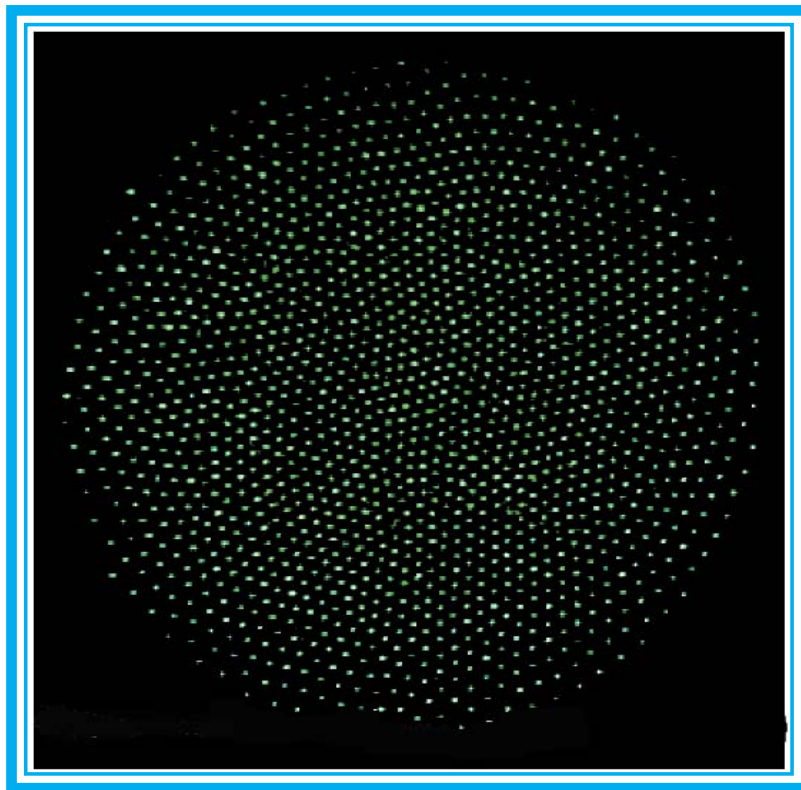




## Research Briefs

*A Department of Energy Multiprogram Laboratory*



---

*Research Briefs* for the Physical and Chemical Sciences Center is published by Sandia National Laboratories. Additional complimentary copies are available by contacting:

**Julia M. Phillips**  
**Physical and Chemical Sciences Center, 1100**  
**Sandia National Laboratories**  
**Albuquerque, NM 87185-1427**

**Phone: (505) 844-1071**  
**Fax: (505) 844-6098**  
**E-mail: [jmphil@sandia.gov](mailto:jmphil@sandia.gov)**  
**url: <http://www.sandia.gov/1100/Xcenter1.htm>**

*Research Briefs*

**Editors**  
J. M. Phillips  
J. A. Nichelason

**Production**  
M. Sheila Wilson

---

**Cover Page:** Top view of light scattering from plasma crystals comprised of different numbers of 8.3  $\mu\text{m}$  diameter, melamine formaldehyde particles suspended in a 1.8 W, 110 mTorr argon plasma. See page 81.

---

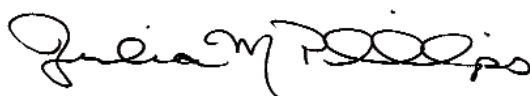
### **Message from the Director**

The Physical and Chemical Sciences Center provides new scientific knowledge in support of Sandia's missions for the Department of Energy. We emphasize research to create and enable emerging technologies. We also provide new understanding needed to support predictive reliability for existing systems. The focus of our work derives from Sandia's role as a multiprogram laboratory with broad-based research and development responsibilities for nuclear weapons, nonproliferation, energy, environment, and other areas of importance to the nation.

Within our portfolio of research investments, this issue of Research Briefs highlights our recent accomplishments supporting longer term/exploratory activities. We address a focused set of strategic themes: science underlying materials performance and reliability, nanoscale structures and devices, advanced sensing science, and the science of semiconductor technologies. We employ a wide range of multidisciplinary capabilities based on the physical and chemical sciences, from first principles modeling and atomic scale measurement to remote laser sensing and the science of complex adaptive behavior. Looking to the future, we are investing in the science that underlies future generations of integrated microsystems, and the microscopic-based physical models needed for predictive reliability of systems in a new era of teraflop computing.

The activities of the Physical and Chemical Sciences Center are supported by a diverse set of funding sources and are managed to assure integration and synergy between projects. The research described here provides examples that illustrate the importance of a strong science base in physics and chemistry to the success of DOE's Stockpile Stewardship mission. This work also provides insights into the connections between science and the wide range of DOE technologies. In essentially all the research described, our partnerships with colleagues in universities, industry, and program areas across the Labs have been critical, and we acknowledge with gratitude their collaboration.

We welcome your inquiries.



**Julia M. Phillips**  
*Director*





# Table of Contents

---

## The Science of Microsystems

Hall-Petch Effect at the Nanoscale: Pulsed-Laser Deposited Nickel .....	6
Separating Mechanical and Chemical Contributions to Molecular-level Friction .....	8
NMR Bonding Studies of <sup>13</sup> C Enriched Amorphous Diamond Films .....	10
Evolution of Al Corrosion at Nano-engineered Cu Islands .....	12
Mechanisms for Atmospheric Sulfidation of Copper .....	14
ONE: Sandia's Optical-Nuclear-Electron Microscope System .....	16

## Surfaces and Interfaces

Surface Passivation by Ordered Water Layers .....	18
Vacancy-mediated Surface Diffusion .....	20
The Evolution of Self-assembled Domain Structures on Solid Surfaces .....	22
The Complex Origins of Intrinsic Stress in Thin Films .....	24

## Nanostructured Materials

Formation of "Magic"-sized Metal and Semiconductor Nanoclusters .....	26
Giant Magnetic Anisotropy in Field-structured Dipolar Nanocomposites .....	28
Colossal Thermoresistance and Piezoresistance Observed in Field-structured Composites .....	30
Precise Control of Carbon Nanotube Diameters Grown Directly onto Substrates .....	32

## Biomolecular Materials and Interfaces

Controlled Switching of Surface Chemistry .....	34
Self-assembling Materials for Biomaterial Adhesion and Hierarchical Structures .....	36
A Study of Cell and Protein Adhesion to SAM-coated Semiconductors .....	38

# Table of Contents

---

## Ferroelectric Materials

Manifestations of Quantum Fluctuations in Ferroelectrics .....	40
Dynamics of Polar Nanodomains in Relaxor Ferroelectrics .....	42
PZT 95/5 Phase Diagram from First Principles and Effective Hamiltonian .....	44
Strong Porosity Effects in the Shock Response of PZT 95/5 .....	46

## Lasers and Optical Materials

Improving the Beam Quality of Nanosecond Optical Parametric Oscillators .....	48
Photoluminescent Investigation of the Defect Structures of Doped and Undoped Lithium Niobate .....	50

## Semiconductor Materials and Physics

Theory of Exciton Transfer between Semiconductor Quantum Wells .....	52
Anomalous Temperature Dependent Exciton Energies in AlGaAs Alloys .....	54
Energy Spectroscopy of Eigenstates of a Ballistic One-dimensional Double Quantum Wire ....	56
Theory of Quantum Dot Lasers .....	58
Coupled-Resonator Vertical-Cavity Laser Diodes .....	60
10 Million cm <sup>2</sup> /Vs Mobility GaAs/AlGaAs Heterostructures and the Metallic Behavior of Dilute 2D Electron Systems .....	62
Emissivity-correcting Pyrometry of Compound Semiconductor Growth .....	64

## Wide Bandgap Compound Semiconductors

Dynamic Model of Hydrogen in GaN .....	66
High Power Electronics Based on the 2D Electron-Gas in GaN Heterostructures .....	68
Optically-pumped UV Lasing from a GaN-based VCSEL .....	70
Transport and Kinetic Processes in GaN Epitaxial Lateral Overgrowth .....	72
Development of Cantilever Epitaxy to Produce High Quality GaN with Reduced Threading Dislocation Densities .....	74
Identification of the Parasitic Chemical Reactions during AlGaN OMVPE .....	76

## Table of Contents

---

### Complex and Collective Phenomena

Physics of Hierarchical Self-Organization .....78

Measurement of Dust Charge and Interaction in 2D Plasma Dust Crystals .....80

Recent Awards and Prizes .....82

Government Advisory Boards and Professional Societies .....87

Resources and Capabilities .....88

Physical & Chemical Sciences Center FY01 Budget - By Customer .....92



# The Science of Microsystems



## Hall-Petch Effect at the Nanoscale: Pulsed-Laser Deposited Nickel\*

by *D. M. Follstaedt and J. A. Knapp*

**Motivation**—Understanding how metals with grains as small as  $\sim 10$  nanometers deform under mechanical stress is a current fundamental scientific issue. For micrometer grain sizes, hardness and yield strength are known to scale with grain diameter ( $d$ ) according to the Hall-Petch relation  $H = H_0 + kd^{-1/2}$ . This relation is generally expected to break down for grains too small to allow at least two dislocations. Atomic-scale simulations indicate that other processes not involving dislocations control plastic deformation at sizes below 10 nanometers. However, experimental results show varying behaviors: hardness no longer increases with decreasing size and may even decrease. Moreover, the size at which deviations from Hall-Petch behavior occur varies, and can be as large as  $\sim 100$  nanometers. In particular, the behavior of fine-grained electrodeposited nickel is unclear. Understanding this material will be important for reliably achieving very high strengths and hardnesses in nickel-based components made by the LIGA electrodeposition process for micro-electromechanical systems (MEMS).

**Accomplishment**—We have used pulsed-laser deposition to form 500 nanometer-thick layers of nickel with grains as small as 12 nanometers, as seen in Fig. 1. To evaluate the mechanical properties of these thin layers independently of their substrates, we used an approach developed by us that combines ultra-low load indentation with finite-element analysis. We found that the Hall-Petch relationship applies to our entire range of grain sizes, as shown in Fig. 2. In accord with this relationship, exceptionally high hardness and yield strength, 10 gigapascals and 2.5 gigapascals, respectively, are obtained with the smallest grain size. This finding implies that plastic deformation occurs by dislocation

movement in small grains. In joint work with Los Alamos National Laboratory, we have recently observed such dislocations directly. A nickel film of 15-nanometer grains was examined in situ during tensile straining in a transmission electron microscope. Dislocations were seen to move across grains ahead of an advancing crack. Multiple dislocations were seen in some grains, as required for Hall-Petch hardening. Moreover, the film thinned immediately ahead of the crack tip before tearing, demonstrating that this material is highly ductile. Such ductility was not observed in fine-grained nickel prepared by other methods, which showed brittle failure by intergranular fracture.

**Significance**—Fine-grained nickel prepared by pulsed-laser deposition shows excellent mechanical properties that are governed by the propagation of dislocations. This material demonstrates that the Hall-Petch relationship extends to grain sizes as small as 12 nanometers in nickel. Future theoretical descriptions of mechanical properties with small grain sizes must correctly address plastic deformation by dislocation motion for such grain sizes. Departures from the Hall-Petch relationship are still expected at even smaller grain sizes. We think the advantages of our material result from its high purity and expected full atomic density; these properties are often lacking in fine-grained nickel prepared by other methods. This work shows that the properties of nickel made by other methods, including electrodeposition, have not been intrinsically limited by deformation mechanisms, but are likely to be improved by reducing impurity content and porosity.

\*Collaborators: R. C. Hugo and H. Kung, Los Alamos National Laboratory

**Sponsors for various phases of this work include:** BES, Nuclear Weapons/Science and Technology

**Contact:** David M. Follstaedt, Radiation-Solid Interactions, Department 1111

Phone: (505) 844-2102, Fax: (505) 844-7775, E-mail: dmfollls@sandia.gov

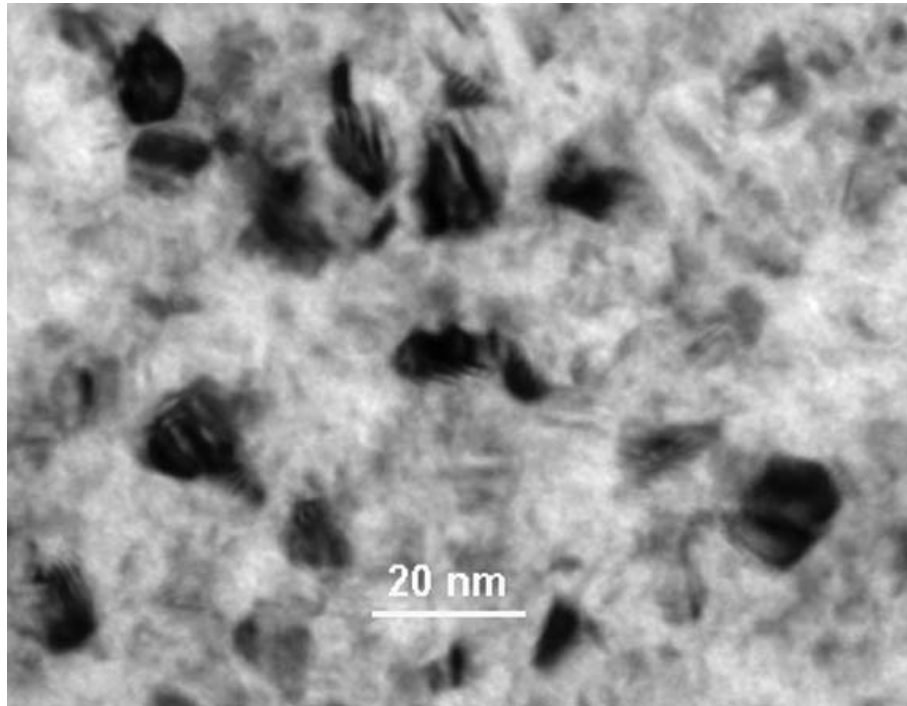


**Figure 1.** Bright-field TEM image showing fine grains of nickel in pulsed-laser deposited (PLD) layers. The average grain size is 12 nanometers.

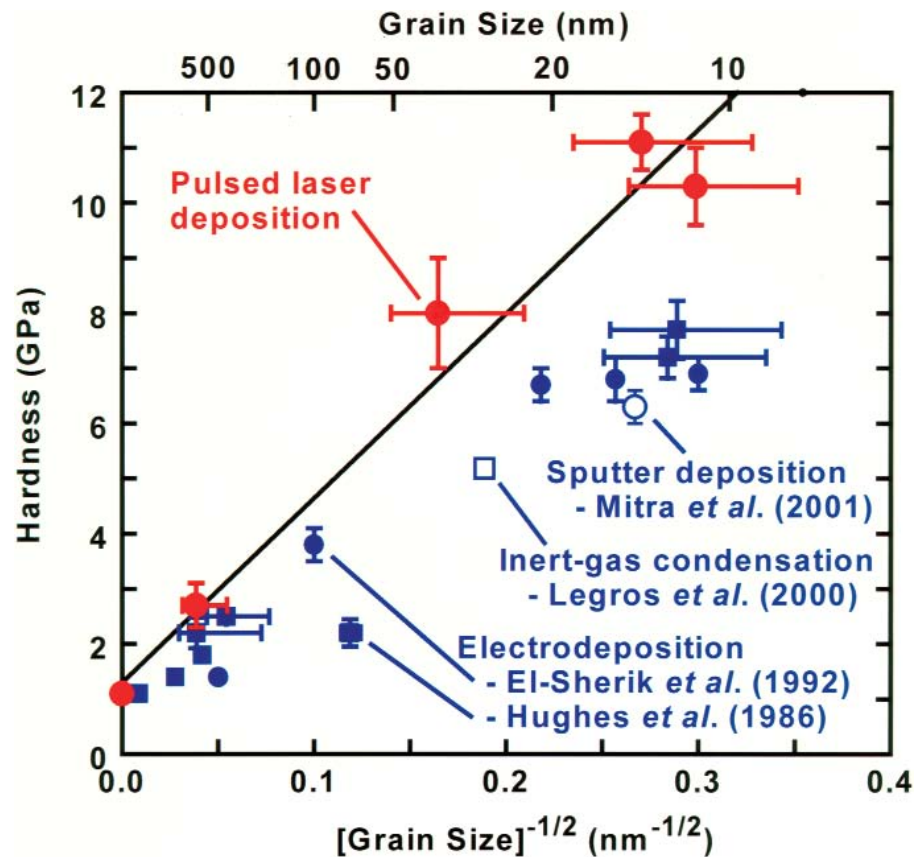


**Figure 2.** Hardness of the PLD nickel layers plotted versus the inverse square-root of grain size. Hardness was determined by finite-element analysis of nanoindentation force versus depth data. Results obtained by other workers are also included.

## Separating Mechanical and Chemical Contributions to Molecular-level Friction

by *Hyun I. Kim and J. E. Houston*

**Motivation**—There has recently been growing interest in the use of self-assembled monolayer (SAM) films as lubricants for applications such as micro-electromechanical machines. The excitement in this area involves the potential to tailor friction and adhesion via these monolayer films. The missing link in being able to achieve such control is the relationship between the various parameters of the modification and the resulting tribological properties.

**Accomplishment**—We have applied the interfacial force microscope in a systematic study of the adhesive and frictional forces for self-assembled monolayers (SAMs) terminated by various combinations of end groups with contrasting chemical functionality. The goal was to use the model systems to separate the role of adhesion from that of purely mechanical modes of energy loss in lateral motion. The focus is on the simultaneous measurement of the adhesive and friction forces for SAM-coated Au probe and sample surfaces. We systematically alter the chemical nature of the SAM surfaces and tabulate the forces for various combinations of methyl ( $-\text{CH}_3$ ) and carboxylic acid ( $-\text{COOH}$ ) end groups. The  $-\text{CH}_3$  represents a chemically inert interface while  $-\text{COOH}$  has the capability of forming hydrogen bonds. Other than these end groups, the backbones for the SAMs are identical. This makes it possible to separate the friction force in the presence and absence of a chemical interaction. Figure 1 illustrates the

results for the purely passive  $-\text{CH}_3$  pair, the  $-\text{CH}_3/-\text{COOH}$  combination, and the  $-\text{COOH}$  pair. Only weak van der Waals forces and low friction are seen for the first two combinations, while the last shows increases in both. The "adhesive" friction is the difference between the two sets and results from the making and breaking of hydrogen bonds. Changing the backbone length by one  $-\text{CH}_2$  unit alters the conformation of the  $-\text{COOH}$  groups and changes the H-bonding (Fig. 2). These results indicate that the odd  $-\text{COOH}$  film has intra-film bonding, while the even can support bonding between films (inter-film). Lateral tip motion disturbs the bonds in both cases. For  $-\text{CH}_3$  vs.  $-\text{COOH}$  (Odd) only H bonds from a single film are disturbed, while for the  $-\text{COOH}$  (Odd) pair two H-bonded films are disturbed. The more bonds disturbed by the tip the higher the friction.

**Significance**—These results are the first such measurements of the individual mechanisms involved in molecular-level friction. Coupled with earlier work showing the effect of packing density upon friction, the results give a much clearer picture of the role of each in producing a particular tribological behavior. Such work will have broad impact on areas of science and technology involved with tailoring surface modification for specific tribological function and will promote theoretical modeling of the details of the interactions involved in these processes.

---

**Sponsors for various phases of this work include:** BES, LDRD

**Contact:** J. E. Houston, Surface and Interface Science, Department 1114

Phone: (505) 844-8939, Fax: (505) 844-1197, E-mail: [jehoust@sandia.gov](mailto:jehoust@sandia.gov)

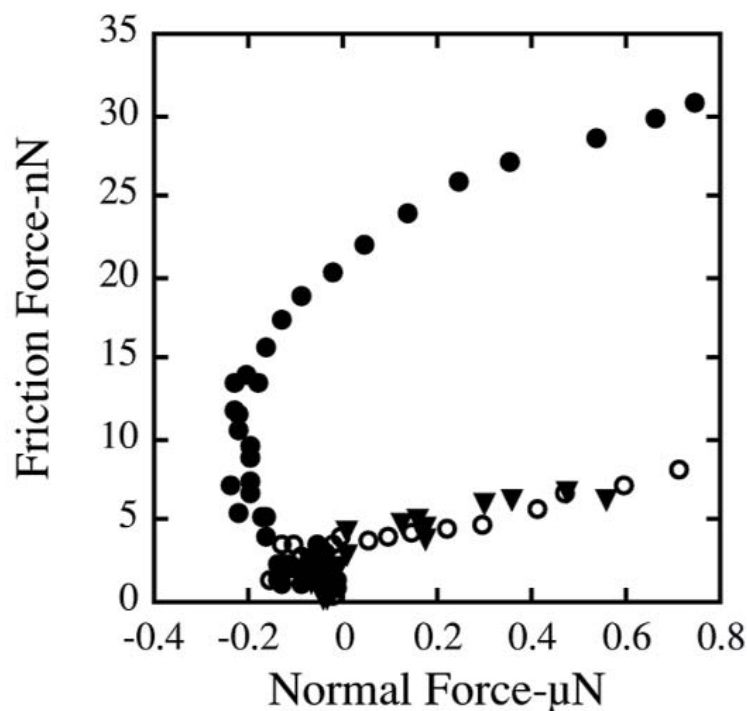


**Figure 1.** Filled circles are for  $-\text{COOH}/-\text{COOH}$  (Even), open circles for  $-\text{CH}_3/-\text{COOH}$  (Even) and inverted triangles are for  $-\text{CH}_3/-\text{CH}_3$  combinations. Negative normal forces are attractive, positive ones repulsive. Large adhesion and friction results from the strong inter-film  $-\text{COOH}/-\text{COOH}$  hydrogen bonding interaction involving both films. The other combinations involve no chemical bonds, and the friction is purely mechanical in origin.

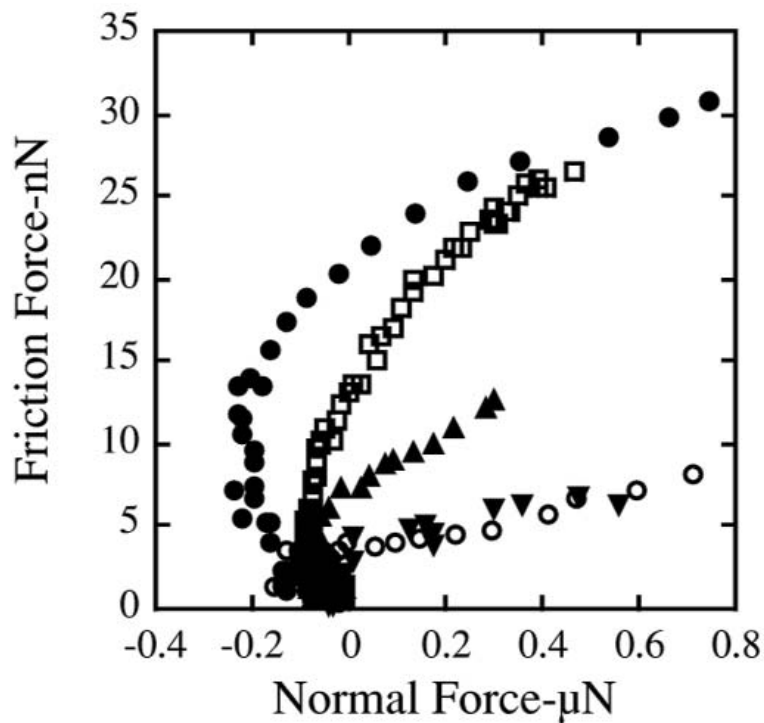


**Figure 2.** Same as Fig. 1 with the addition of the  $-\text{COOH}/-\text{COOH}$  (Odd) — open squares — and  $-\text{CH}_3/-\text{COOH}$  (Odd) — filled triangles — combinations.  $-\text{COOH}$  (Odd) films form intra-film hydrogen bonds but no inter-film bonds. Thus, friction is highest for the double-odd combination and about half for the single-odd combination.

## NMR Bonding Studies of $^{13}\text{C}$ Enriched Amorphous Diamond Films

by *T. A. Friedmann and T. M. Alam*

**Motivation**—Amorphous diamond thin films grown by pulsed laser deposition are currently being used in MEMS and sensor technologies under development at Sandia National Laboratories. Our discovery that amorphous diamond thin films can be fully stress relieved (Patent #5,821,680) has enabled these applications and is a direct result of basic research on this material.

In spite of this research, there is comparatively little understanding of the local bonding structure in these films. This is a direct consequence of the fact that both the length and bond angle of 3- and 4-fold bonds can vary considerably. This variability coupled with the amorphous structure make characterization of this material difficult. Useful characterization techniques include Raman spectroscopy, x-ray reflectivity, and electron energy loss spectroscopy (EELS). With these techniques it is possible to infer the mass density and the relative bonding percentage of 3- and 4-fold carbon to within  $\sim 5\%$ , but quantitative detailed knowledge of the bonding structure is much more difficult (if not impossible) to obtain.

Solid state NMR spectroscopy of carbon-based materials is a well developed field that is capable of probing the local carbon bonding environment quantitatively even in amorphous materials. Unfortunately, it has not been applied to thin film amorphous diamond samples since no bulk analogue exists, and the NMR signal from natural abundance samples is too small to be useable.

**Accomplishment**—We have been able to grow almost completely enriched (99%)  $^{13}\text{C}$  amorphous carbon thin film samples. The target for

the deposition was made by pressing enriched  $^{13}\text{C}$  graphite powder to 99% of the theoretical density of graphite. Raman spectra of the enriched samples reveal a large frequency shift due to the heavier  $^{13}\text{C}$  atom (Fig. 1) but appear otherwise identical to samples made from unenriched targets.

Importantly, we were able to obtain quantitative magic angle spinning (MAS) solid state NMR spectra from these samples. These measurements have been made on as-deposited and annealed samples to study the structural changes with annealing that are associated with stress relief (Fig. 2). The as-deposited samples are highly metastable with peak widths that are very broad and positions that are much higher than for the crystalline analogues of graphite and diamond. Annealing allows for stress relaxation of these bonds and is revealed in the NMR spectra by a peak shift (toward the crystalline) and narrowing of the resonances for both the  $\text{sp}^3$  and  $\text{sp}^2$  components. Further measurements with longer acquisition times should allow quantitative determination in the bonding down to the 1% level.

The high enrichment percentage also enables the quantitative measurement of correlations between  $^{13}\text{C}$  atoms in the sample through the use of 2D radio-frequency dipolar recoupling experiments. These experiments allow the determination of the percentage of carbon atoms with specific 3- or 4-fold bonded neighbors.

**Significance**—These measurements enable direct comparison to theoretical structural models derived from first-principles structural models — the first time this has ever been done for this complex material.

---

**Sponsors for various phases of this work include:** LDRD

**Contact:** Thomas Friedmann, Nanostructure and Semiconductor Physics, Department 1112

Phone: (505) 844-6684, Fax: (505) 844-1197, E-mail: tafried@sandia.gov

---



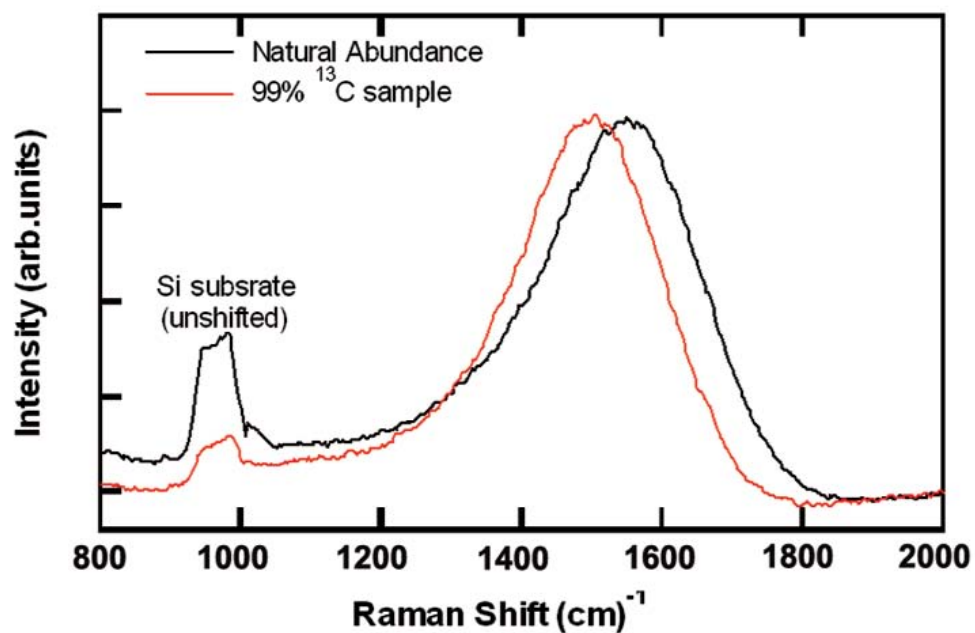


**Figure 1.** Raman spectra of natural abundance and <sup>13</sup>C enriched sample. The peak shift is due to the higher mass difference of the two isotopes.

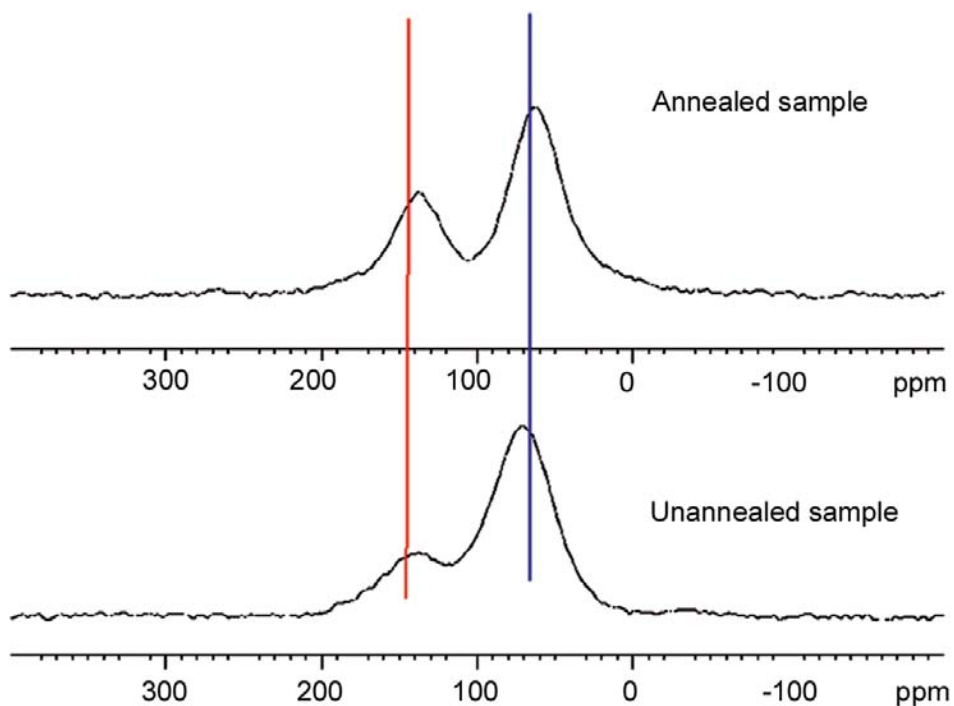


**Figure 2.** NMR spectra from as-grown and annealed amorphous carbon films. The sp<sup>3</sup>-carbon peak narrows and shifts toward the crystalline diamond peak with annealing.

## Evolution of Al Corrosion at Micro-engineered Cu Islands

by *N. Missert, J. C. Barbour, R. G. Copeland and J. E. Mikkalson*

**Motivation**—Although corrosion in Al alloys often occurs at second phase particles, the mechanisms responsible for the initiation and evolution of the corrosion process are not well understood. Alloys typically contain particles with a variety of compositions, sizes and spatial distributions. The galvanic nature of corrosion near these particles is expected to produce a heterogeneous solution chemistry that may affect the corrosion rate of the surrounding matrix. Understanding the evolution of the solution environment during corrosion, as a function of particle size and spacing, is important for enabling accurate predictive models and ultimately, for developing successful approaches to corrosion mitigation.

**Accomplishment**—We have measured the evolution of solution chemistry during corrosion of a model Al-Cu alloy system. The model alloy was designed to carefully control the chemistry, size, and spacing between Cu particles on an Al matrix. An ultra-high purity Al thin film was electron-beam evaporated onto an SiO<sub>2</sub> coated Si wafer to form the matrix. The Cu particles were fabricated by using standard photolithography to define island size and spacing, followed by Cu thin-film deposition and lift-off. Corrosion of Al on samples containing arrays of Cu particles with diameters ranging from 2 - 100  $\mu\text{m}$  and spacings of 10 - 500  $\mu\text{m}$  were investigated by immersion in dilute NaCl containing a small amount of fluorescein. In-situ confocal scanning laser microscopy was used to image fluorescein emission during the corrosion process. The fluorescein emission intensity increases with pH, so a heterogeneous solution chemistry that may develop due to a spatial

separation between the cathodic (alkaline) and anodic (acidic) sites, could be imaged in-situ. Figure 1a shows an image taken when the corrosion rate was high, where the solution above the Cu particles is alkaline due to the oxygen reduction reaction. The fluorescein emission intensity was observed to fluctuate with time, indicating a non-uniform corrosion rate. The fluctuations in emission intensity were linked to the open circuit potential,  $V_{oc}$ , as shown in Figs. 1 and 2. When the emission intensity was high, or the sample was actively corroding,  $V_{oc}$  remained low, while when the emission intensity dropped, or the sample was not actively corroding,  $V_{oc}$  increased. This type of behavior was observed for the whole range of particle sizes and spacings investigated, and corresponds to the changes in the rate of Al corrosion beneath the Cu particles. When the spacing between Cu particles was decreased to 10  $\mu\text{m}$ , the regions of alkaline solution overlapped, greatly increasing the corrosion rate of the surrounding Al matrix.

**Significance**—These results show that an anode and cathode can exist at the same site due to the restricted geometry at the particle/matrix interface. Corrosion at the Cu particles does not proceed in a uniform fashion, rather it occurs through a series of initiation and re-passivation events. The link between the rate of Al corrosion beneath the particles and  $V_{oc}$  shows that the open circuit fluctuations typically observed in Al alloys are not simply due to metastable pitting in the matrix, but can be linked to corrosion at particles also. Finally, in order to avoid regions of overlapping alkaline solution during corrosion, spacing between particles should be maximized, possibly through special alloy heat treatments.

---

**Sponsors for various phases of this work include:** BES, Nuclear Weapons/Science and Technology

**Contact:** Nancy Missert, Nanostructure and Semiconductor Physics, Department 1112

Phone: (505) 844-2234, Fax: (505) 844-1197, E-mail: namisse@sandia.gov

---

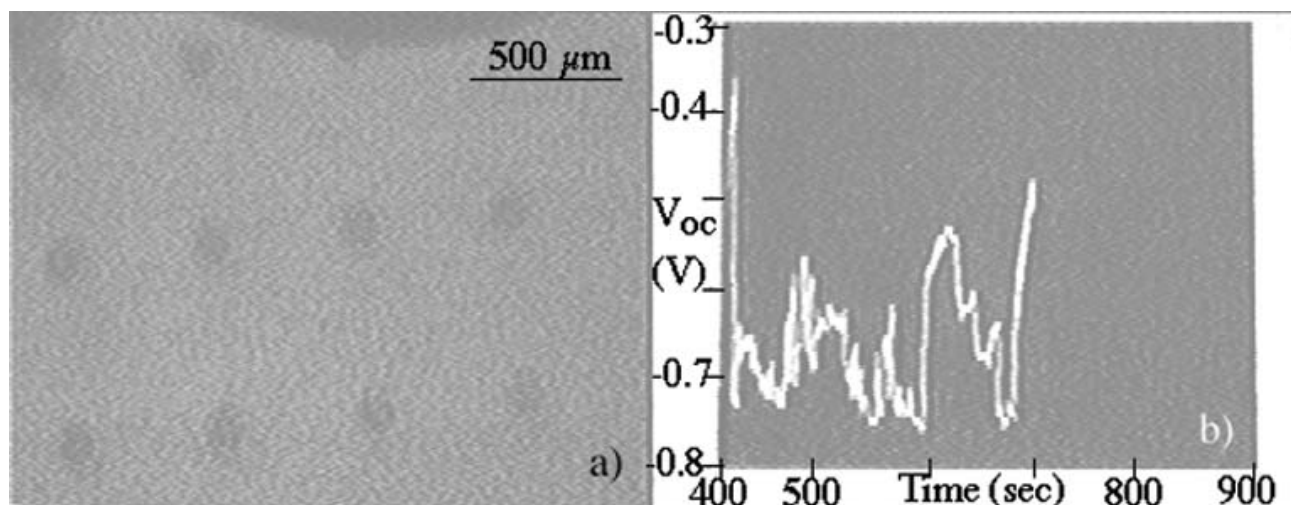


**Figure 1.** a) In-situ, confocal microscope image showing dim fluorescein emission in solution or a low  $\text{OH}^-$  production rate on Cu particles, which corresponds to a high open circuit potential. b) Open circuit potential as a function of time — a high value indicates a low Al corrosion rate.

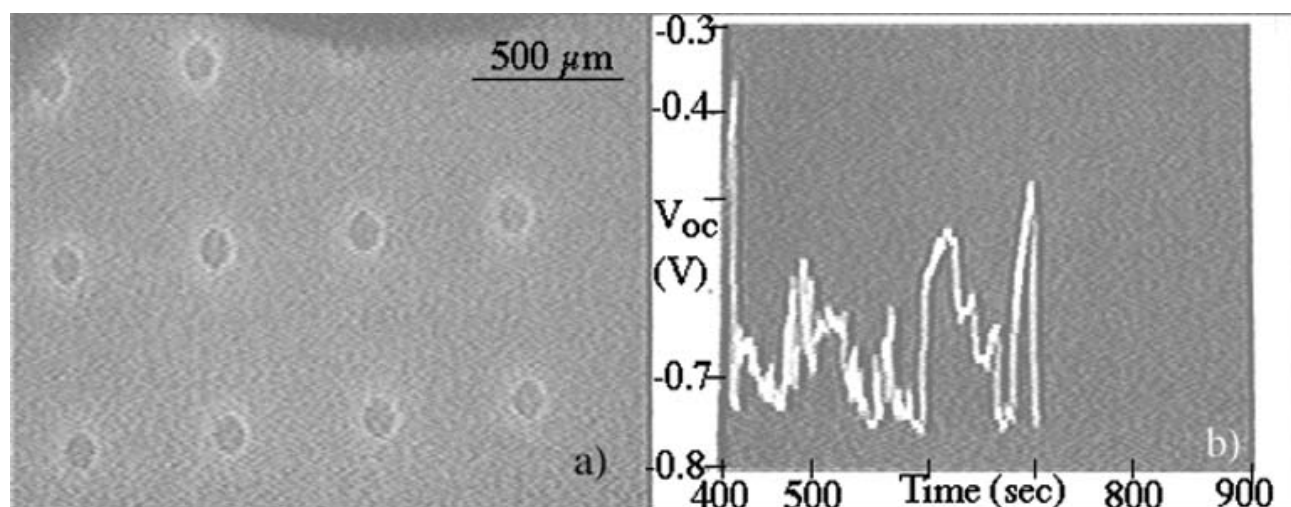


**Figure 2.** a) In-situ, confocal microscope image showing bright fluorescein emission in solution or a high  $\text{OH}^-$  production rate on Cu particles. b) Open circuit potential as a function of time — low value at longest time indicates active Al corrosion.



## Mechanisms for Atmospheric Sulfidation of Copper

by J. C. Barbour and J. W. Braithwaite

**Motivation**—Atmospheric sulfidation of copper-containing components in electrical systems has been identified as an important corrosion process that can impact the performance of numerous subsystems: from printed circuit boards to power supplies. In order to predict the effects of this corrosion process reliably, the mechanisms by which Cu sulfidation occurs need to be understood and the activation energies for sulfidation need to be measured. This work reports on the first step in this process to measure the dominant moving species in  $\text{Cu}_2\text{S}$  formation, and the effect of relative humidity (RH) on  $\text{Cu}_2\text{S}$  growth kinetics.

**Accomplishment**—Ion-beam analysis was used to measure the thickness of  $\text{Cu}_2\text{S}$  films growing on copper substrates as a function of RH and temperature. The copper was sulfidized in atmospheric environments containing  $\text{H}_2\text{S}$  (50-600 ppb  $\text{H}_2\text{S}$  in air with 0.5-85% relative humidity). A series of marker experiments, using gold patches as the markers, at both high and low RH showed that sulfidation proceeds by solid-state transport of Cu from the substrate through the  $\text{Cu}_2\text{S}$  product layer. Further, little if any transport of sulfur was observed. Copper was conclusively determined to be the fastest moving species at both high and low RH. Figure 1 shows the results from the analysis. For both the high and low RH experiments, the samples initially grow a  $\text{Cu}_2\text{S}$  layer which increases linearly with time (termed stage I linear growth regime). The difference in humidity, however, appeared to produce a dramatic effect on sulfidation growth rates for long times, perhaps as a result of different kinetic mechanisms.

For low RH, the samples stayed in stage I growth kinetics for the entire experiment; whereas the samples exposed to the high RH environment had a decreased growth rate at longer times (greater than 10 hours) consistent with solid-state diffusion-controlled growth, termed stage II kinetic growth regime. It should be noted that the stage I growth rate was faster for the high RH environment than for the low RH environment, and both are less than the theoretical maximum from gas-phase transport-limited growth (shown as a solid red line). In order to get a clue to possible different primary stage I growth mechanisms at low and high RH sulfidation,  $\text{Cu}_2\text{S}$  growth rates were analyzed as a function of sulfidation temperature. These results are given in Fig. 2a and b for the low and high RH environments, respectively. The activation energy at low RH ( $E_{\text{AL}}$ ) was more strongly dependent on temperature than that at high RH ( $E_{\text{AH}}$ ); and  $E_{\text{AL}} > E_{\text{AH}}$ , consistent with a difference in growth rate mechanisms. The slope of the Arrhenius plot in Fig. 2a gives  $E_{\text{AL}} = 0.34 \text{ eV}$  (7.8 kcal/mole), which is consistent with a mix of gas-phase diffusion and surface reaction-limited kinetic mechanisms. The slope in Fig. 2b gives  $0.03 \text{ eV} < E_{\text{AH}} < 0.18 \text{ eV}$  (0.6 to 4.1 kcal/mole) which is consistent with a gas-phase diffusion limited process.

**Significance**—This work demonstrates the importance of understanding the role of humidity on copper sulfidation mechanisms. For the first time, different activation energies have been determined for both high and low relative humidities.

**Sponsors for various phases of this work include:** LDRD, Nuclear Weapons/Science and Technology

**Contact:** J. Charles Barbour, Nanostructure and Semiconductor Physics, Department 1112

Phone: (505) 844-5517, Fax: (505) 844-7775, E-mail: jcbarbo@sandia.gov

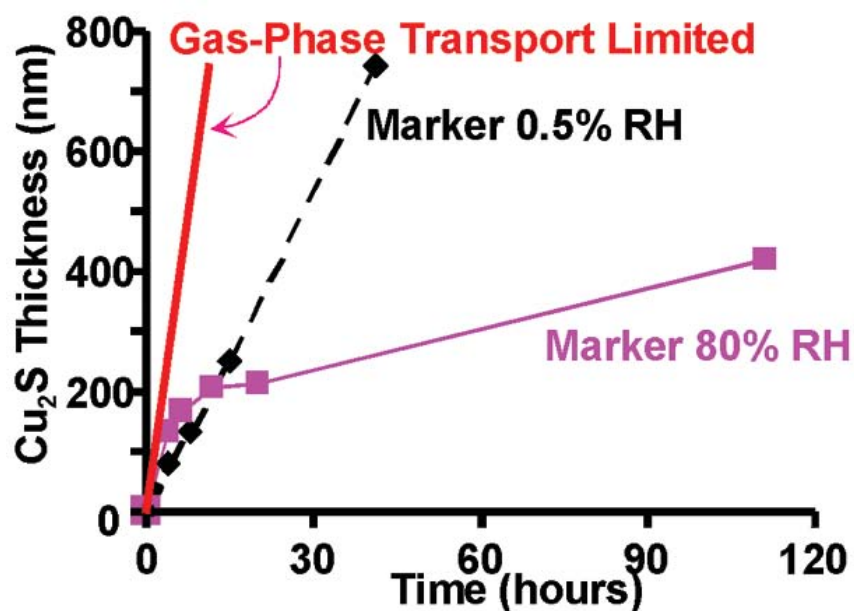


**Figure 1.** Different  $\text{Cu}_2\text{S}$  growth rates suggest different kinetic mechanisms observed for high and low RH sulfidation.

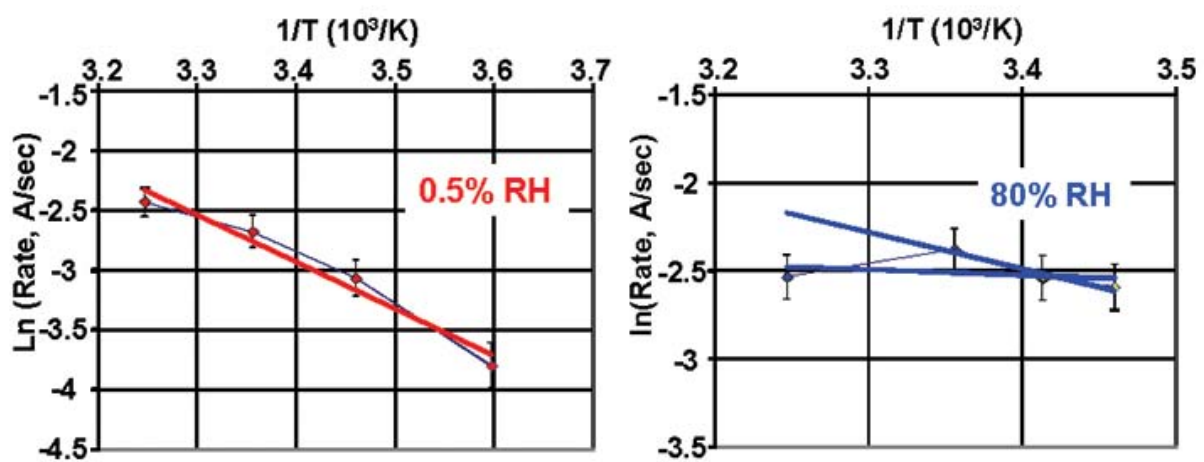


**Figure 2.** Activation energies for the low (a) and high (b) humidity sulfidation give clues to different primary growth mechanisms. At low RH,  $E_A = 0.34 \text{ eV}$  (7.8 kcal/mole), and at high RH  $0.03 \text{ eV} < E_A < 0.18 \text{ eV}$  (0.6 to 4.1 kcal/mole).

## ONE: Sandia's Optical-Nuclear-Electron Microscope System

by *D. S. Walsh, B.L. Doyle and G. Vizkelethy*

**Motivation**—Over the last decade Sandia has used the nuclear-ion microprobe to perform pioneering studies of radiation effects in semiconductor-based electronics at the microscopic level. During that decade phenomenal improvements in semiconductor manufacturing techniques have reduced the critical dimensions of devices about an order of magnitude. Consequently, analysis and research tools must also improve their resolution in order to study effects on scales that are relevant to modern technologies. The Sandia Optical-Nuclear-Electron hybrid microscopy system was designed to enable radiation effects microscopy research of the shrinking modern semiconductor technologies.

**Accomplishment**—ONE is an integrated, high vacuum chamber/positioning system jointly designed with Raith, Inc., for the Sandia nuclear microprobe. The system combines a positioning stage accurate to 0.1  $\mu\text{m}$  with optical, secondary electron and nuclear microscopes.

The sample stage uses laser interferometric feedback to control DC and piezoelectric positioning motors. Sophisticated software control of the stage, electron and nuclear microscopes allows the user to position test devices using the manufacturer's design layouts (GDSII format). Using this system we can target the desired microscopy to any point on the device under test (DUT) quickly, accurately and with a high degree of repeatability. Samples of various geometries up to 8" in diameter and 1" thick can easily be mounted upon the stage. Standard mounts for silicon wafers, 40 pin ZIF and Planar Gate Array sockets are available. The stage can target an area on the DUT 100 by 300 mm for

optical, nuclear and electron microscopic study.

Communication with the DUT in the vacuum chamber is possible via permanently mounted 25pin DB cables (6 total) and 6-BNC cables (6 total). Bulkhead SMA (6 total) connectors can be used to provide high-speed connections to the DUT.

A JEOL OM-40a annular microscope provides the optical microscopy for the ONE chamber. Maximum magnification is about 300x with resolution on the order of a micron. The secondary electron microscope is a FEI/Philips XL-30 model with up to 100kx magnification. The nuclear microprobe is a Sandia design using a Dyer Systems QL-100 quadrupole lens with electrostatically isolated lens tips for fast beam scanning. The resolution of ion beams from 4.5 MeV protons to 50 MeV copper is 0.5 to 1 micron. Sophisticated data collection and analysis software allows the user to collect position-correlated responses of the DUT to photon, ion, or electron exposure.

**Significance**—Radiation effects in semiconductor electronics are becoming increasingly important as device dimensions decrease and space and weapons applications increase. The targeting abilities and versatility of the ONE system make it an excellent tool for studying the mechanisms and effects of radiation on semiconductors at the microscopic level. Figures 1 and 2 show examples of heavy ion radiation microscopy measurements on Sandia's bulk silicon technology (CMOS6) TA788 16k SRAM along with excellent agreement with computer model predictions.

---

**Sponsors for various phases of this work include:** Nuclear Weapons/Science and Technology, LDRD

**Contact:** David S. Walsh, Radiation Solid Interactions, Department 1111

Phone: (505) 844-9590, Fax: (505) 844-7775, E-mail: dswalsh@sandia.gov

---

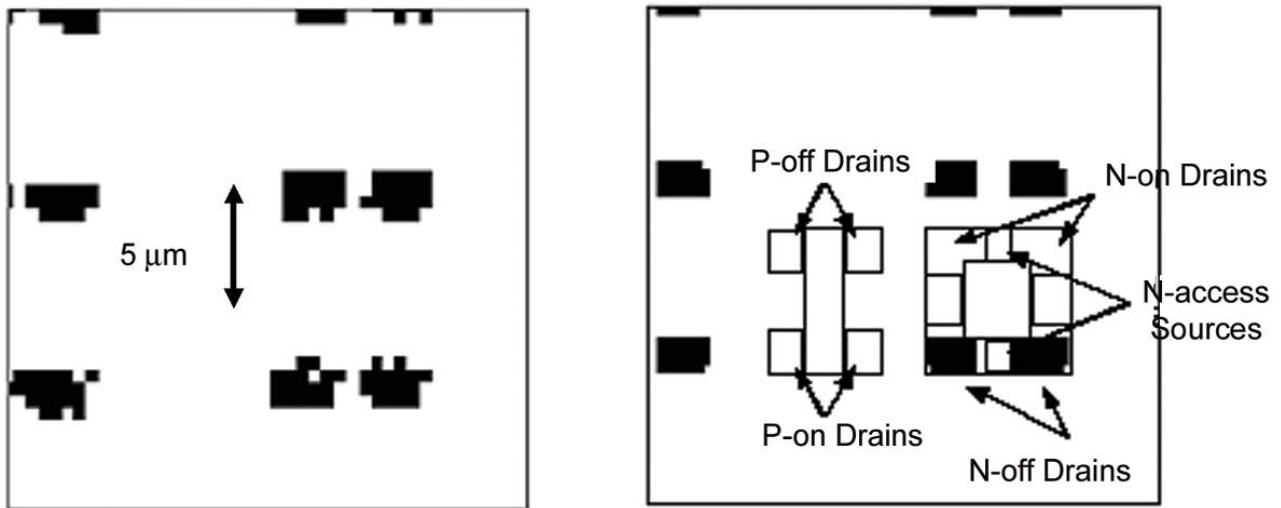


**Figure 1.** Left: Single-event upset (SEU) image of several unit cells in a TA788 16K bulk SRAM obtained with focused 35-MeV chlorine ions on the ONE system. Right: Equivalent simulated SEU map for 35-MeV chlorine ions. The upsetting regions correspond to the reverse-biased n<sup>+</sup> drains.

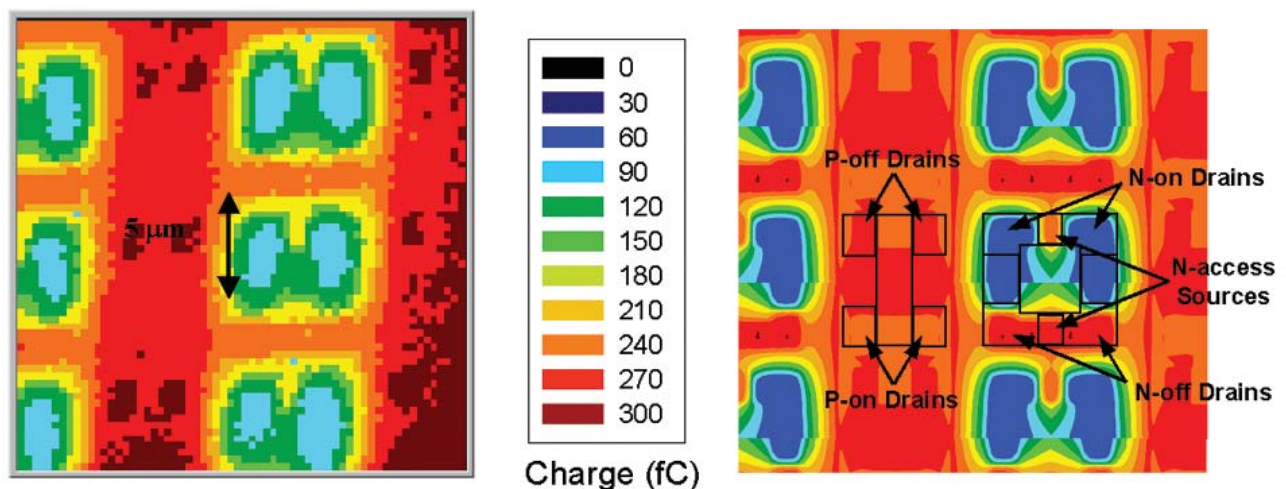


**Figure 2.** Left: Calibrated Ion Beam Induced Charge (IBIC) image of several unit cells in a TA788 16K bulk SRAM obtained with focused 20-MeV carbon ions on the ONE system. Right: Equivalent simulated charge-collection map for 20-MeV carbon ions. The color scales for both maps are the same and indicate total charge collection measured at the power supply. Note the remarkable agreement between model and experiment.



# Surfaces and Interfaces

## Surface Passivation by Ordered Water Layers

by *Hyun I. Kim J. G. Kushmerick, J. E. Houston and B. C. Bunker*

**Motivation**—An area of particular interest in bio-materials is the production of surfaces which are resistant to protein adsorption. Self-assembling monolayers (SAMs) terminated by only a small number of oligo (ethylene glycol), i.e.,  $(-\text{O}-\text{CH}_2-\text{CH}_2-)$ , units have been shown to provide unique and non-specific protein resistance. It has been suggested that this material may form a template for the organization of a water inter-phase which passivates the surface. However, the mechanisms involved in this important process are not presently understood.

**Accomplishment**—We have applied the interfacial force microscope to examine how surfaces coated with self-assembled monolayers interact with each other through water. Both a Au probe tip and a single crystal Au substrate are functionalized with various combinations of oligo(ethylene glycol)  $(-\text{O}-\text{CH}_2-\text{CH}_2-)_3$  (designated EG3),  $-\text{OH}$ , and  $-\text{CH}_3$  end groups. Both the normal and lateral friction forces are measured as the tip approaches and retracts at a constant rate. In air, normal force measurements reveal a van der Waals attraction followed by a hard-wall repulsion (after the two surfaces come into contact). However, in water, a long-range repulsion is detected whenever an EG3 surface is present. The repulsion is thought to be due to the presence of an ordered water layer nucleated by the EG3. To determine the mechanical properties of this interphase

water, contact mechanics models have been used to remove the compliance contributions of the Au tip and substrate as well as the contacting SAM films. Results for combinations involving -EG3 are shown in Fig. 1. For the -EG3 vs. -EG3 contact, the results are consistent with the presence of an ordered, viscoelastic water layer that is at least 4 nm thick, while the asymmetric combinations show lesser values. The viscous, fluid nature of the layer is apparent in the hysteresis in both lateral friction and slow approach measurements (Fig. 2). The layer has an apparent viscosity that is seven orders of magnitude less than that of ice, but still seven orders of magnitude more viscous than normal room-temperature water. The elastic response of the layer is more apparent at high approach rates, where the level of the repulsive force rises and there is less hysteresis. Work is in progress to determine the elastic modulus and compare it to that of ice.

**Significance**—Our results represent the first detailed study of the nano-mechanical and tribological properties of ordered water near interfaces. The results show that some surfaces can influence the structure and properties of water out to much greater distances than the one or two monolayers invoked in classical models for surface solvation. The presence of thick ordered water layers may be highly significant for explaining phenomena ranging from protein folding to fluid flow in nano-systems.

**Sponsors for various phases of this work include:** BES, LDRD

**Contact:** J. E. Houston, Surface and Interface Science, Department 1114

Phone: (505) 844-8939, Fax: (505) 844-1197, E-mail: [jehoust@sandia.gov](mailto:jehoust@sandia.gov)



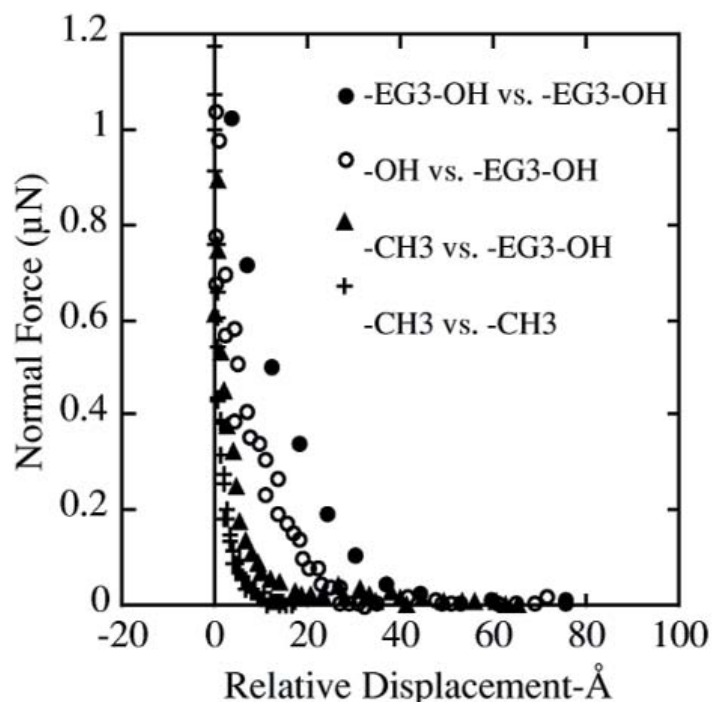


**Figure 1.** Force profiles for various combinations of end groups involving -OH, and -CH<sub>3</sub> interacting with three oligo (ethylene glycol) units, as well as a -CH<sub>3</sub> terminated pair. The data has been corrected for the compliance behavior of the Au tip and substrate and that of the two supporting SAM films in contact. The zero of the displacement axis corresponds to the point at which the films have essentially zero compliance.

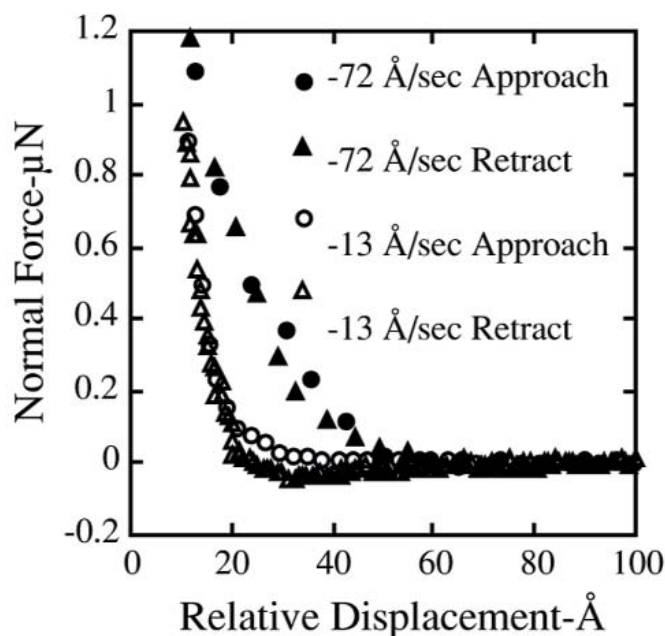


**Figure 2.** Force profiles for the three-unit oligo (ethylene glycol)-terminated SAM at two tip speeds. The symmetric hysteresis (around the zero of force) and dramatic difference in force level for the two speeds is interpreted as the result of a water interphase organized by the oligo (ethylene glycol) interaction, which has a calculated effective viscosity seven orders of magnitude larger than that of liquid water.

## Vacancy-mediated Surface Diffusion

by *B. S. Swartzentruber, M. L. Grant, N. C. Bartelt, and J. B. Hannon*

**Motivation**—The formation kinetics and thermodynamic stability of metal alloy structures is an important part of solder and braze technology, particularly at the interface between dissimilar materials. Performing measurements on the atomic length scale commensurate with state-of-the-art calculations allows the connection that enables a more thorough and realistic understanding of physical processes. Such measurements can also reveal rather unexpected or overlooked mechanisms that play a predominant role in materials behavior.

**Accomplishment**—We used atom-tracking scanning tunneling microscopy (STM) and ab-initio electronic-structure calculations to study the surface diffusion of individual Pd atoms embedded in the outermost layer of the Cu(001) surface. Through comparison of the measured diffusion statistics with model simulations and calculations we determined that diffusion occurs solely by exchange with surface vacancies. The experiments were performed in ultra-high vacuum using a variable-temperature STM. We deposited a very small amount of Pd onto a clean Cu surface. Upon deposition, adsorbed Pd atoms readily exchange with surface copper atoms, embedding themselves in the outermost layer of the crystal surface. In Fig. 1 we show an STM image of embedded Pd atoms in the Cu lattice. We measured the subsequent diffusion of the Pd atoms as a function of temperature using atom-tracking STM. In atom-tracking mode, the STM probe tip is locked onto an individual Pd atom using lateral feedback. The 2-d coordinates of the atom are measured as a function of time with a time resolution of about 1 ms.

The right side of Fig. 1 shows the X and Y coordinates of a diffusing Pd atom at 62 C over 160 seconds. Analyzing the hop rate as a function of temperature from 25 to 70 C yields an activation energy for diffusion of 0.88 eV. Of particular importance is the fact that not all of the hops are to nearest-neighbor positions. About 25% of the hops are longer than unit length (Fig. 2). Comparison of the hop length distribution with Monte-Carlo simulations of various diffusion processes revealed that the diffusion mechanism is due to thermal surface vacancies diffusing over the lattice occasionally exchanging with the Pd atoms resulting in their motion. When a vacancy is meandering in the neighborhood of a Pd atom, it can exchange with it several times in rapid succession leading effectively to long hops. To further understand this diffusion process we performed ab-initio electronic structure calculations using the VASP total energy code. The calculated vacancy formation energy plus the vacancy-palladium exchange barrier is 0.94 eV, in good agreement with our measurement.

**Significance**—By measuring the detailed statistics of the atomic motion directly we are able to determine that the diffusion of surface palladium atoms occurs via exchange with surface vacancies. This result implies that the surface copper atoms are also mobile, diffusing readily as the vacancies migrate around the surface. Adding the notion of vacancy-mediated surface diffusion to our intuitive understanding of atomic processes enhances our ability to predict and explain phenomena critical to interface behavior.

**Sponsors for various phases of this work include:** BES, LDRD

**Contact:** Brian S. Swartzentruber, Surface and Interface Science, Department 1114

Phone: (505) 844-6393, Fax: (505) 844-1197, E-mail: [bsswart@sandia.gov](mailto:bsswart@sandia.gov)



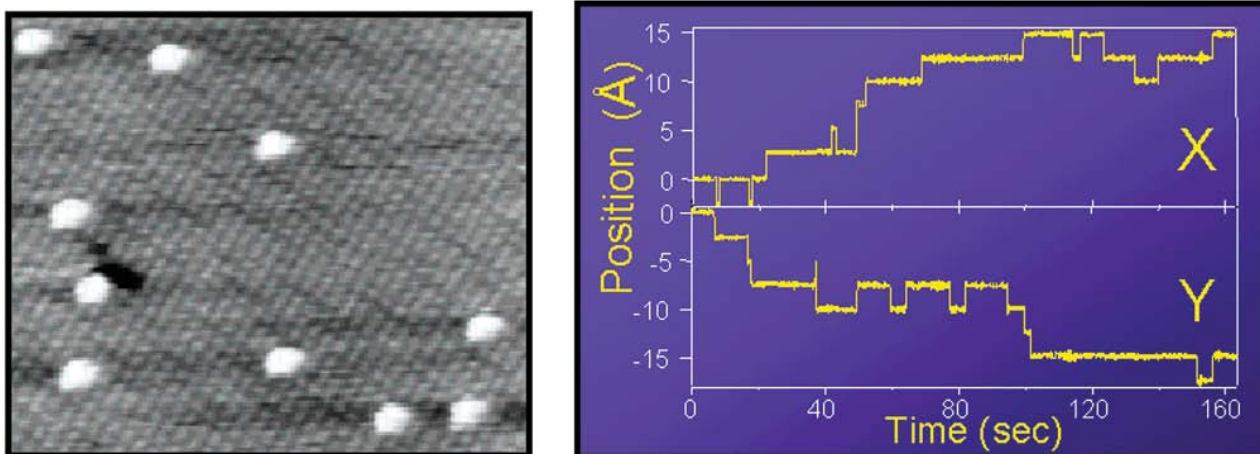


**Figure 1.** Left side, an STM image ( $95 \times 85 \text{ Å}^2$ ) of the Cu(001) surface after deposition of 0.01 ML of Pd at room temperature. The large protrusions are incorporated Pd atoms. Right side, X and Y position of a diffusing Pd atom at 62 C over 160 seconds.

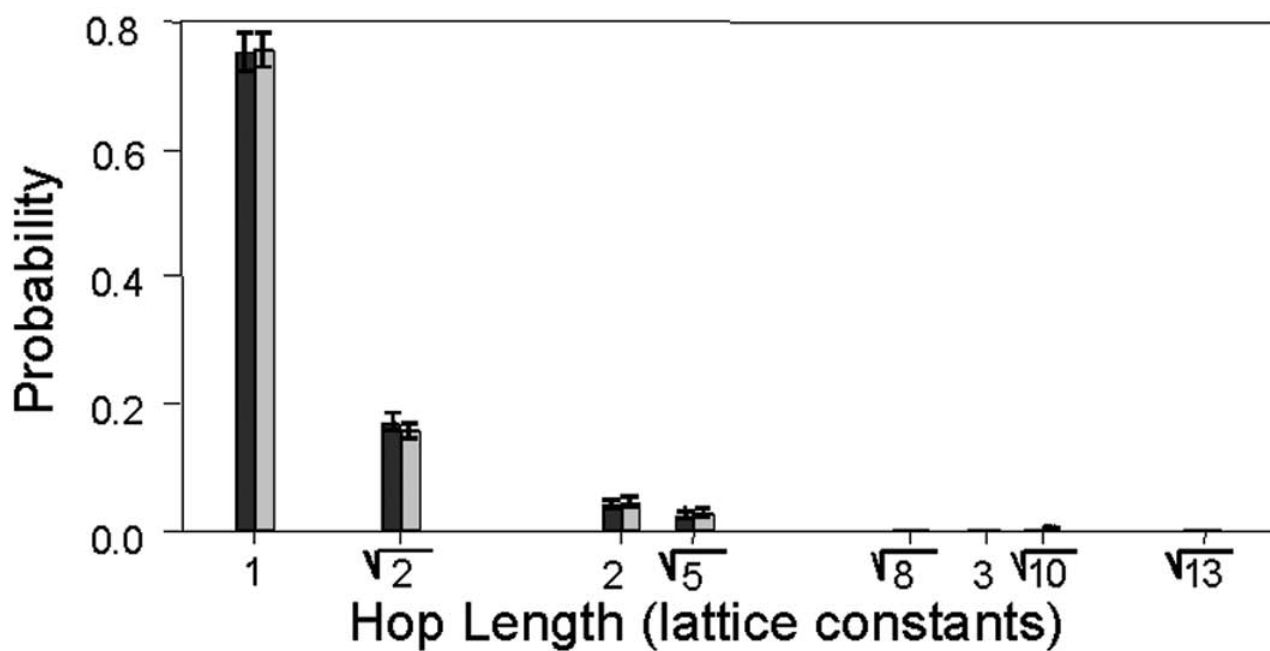


**Figure 2.** Distribution of jump lengths at 62 C. Dark bars represent experiment and shaded bars are simulation.

## The Evolution of Self-assembled Domain Structures on Solid Surfaces

by *R. A. Plass, N. C. Bartelt, and G. L. Kellogg*

**Motivation**—Competing attractive and repulsive inter-atomic interactions can lead to the spontaneous formation of ordered domain patterns in widely varying chemical and physical systems. The potential use of such patterns as templates for the fabrication of nanostructures has fostered considerable interest in the underlying self-assembly physics. Theoretical models and simulations predict the possibility of controlling pattern geometry, long-range order and feature size with varying coverage and temperature, but, until now, experimental verification of these models has remained elusive.

**Accomplishment**—We have discovered a new self-assembling system — two surface structures of Pb on Cu — which displays a pattern evolution and temperature dependence in close agreement with theoretical predictions. Real-time, real-space images recorded using the Low Energy Electron Microscope (LEEM) show exactly how the structures are generated, how they self-assemble, and how the phases transform. The close agreement between experiment and theory allows us to probe the key inter-atomic force parameters involved in the process.

The two Pb on Cu structures that exhibit this remarkable behavior are a disordered Pb/Cu surface alloy, produced by Pb vapor deposition onto clean Cu(111), and a Pb overlayer phase, produced by continued deposition after the alloy structure has covered the surface. Figure 1 shows models of the atomic structure of the two phases. Figure 2 shows a sequence of LEEM images illustrating the growth of the overlayer structure (bright) at the expense of the surface alloy structure (dark) during Pb deposition at

673 K. The most striking feature of this sequence is the pattern evolution from circular islands (with an average diameter of 67 nm) to stripes and then to circular holes within the Pb overlayer matrix. This sequence of domain patterns, typically referred to as droplets, stripes, and inverted droplets, has been predicted to be a general property of domain formation on solid surfaces. Our results represent the first clear observation of the expected sequence of domain patterns with changing area fraction. The data agree well with the predicted positions of the droplet to stripe phase transitions [Ng and Vanderbilt, PRB 52, 2177-2183 (1995)]. We propose that the repulsive interactions arise from a stress difference between the two phases and determine its magnitude from analysis of our data. Our results define the parameters required for self-assembly on solid surfaces and allow us to predict other systems for which the process should occur.

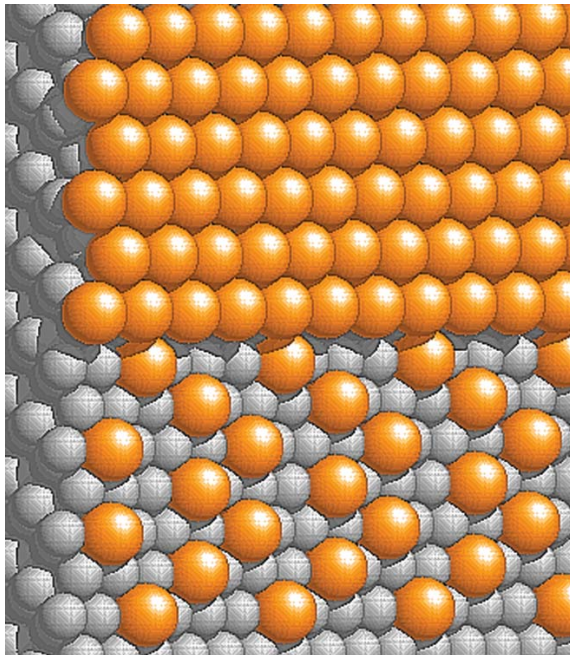
**Significance**—The spontaneous formation of two-dimensional domain structures with controllable shapes and dimensions is an intriguing phenomenon with significant potential applications in patterning nanotechnologies. Our observations show unambiguously that self-assembled lead structures on the close-packed surface of copper encompass the complete range of phases expected when long- and short-range forces compete. The system is simple enough to characterize the composition and structure of the component phases in atomic detail and yet displays the same cooperative behavior found in much more complicated magnetic and chemical systems.

---

**Sponsors for various phases of this work include:** BES, LDRD

**Contact:** Gary L. Kellogg, Surface and Interface Sciences, Department 1114

Phone: (505) 844-2079, Fax: (505) 844-1197, E-mail: glkello@sandia.gov



**Pb Overlayer  
Phase**

**Pb/Cu Surface Alloy  
Phase**

**Figure 1.** Schematic representation of the two Pb/Cu surface phases that exhibit nanoscale self-assembly. (Figure courtesy of P. J. Feibelman.)

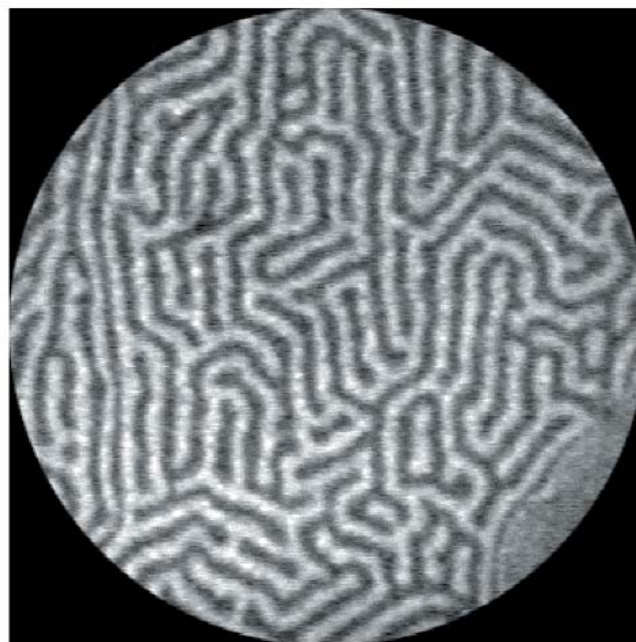


**Figure 2.** LEEM images of Pb/Cu surface phases at 673 K showing pattern progression with increasing amount of Pb ( $2.3\ \mu$  field of view). The pattern evolves from droplets (with an average diameter of 67 nm) to stripes to "inverted droplets" as predicted by theory.

## The Complex Origins of Intrinsic Stress in Thin Films

by J. A. Floro, S. J. Hearne, P. Kotula, and J. A. Hunter

**Motivation**—Thin films of metals, semiconductors, and ceramics often exhibit internal stress levels far in excess of the yield stress of the equivalent bulk materials. These stresses can have many deleterious effects, including buckling, spallation, fracture, voiding, or roughening of the film. The physical origins of film stress clearly need to be understood, but progress in this area has been extremely difficult using standard approaches where films are grown, and then the stress is measured *ex situ*.

**Accomplishment**—We have used our Multi-beam Optical Stress Sensor (MOSS) to perform ultra-sensitive stress measurement during non-epitaxial thin film growth under extremely clean conditions. The evolution of stress during island nucleation, growth, coalescence, and grain growth has been measured in metallic and semiconducting films, crystalline and amorphous films, and over a wide range of material melting points. In all cases we observed a complex but generic behavior for the stress evolution (see Fig. 1) that is intimately related to the evolving microstructure in the growing film. As the film microstructure evolves, a dynamic competition between different stress generation mechanisms yields the overall complex stress behavior. In all the films studied, there is clearly a competition between capillary effects that generate compressive stress, and island coalescence effects that generate tensile stress. We recently developed a new model that explains how additional compressive stresses may result from excess atom flows from the surface into the film interior, driven by the presence of a deposition flux. This model is the first to explain a range of experimental results. In addition to describing the origins of

compressive stress itself, the model explains why compressive stress increases when deposition rate is decreased. An unusual *reversible* stress relaxation frequently observed when deposition is interrupted and then resumed also arises naturally within our model.

We have used deposition interruptions during film growth to explore the importance of irreversible relaxation phenomena. Because the same complex stress evolution is observed in films where relaxation is clearly suppressed, we have disproven the controversial hypothesis that relaxation processes dominate the complex evolution of film stress during growth.

Lastly, we have shown that film/interface effects are important during the island growth stage. Shear at the film/substrate interface can relax stress efficiently for weakly-bound films (see Fig. 2), while strongly-bound films can relax only by more conventional plasticity processes. We have also demonstrated that the chemical interaction between highly reactive films with the substrate in the first few atomic layers of film can significantly affect stress evolution.

**Significance**—From a reliability standpoint, our work has further elucidated the intrinsic microstructural mechanisms that generate stresses in non-epitaxial films. Understanding these mechanisms is critical to learning how to control and modify stresses in thin films to avoid failure during or after deposition. Our experiments have also stimulated scientific modeling efforts aimed at understanding island coalescence, surface-mediated creep, and the kinetics of film formation.

---

**Sponsors for various phases of this work include:** BES, Nuclear Weapons/Science and Technology

**Contact:** Jerrold A. Floro, Surface and Interface Sciences Department, 1114

Phone: (505) 844-4708, Fax: (505) 844-1197, E-mail: [jaflo@sandia.gov](mailto:jaflo@sandia.gov)

---



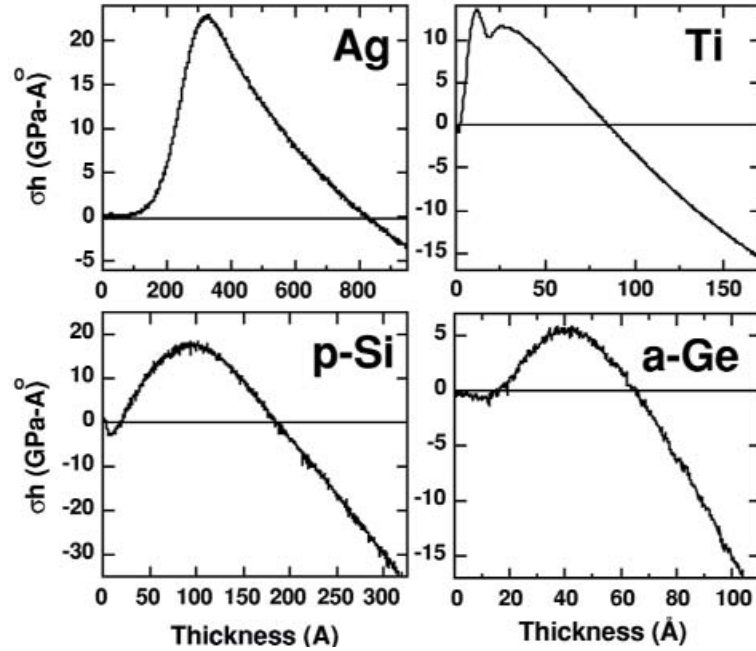


**Figure 1.** Stress evolution during evaporative deposition of Ag, Ti, poly-Si and amorphous Ge thin films on silica. Positive values of the stress-thickness product ( $\sigma h$ ), which is proportional to wafer curvature, denote tensile stress.

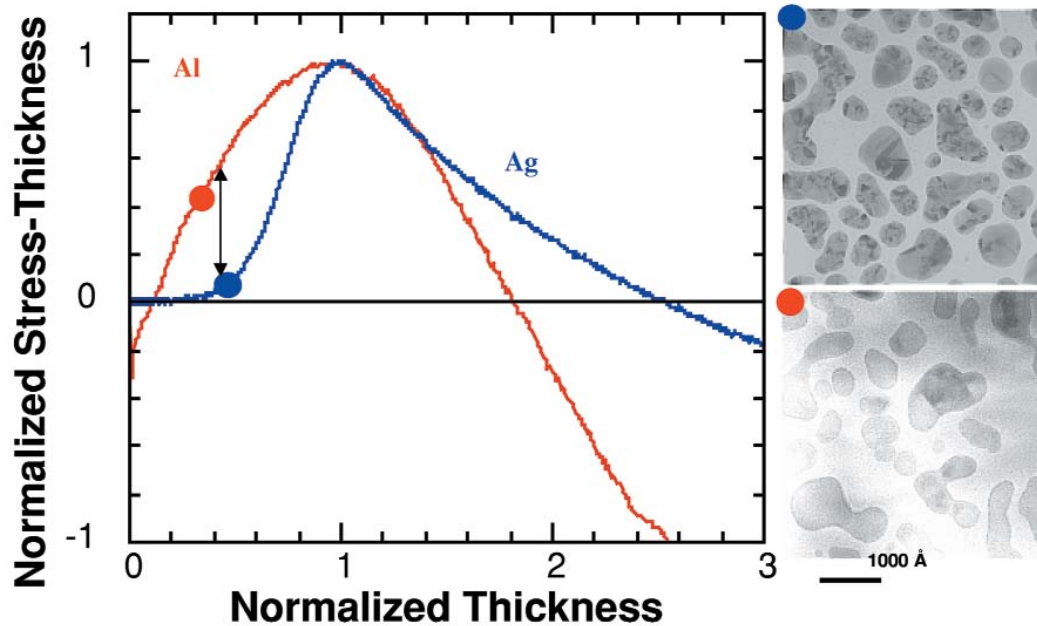


**Figure 2.** Ag and Al exhibit much different stress evolution in the early stages of growth (see arrowed region), despite the similar microstructures. This results from shear at the weak Ag/SiO<sub>2</sub> interface, which is suppressed in the much stronger Al/SiO<sub>2</sub> interface.

# Nanostructured Materials



## Formation of "Magic"-sized Metal and Semiconductor Nanoclusters

by *J. P. Wilcoxon and P. N. Provencio*

**Motivation**—Using High Performance Liquid Chromatography (HPLC), we have shown these clusters to have greater monodispersity than purified  $C_{60}$ . In traditional solution based colloidal synthesis, kinetic factors determine the final size and size-dispersion of the colloids (nanoclusters), leading in most cases to either log-normal or even power-law size distributions. However, the possibility exists that when clusters are grown slowly enough from atomic species, thermodynamically favored or "magic" sizes/structures will dominate, characterized by the closing of an icosohedral shell as atoms are added to the cluster. The key to this process is control of both the rate of atomic accretion so that atoms can diffuse and find equilibrium positions on the growing cluster and a medium which allows the clusters to "equilibrate" via collisions and atomic exchange with other clusters to favor these "magic" sizes. Unfortunately, neither of these two conditions can be achieved in vacuum or inert gas cluster-beam sources and thus metastable structures are also found in similar abundance to the "magic" closed shell icosohedra.

**Accomplishment**—We have learned to control the growth rate of nanoclusters from reduced atomic species contained in inverse micelles, (the nucleation centers) and using using high pressure liquid chromatography (HPLC) for precise size feedback. This has allowed us to form special sized nanocrystals to form spontaneously via micellar diffusion, micelle fusion and atomic exchange, and, finally, cluster equilibration on time scales of a few days to several weeks. Using HPLC, we have shown the clusters to have greater monodispersity than purified  $C_{60}$ . We have demonstrated that this

phenomenon is universal, occurring in a wide variety of simple metals such as Au, Ag, Pt, Rh, Cu and Ni. We have then purified the nanocrystals from the inverse micelles, essentially removing alternative nucleation sites (i.e., the micelles). Employing these perfectly monodisperse, nanocrystalline seeds in a solvent, we then feed in a stock of a atom of the same type at a very slow rate while controlling their reduction to the zero valence state and using a passivating agent to control the deposition/growth process. The feedstock atoms then deposit onto the pre-existing perfect nanocrystal "seeds" growing shell-by-shell by a process akin to two dimensional epitaxially growth on substrates. The shell-by-shell growth can be demonstrated by the entire size distribution growing uniformly larger ( Fig. 1), leaving none of the smaller seeds behind.

**Significance**—This is the first demonstration of the controlled solution growth of nanocrystals via heterogeneous nucleation on "seed" nanocrystals and provides the first rational synthetic strategy for growing both homo- and poly-atomic (core/shell) species. The universality of the thermodynamic stability of the nanocrystal seed growth process ensures an unlimited range of applicability of the process, requiring only an oil-soluble coordinating solvent (the passivating agent) and a source of oil-soluble, reduceable atomic species for deposition. The controlled atomic feed rate and perfect dispersion of both nanocrystal seeds and feedstock eliminates the possibility of homogeneous nucleation of new nanocrystals. The enormous surface area of the seed population of the nanocrystals guarantees uniform deposition only the seeds.

---

**Sponsors for various phases of this work include:** BES

**Contact:** Jess P. Wilcoxon, Nanostructures and Advanced Materials Chemistry, Department 1122

Phone: (505) 844-3939, Fax: (505) 844-4045, E-mail: jpwilco@sandia.gov

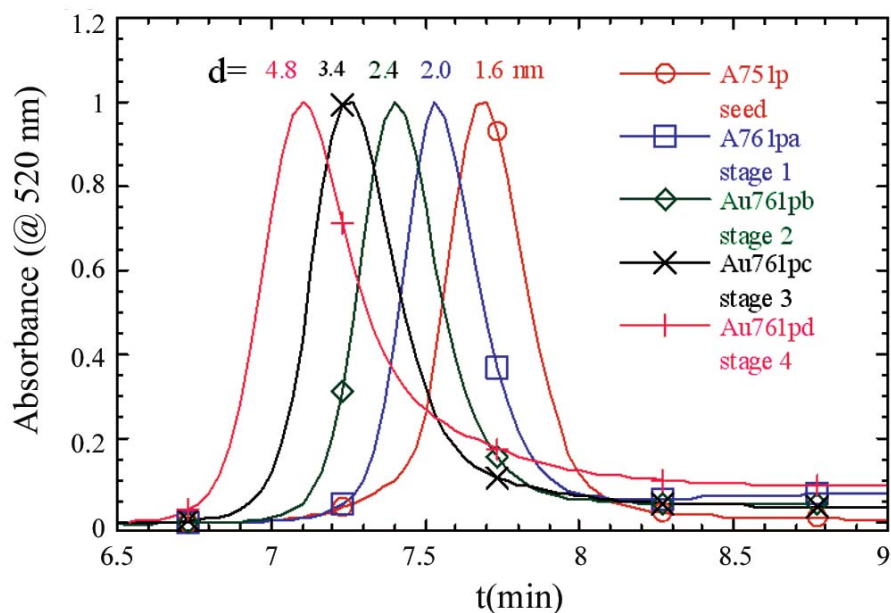


**Figure 1.** Au cluster optical absorbance vs flow time  $t$  for HPLC determination of magic size clusters from monodisperse seeds. The relationship  $t \sim \log(\text{cluster volume})$  was used to obtain the sizes indicated which closely match those expected for completion of successive shells of atoms.

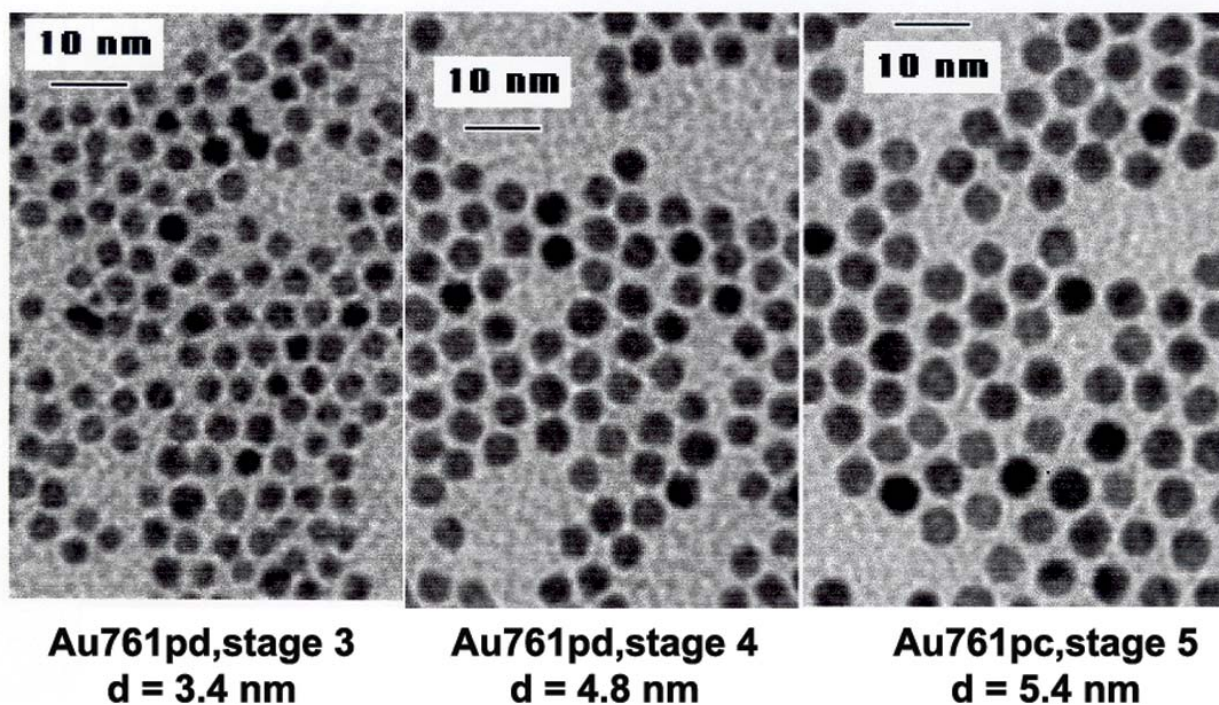


**Figure 2.** TEM of three of the growth stages of the clusters shown in Fig. 1.



## Giant Magnetic Anisotropy in Field-structured Dipolar Nanocomposites

by *E. L. Venturini, J. E. Martin, J. P. Wilcoxon, J. G. Odinek and P. N. Provencio*

**Motivation**—Composite materials consisting of structured nanoparticles in an amorphous continuum can exhibit unique, anisotropic physical properties when the particles are strongly coupled. Examples include composites containing arrays of closely spaced metallic, dielectric or magnetic nanoparticles. In particular, structured arrays of mobile magnetic nanoparticles will form in an external magnetic field when the dipolar interaction energy between the particles exceeds the thermal energy of the system. Subsequent "freezing" of the particle array in the host matrix creates a strongly anisotropic composite material that is expected to exhibit distinctive properties not achievable with macroscopic particles. The purpose of this work is to investigate and understand these properties.

**Accomplishment**—The system used in this study consisted of dilute (0.5 vol%) 10 nm-diameter magnetite ( $\text{Fe}_3\text{O}_4$ ) particles plus surfactant suspended in an aqueous solution. Nanoparticles of this size or smaller have a single magnetic domain and act as large magnetic dipoles (giant spins) that rotate freely in the absence of a strong magnetic field. Linear chains were formed by applying a static magnetic field (typically 1000 Oe) at room temperature and exploiting the dipolar coupling between nanoparticles to drive chain formation. The structured solution was then frozen by slow cooling in the static field.

The effect of collective behavior in a structured nanoparticle composite can be illustrated by comparing magnetic hysteresis loops before and after structuring. Upon structuring, the dipolar coupling among nanoparticles in the composite results in a strongly enhanced local magnetic field for a particular orientation. This effect is

illustrated in Fig. 1 where we compare hysteresis loops at 200 K for an unstructured nanoparticle composite (solid triangles) with a structured composite containing linear chains of nanoparticles oriented parallel (open circles) and perpendicular (open squares) to the external field. At low field the system exhibits a strongly enhanced response along the nanoparticle chains and a diminished response normal to the chains compared with the unstructured material.

The giant anisotropy of the structured nanocomposite can be shown by taking the ratio of the magnetic response parallel to the chains to that of the unstructured sample. This ratio is plotted versus field in Fig. 2 where the low-field maximum reflects a  $6.2\times$  enhancement. Similarly, the ratio of the response perpendicular to the chains to that of the unstructured sample reaches a minimum of 0.7 at low field; in this orientation the dipolar coupling reduces the local field felt by the nanoparticles.

**Significance**—Structured arrays of magnetic nanoparticles formed by dipolar coupling exhibit giant magnetic anisotropy that cannot be duplicated using macroscopic particles. Our study of composites containing linear chains of 5  $\mu\text{m}$ -diameter, multidomain Fe particles had less than half the anisotropy of these monodomain nanoparticle composites. The strongly enhanced local fields in structured nanoparticle arrays lead to magnetic saturation in smaller external field plus greater coercivity and a larger remanent moment at low temperature. Applications include high-density memory, field sensors with orientation dependence, and anisotropic, nonlinear conductors exploiting electron tunneling between metallic nanoparticles.

**Sponsors for various phases of this work include:** BES

**Contact:** Eugene L. Venturini, Nanostructures and Advanced Materials Chemistry, Department 1122  
Phone: (505) 844-7055, Fax: (505) 844-4045, E-mail: elventu@sandia.gov

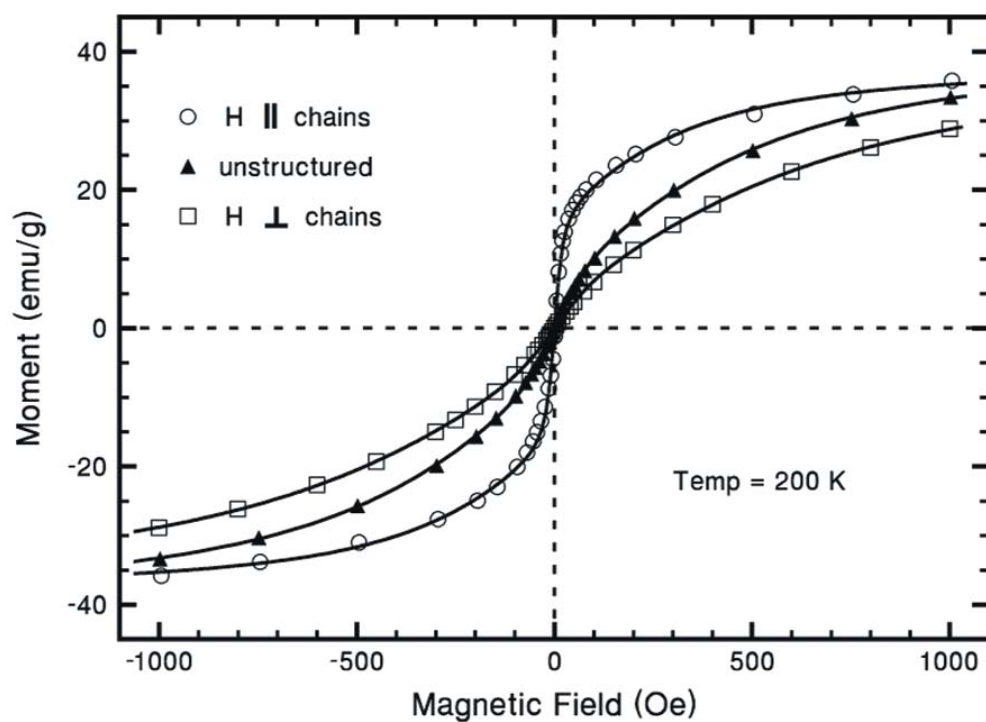


**Figure 1.** Magnetization hysteresis loops at 200 K for unstructured and field-structured dipolar nanocomposites containing 10 nm-diameter magnetite ( $\text{Fe}_3\text{O}_4$ ) particles.

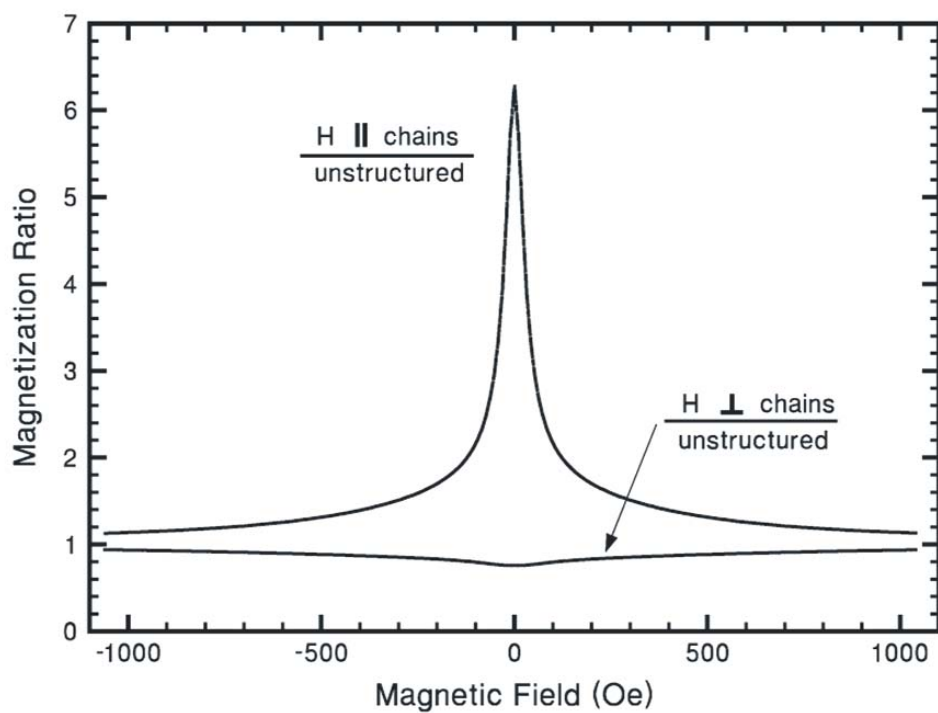


**Figure 2.** Magnetization ratios showing giant anisotropy parallel and perpendicular to the chains of  $\text{Fe}_3\text{O}_4$  nanoparticles compared to unstructured composites.

## Colossal Thermoresistance and Piezoresistance Observed in Field-structured Composites

by J. E. Martin, J. Odinek, R. Anderson and D. Adolf

**Motivation**—We have developed a novel class of materials we call Field-Structured Composites (FSCs) that consist of electrically conductive magnetic particles in a polymeric resin. As the polymeric resin is cured, the particles are subjected to a magnetic field that causes them to aggregate into chain-like structures, that are then immobilized by the curing resin. These chains traverse the material, forming electrically conducting pathways that are expected to be remarkably sensitive to the specific volume and strain state of the composite, and thus might be ideally suited to the development of inexpensive resistance-based sensors. In this work we are both exploring the phenomenology of these materials and starting to understand their transport physics.

**Accomplishment**—We have developed an epoxy resin FSC containing Au-coated Ni particles whose resistivity increases reversibly by a factor of one billion upon heating from room temperature to 100 °C (Fig.1). FSCs made using silicone resins are found to have a permanent memory of the cure temperature, which is manifest as a conductor-insulator transition (Fig. 1). Near this transition temperature the sample resistance can easily change by a factor of 100 over 1 °C. We have also demonstrated an epoxy FSC whose resistivity reversibly decreases by a factor of nearly one trillion over a uniaxial strain range of 6%. For a 1 mm thick sample a

compression of only 20 nm would result in a 1% resistance change. This piezoresistance was observed both above and below the glassy transition temperature of the resin, and we have shown that by controlling the resin elastic modulus the stress range over which the resistance changes can be varied over a wide range (Fig. 2). We have started to model these transport effects with site percolation studies of simulated FSC structures, which show that such large effects are a direct consequence of the low dimensionality of the particle aggregates.

**Significance**—FSCs show tremendous potential for the development of inexpensive resistance-based sensors. Sensing stress, strain, pressure, and temperature are obvious, but more interesting possibilities are sensing chemical vapors and magnetic fields. At this time carbon black-filled composites are used as chemical vapor sensors, called "chemiresistors", but these random particle composites have poor response unless prepared very near the particle percolation threshold, which is difficult to do. FSCs can be prepared with essentially any particle concentration, have tailorable thermoresistance, and exhibit tremendous response, due to the one-dimensional particle chains. We are very optimistic about the potential of FSCs for sensors, and have started to test these materials as chemiresistors.

---

**Sponsors for various phases of this work include:** BES

**Contact:** James E. Martin, Nanostructures and Advanced Materials Chemistry, Department 1122

Phone: (505) 844-9125, Fax: (505) 844-4045, e-mail: jmartin@sandia.gov

---

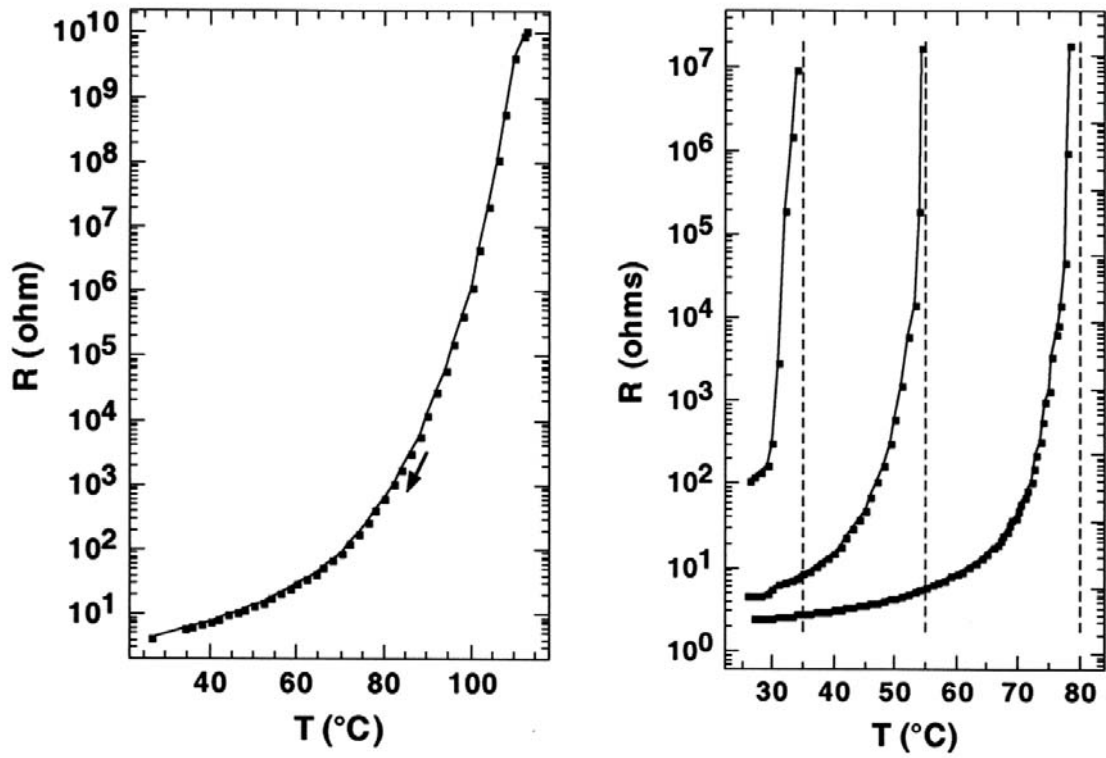


**Figure 1.** Thermoresistance of an epoxy FSC (left). Memory of the cure temperature (shown by vertical lines) occurs in silicone FSCs, due to small cure shrinkage.

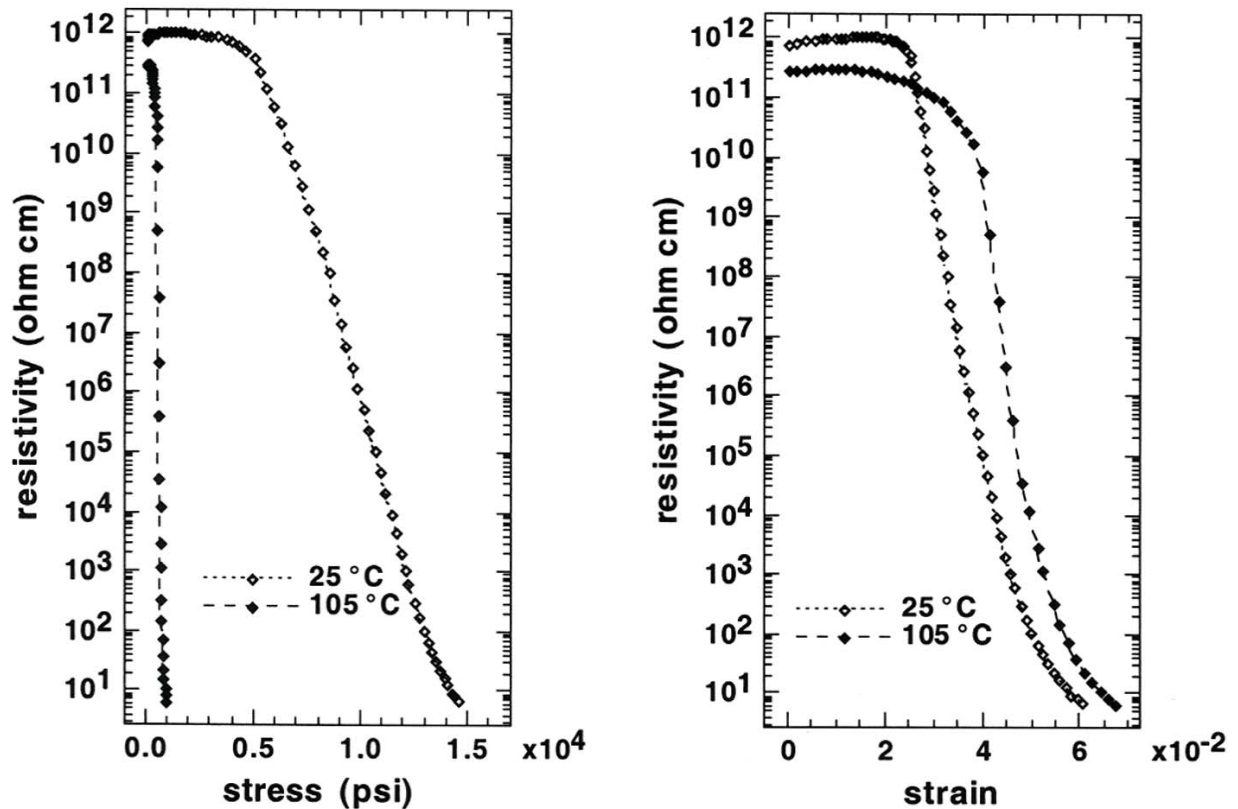


**Figure 2.** Piezoresistance of an epoxy FSC measured above and below the 90°C glass transition. A master curve nearly obtains when strain is the abscissa.

## Precise Control of Carbon Nanotube Diameters Grown Directly onto Substrates

by *M. P. Siegal, D. L. Overmyer, P. P. Provencio, and F. H. Kaatz*

**Motivation**—Carbon nanotubes represent a unique form of pure graphene-based materials with intriguing physical properties and a plethora of potential applications, ranging from room-temperature cold-cathode electron field-emitters to nanoelectrodes for electrochemical sensing to nanometer-sized hollow tubes for mass separation and filtration. We collaborated on the first demonstration of highly-aligned, multiwalled carbon nanotube growth using hot-filament, plasma-enhanced chemical vapor deposition, CVD (Science 1998). We are now pursuing simpler growth methods with improved reliability and scaleability.

**Accomplishment**—We grow multiwalled carbon nanotubes using a simple thermal CVD process at atmospheric pressure from a mixture of acetylene and nitrogen gases. Figure 1 shows scanning electron microscopy (SEM) images of nanotubes grown on Si, with outer diameters ranging from 5 - 300 nm controlled primarily by growth temperature, varying from 630 - 790 °C. Transmission electron microscopy (not shown) finds that the hollow inner core diameters of these nanotubes range from 2 - 12 nm. Note the superior uniformity of diameters within each sample. Growth at lower temperatures yields no carbon structures; growth at higher temperatures yields tubular-like  $\mu\text{m}$ -sized cluster structures directly from the gas phase, independent of the catalyst used. We grew the nanotubes shown in Fig. 1 on Si(100) substrates using 4 nm thick sputtered Ni as the catalyst. A 50 nm thick W diffusion barrier prevents unwanted silicidation. We reduce the Ni/W/Si(100) substrates in flowing CO at 600 °C for one hour, raise the temperature to that desired for growth in N<sub>2</sub>, and then expose the substrates to the growth ambient for 15 minutes. Samples furnace-cool in nitrogen. While this

simple growth method does not directly yield aligned nanotubes, this can be achieved by using templates such as anodized aluminum with arrays of pinholes, like those shown in Fig. 2. Metal catalyst will be electrochemically deposited at the bottom of these pinholes in the resulting Al-oxide layer. Our work defines nanotube growth conditions which will be applied to the use of anodized aluminum templates with predetermined pinhole sizes for growth of aligned multiwalled carbon nanotube arrays with optimal structural integrity. The result will be quasi-ordered highly-aligned nanotubes of any given diameter.

**Significance**—We have achieved precision control of carbon nanotube diameters grown directly onto a substrate. Employing ordered arrays of pinholes formed by anodizing high-purity Al enables utilization of a simple thermal CVD process to fabricate quasi-ordered, highly-aligned arrays of carbon nanotubes. Pinhole diameters can be engineered to match nanotube diameters required for a particular application for enhanced structural integrity. Since multiwalled carbon nanotubes are conductive both electrically and thermally, similar to graphite, these arrays can be used as nanoelectrodes for a wide variety of applications. Nanotubes can be further functionalized via selective metallization and chemical modification to create arrays of nanoelectrodes, permitting, for example, real-time, precise electrochemical analysis of regulated chemicals in ground water. These highly-aligned nanotube arrays can also be used as room-temperature electron sources for miniaturized ion mass mobility microsensors, replacing radioactive beta-emitters in these devices. This source substitution will enable new uses of these microsensors, including biological/medical diagnostic tools.

**Sponsors for various phases of this work include:** Nuclear Weapons/Science and Technology

**Contact:** Michael P. Siegal, Nanostructures and Advanced Materials Chemistry, Department 1122

Phone: (505) 845-9453, Fax: (505) 844-4045, E-mail: mpsiega@sandia.gov



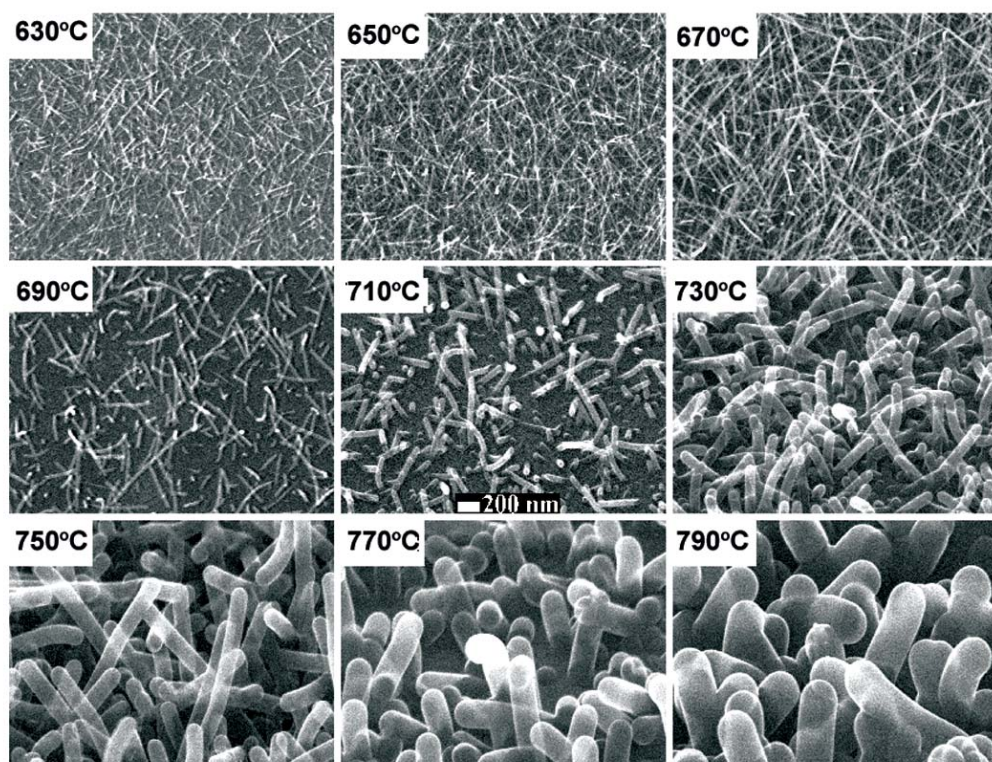


**Figure 1.** SEM images of carbon nanotubes grown at different temperatures by thermal CVD, each for 15 minutes using identical Ni catalyst thicknesses on W-coated Si(100) substrates. Outer (inner) tube diameters range from 5 - 300 nm (2 - 12 nm), as a function of growth temperature.

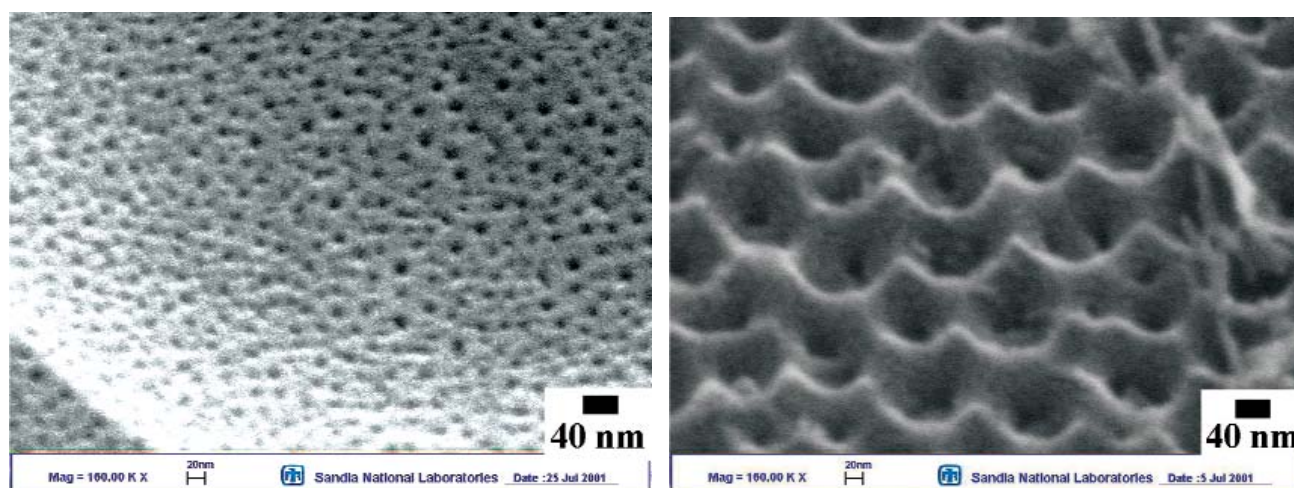


**Figure 2.** SEM images of anodized aluminum to be used as templates for the growth of highly-aligned, quasi-ordered arrays of tightly-packed individual carbon nanotubes. Pinhole diameters shown here range from 10 - 50 nm, and are controlled by varying the acid and voltage used for anodization.

# Biomolecular Materials and Interfaces



## Controlled Switching of Surface Chemistry

by *B. C. Bunker, D. L. Huber, M. A. Samara, J. G. Kushmerick, R. P. Manginell, M. J. Kelly, and C. M. Matzke*

**Motivation**—Sandia is developing integrated microfluidic systems for separating and analyzing biological species such as proteins. As fluid channels get smaller, interactions with channel walls become critical, controlling fluid flow and species transport as mediated by adsorption and desorption from channel walls. The goal of this work is to see whether the chemistry of the solid-liquid interface can be programmed using electrical, optical, or thermal impulses from integrated systems to drive fluids through microchannels or to grab and release desired solution species.

**Accomplishment**—The general strategy for controlled switching of surface chemistry involves functionalizing interfaces with self-assembled monolayers. Species configurations within the monolayers change in response to applied stimuli to modify the surface chemistry. For example, we are collaborating with Professor Fraser Stoddart at UCLA to develop a new class of monolayers that are electrochemically-activated based on molecular machines tethered to Au (Fig. 1). The functional unit in the machine is a cyclophane called the "blue box". In its native state, the central cavity of the box is  $\pi$ -electron deficient and readily adsorbs aromatic molecules such as tetrathiafulvalene (TTF). Oxidation of the TTF turns off these attractive  $\pi$ -stacking interactions, resulting in TTF desorption. The results demonstrate that tethered molecular machines can be programmed to reversibly adsorb or release solution species. Water contact angle measurements indicate that such adsorption can also change interfacial energies to switch interfaces between hydrophobic and hydrophilic states. A second

system under investigation is poly(*n*-isopropyl acrylamide) or PNIPAM tethered to oxide surfaces. PNIPAM undergoes a thermally-activated phase change at 35°C between a hydrophilic, swollen state and a more hydrophobic, collapsed state. UV-visible spectra show that water-soluble proteins such as myoglobin do not stick to the room-temperature state. However, heating the films above the transition temperature results in the rapid adsorption of a protein monolayer. Cooling the films results in protein desorption. A microelectronic "hot-plate" consisting of programmable gold heater wires on a silicon nitride membrane has been developed to exploit the reversible protein adsorption properties of PNIPAM in a microfluidic system (Fig. 2a). Preliminary experiments with fluorescently-tagged myoglobin show that individual heater lines can be addressed to capture (Fig. 2b) and release (Fig. 2c) proteins.

**Significance**—The ability to store "one's and zero's" in solid state microelectronics devices revolutionized the Information Age. The work reported here suggests that integrating such devices with microfluidic systems could have a similar impact on the emerging era of bio- and nano-technologies. Most existing microfluidic systems contain passive components such as chromatographic media that perform a single function in a single state. Incorporation of programmable materials into microfluidic systems means that it may be possible to store both chemical and physical information into interfaces and 3D materials to perform functions such as selective adsorption, active transport, programmable valving, switchable porosity, and reconfiguration of fluidic channels on a chip.

**Sponsors for various phases of this work include:** BES, LDRD

**Contact:** B. C. Bunker, Biomolecular Materials and Interfaces, Department 1140

Phone: (505) 284-6892, Fax: (505) 844-5470, E-mail: bcbunke@sandia.gov



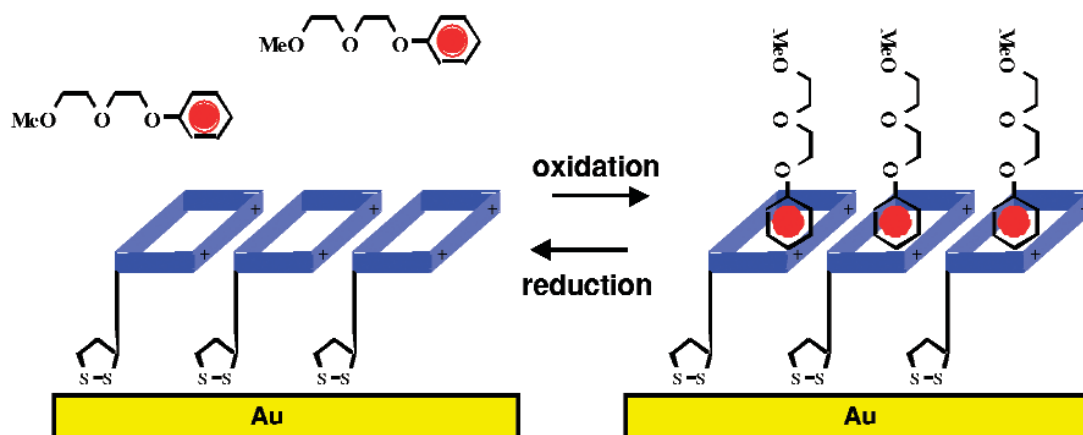


**Figure 1.** Schematic depicting the electrochemical switching of the "blue box". When the box is in its native +4 oxidation state, it adsorbs aromatic species into its central cavity (right). Electrochemical reduction of the box to the +2 state (shown) or oxidation of the aromatic results in desorption of the aromatic (left).

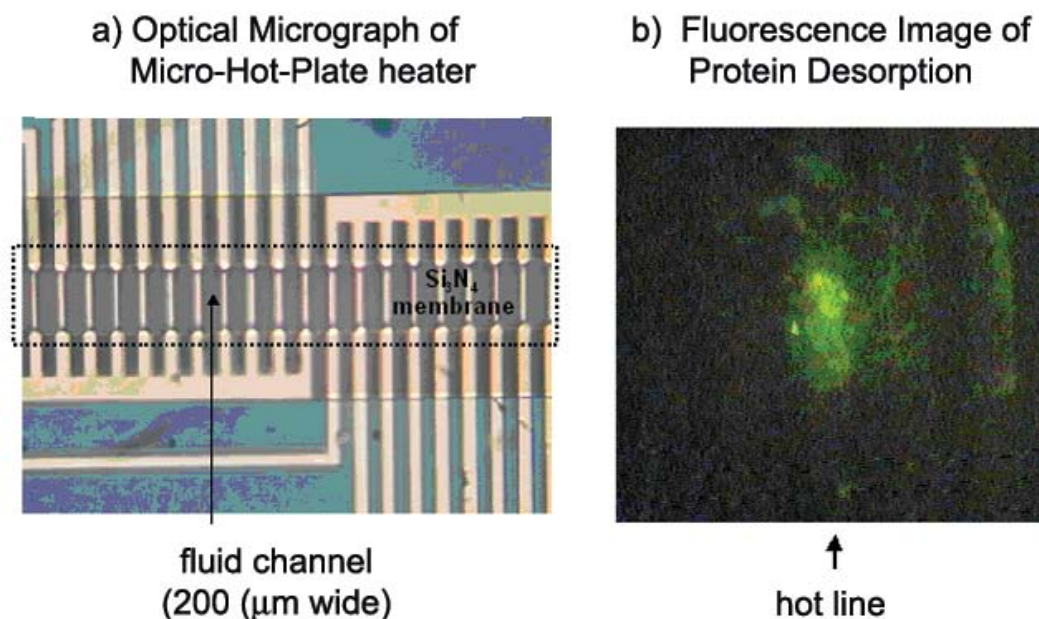


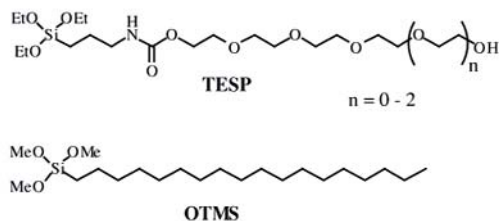
**Figure 2.** a) Optical micrograph of the microheater used to activate PNIPAM films in microfluidic systems. b) Image obtained in a fluorescence microscope of fluoresceine-tagged myoglobin desorption plume leaving a heater line seconds after the heat was turned off. Note that prior to this, myoglobin was only adsorbed on regions coated with PNIPAM that were heated above the transition temperature.

## Self-assembling Materials for Biomaterial Adhesion and Hierarchical Structures

*by D. Y. Sasaki*

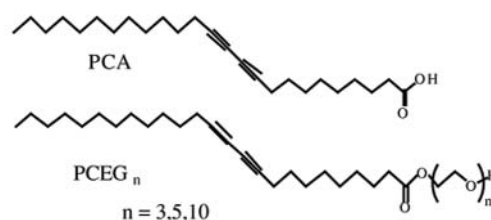
**Motivation**—Functionalized surfactants allow us to prepare novel self-assembled materials for a broad range of applications. Materials that range from biocompatible surface coatings on semiconductors to organic-inorganic hybrid composites with unique optical properties can provide routes towards advances in areas such as BioMEMS and remote sensor materials. Through a judicious selection of surfactant functionality and structure we hope to prepare unique surface coatings and structural templates for composite materials with hierarchical order.

**Accomplishment**—Over the past year we have examined the biocompatibility and surface passivation properties of several coating materials in an effort to improve flow properties of the microfluidic system within the Biocavity Laser device. Self-assembled monolayers (SAM) of alkoxy-silanes offered several desirable structural properties, which included optical clarity, nanometer level thickness, robustness, ease of preparation, and reproducibility. Bioadhesion properties of these coatings were tested against proteins (albumin, fibrinogen) and glial cells under static and fluidic systems (Biomaterials in press). One of the findings of this work was that the hydrophilic oligoethylene glycol SAM, prepared from TESP [N-(triethoxysilylpropyl)-O-polyethylene oxide urethane], is biocompatible under cell culture conditions but resistant to cell adhesion under fluidic conditions. The hydrophobic alkane surface, on the other hand,



prepared from OTMS, was incompatible for cell proliferation under static conditions but induced biofouling of cells under fluidic conditions. The results indicate that solution phase proteins play a major role in the modification of surfaces for cell adhesion.

In a separate research project, diacetylene surfactants with oligoethyleneglycol headgroups were prepared for use as structural templates in sol-gel hybrid materials synthesis. The size of the oligoethylene glycol headgroup allowed us to tune the micellar phase from hexagonal to cubic to lamellar structures. The diacetylene unit also organized neatly in the micellar supramolecular structures allowing facile polymerization with UV light. The composite material thus exhibited not only unique mesoporous structure but also optical properties not observed before with polydiacetylenes (in Nature 2001, 410, 913).



**Significance**—Understanding the bioadhesion properties of SAM coatings on semiconductor materials is of utmost importance for the current development of BioMEMS devices at Sandia. Our ability to design and synthesize surfactants with unique functionality will allow us to prepare hybrid materials that have not only highly ordered nanostructure but also exhibit optical function.

**Sponsors for various phases of this work include: LDRD, BES**

**Contact:** Darryl Y. Sasaki, Biomolecular Materials and Interfaces, Department 1140  
Phone: (505) 845-0824, Fax: (505) 844-5470, E-mail: [dysasak@sandia.gov](mailto:dysasak@sandia.gov)

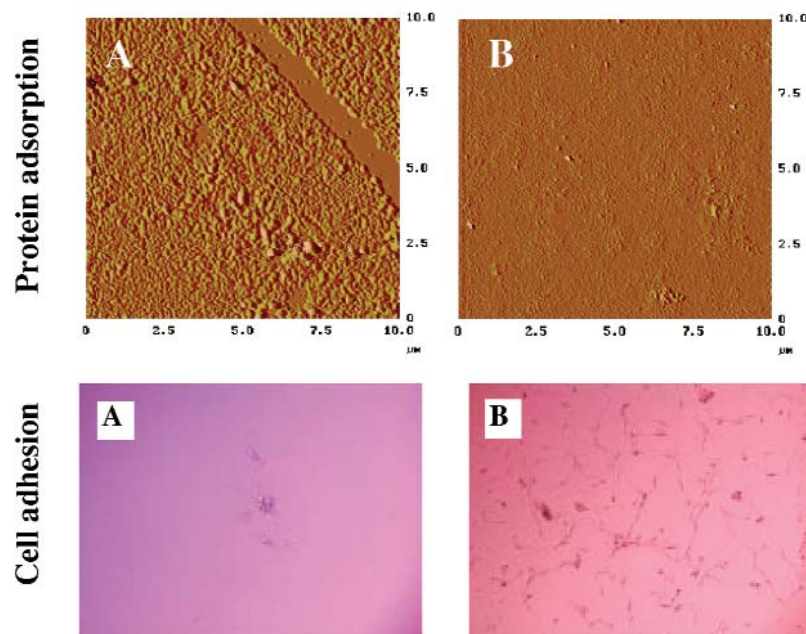


**Figure 1.** Above: AFM images of bovine serum albumin adsorbed onto (A) a hydrophobic alkane SAM coating and (B) hydrophilic oligoethylene glycol SAM coating. Below: Those same surfaces, exposed to glioblastomas under cell culture conditions, displayed poor cell adhesion and proliferation for the hydrophobic surface but good biocompatibility with the hydrophilic surface.

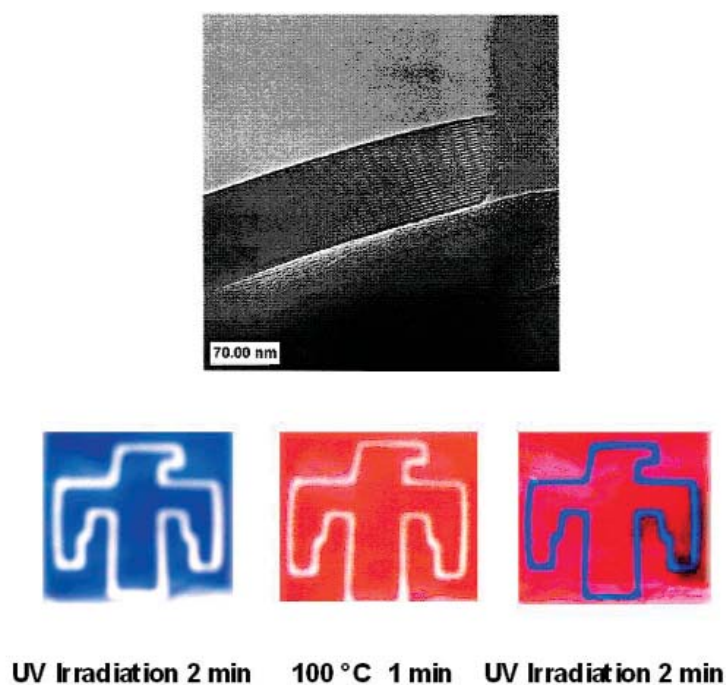


**Figure 2.** Above: A TEM image of a PCEG5/silica sol-gel material showing the highly ordered and oriented porosity. Below: A PCEG/sol-gel material after UV exposure with a thunderbird mask, followed by heat treatment, then another dose of UV irradiation.

## A Study of Cell and Protein Adhesion to SAM-coated Semiconductors

by *Jim D. Cox, Darryl Y. Sasaki, Anthony McDonald and P. L. Gourley*

**Motivation**—Growing interest in BioMEMS devices has brought on new issues involving interfacial phenomena of biological materials with semiconductor surfaces. One such device is the biocavity laser in which flowing cells interact with semiconductor surfaces. A technical problem is that the cells adhere to the surface and prevent fluid flow after a period of time. We undertook an investigation of the binding interactions of cells and proteins to semiconductor surfaces used in these microcavity lasers to determine how adhesion and biofouling can be attenuated using readily prepared coatings of thin organic films.

**Accomplishment**—Hydrophobic (alkane) and hydrophilic (oligoethylene glycol) coatings were deposited onto oxidized silicon and gallium arsenide by various techniques: self-assembled monolayers (SAM), Langmuir-Blodgett (LB), and spin-casting. Coated and bare surfaces were exposed to media containing cells (astrocytes, glioblastomas) and proteins (serum albumin) in both flowing and static experiments to evaluate kinetic and thermodynamic adhesion phenomena. AFM and optical microscopy were used to characterize the coatings and subsequent biofilm formation to evaluate materials biocompatibility.

Cells were flowed through a microfabricated structure composed of glass and semiconductor materials that formed an array of microchannels. If surface adhesion is strong, biofouling of the microchannels will occur resulting in reduced fluid flow rates. In addition to the measurement of flow rates, post mortem analyses of the glass and semiconductor surfaces with optical microscopy were conducted to determine binding patterns that lead to biofouling. The results summarized in Figs. 1 and 2 show that surfaces coated with hydrophilic SAM layers are much

more resistance to biofouling than similar surfaces coated with hydrophobic layers.

Cell adhesion and biofouling were shown to be dependent not only upon surface functionality but also on kinetic interactions of the biomaterial to the surface. Under flow conditions, astrocytes and glioblastomas exhibited little biofouling behavior on the hydrophilic TESP surface but strong channel clogging with the hydrophobic surface. These studies motivate future investigations of cellular adhesion on composite surfaces of hydrophilic and hydrophobic domains as well as complex functionality to further understand cell and protein adhesion.

**Significance**—Creating a smooth flow of biological cells through a microscopic channel in an optical device is far from a simple proposition. The problem is encountered whenever scientists try to merge biological materials with microfabricated structures. These materials are poorly suited to each other. Proteins are large, sticky molecules that tend to adhere to glass, metal and semiconductor surfaces, forming biofilms that foul the devices and quickly compromise their performance. Our device quickly demonstrated this problem. When we flowed the astrocytes and glioblastoma cells through our channels, they stuck on the downstream side of the channels. Within a few minutes the device was severely clogged. Surfaces coated with hydrophilic SAM layers help to minimize this problem and are preferred over hydrophobic coatings. These layers increase fluid velocity and minimized cell sticking. We do not, however, consider the problem solved. Even with the surface treatments the operation time of our biocavity laser is extended only a factor of 3. Additional means for preventing cell and protein adhesion are under investigation.

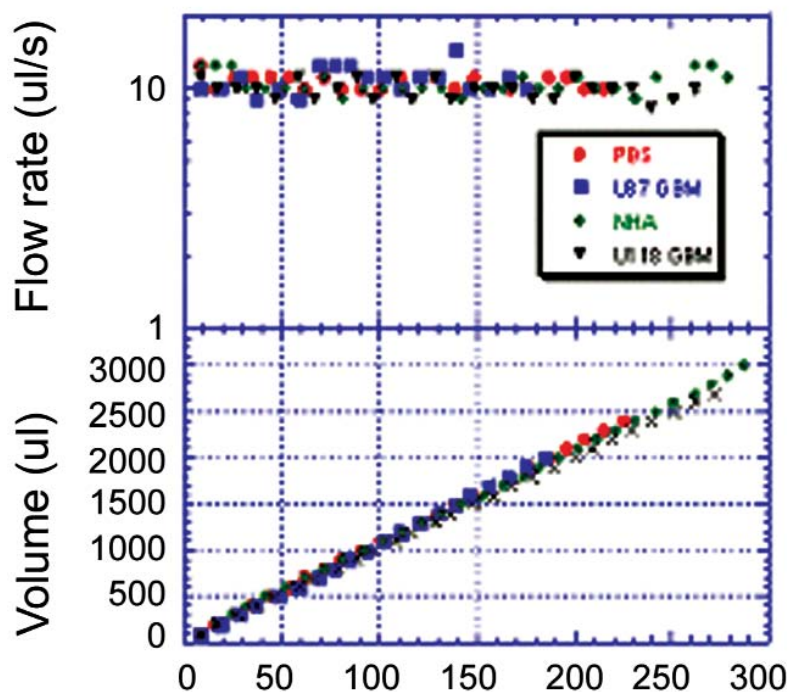
**Sponsors for various phases of this work include:** BES

**Contact:** P. L. Gourley, Biomolecular Materials and Interfaces, Department 1140

Phone: (505) 844-5806, Fax: (505) 844-5470, E-mail: [plgourl@sandia.gov](mailto:plgourl@sandia.gov)



## Cells flowing across hydrophilic Surfaces



## Cells flowing across Hydrophobic Surfaces

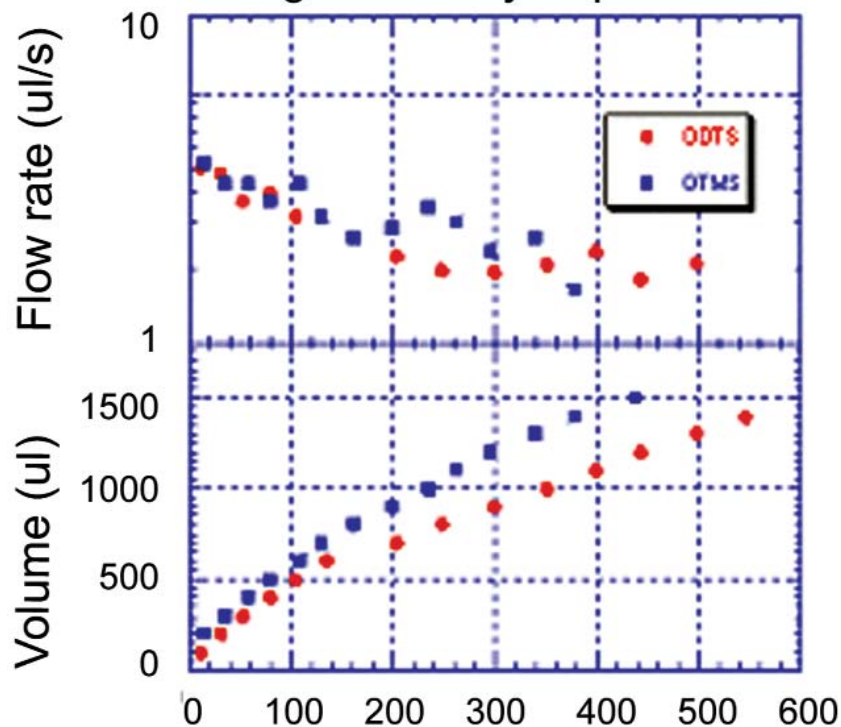


**Figure 1.** Flow rates and flow volume of solutions containing glioblastoma cells through microfluidic devices coated with hydrophobic (OTMS) and hydrophilic (TESP) self-assembled monolayers.

# Ferroelectric Materials





## Manifestations of Quantum Fluctuations in Ferroelectrics

by G. A. Samara

**Motivation**—The occurrence of transitions in ferroelectrics (FEs) is determined by a competition between cooperative, long-range forces and fluctuations. At high temperature ( $T$ ), these fluctuations dominate and there is no ordering; but, on lowering  $T$  the fluctuations decrease and eventually the ordering forces win out, and the system orders at  $T_C$ . On the other hand, at sufficiently low  $T$ , quantum fluctuations, or zero-point motions, can strongly influence the response leading to new critical exponents, the suppression of  $T_C$  below its classical value, and ultimately the complete suppression of  $T_C$ . As there are no known ferroelectrics with sufficiently low  $T_C$ s, experimental study of these effects necessitates that  $T_C$  be shifted down to the appropriate range by application of external fields. The usual approach using chemical substitution to shift  $T_C$  introduces compositional fluctuations, clustering, and breaks translational symmetry. These effects change the interaction parameters of the system, and it is not clear that they can be neglected. We are using a different approach, namely the application of hydrostatic pressure as we now demonstrate.

**Accomplishment**—Figure 1 shows the dielectric response on a Ca-doped  $\text{KTa}_{0.977}\text{Nb}_{0.023}$  crystal. The addition of Nb induces a FE transition in  $\text{KTaO}_3$ . The peak in  $\epsilon'(T)$  defines  $T_C$ . There is a pressure-induced FE-to-relaxor (R) crossover at  $\sim 5$  kbar (Phys. Rev. B 61, 3889, 2000), but the important new result is the vanishing of the phase transition at 9.2 kbar. One of the consequences of the suppression of  $T_C$  is the presence of a special critical point, namely  $T_C = 0$  K. This point, referred to as the *quantum*

*displacive limit*, is characterized by special critical exponents. Specifically, theory shows that in the high  $T$  phase  $\epsilon'(T)$  is given by  $(\epsilon' - \epsilon'_\infty) = C(T - T_C)^{-\gamma}$ , where  $\gamma = 1$  in the classical regime and crosses over to  $\gamma = 2$  at  $T_C = 0$  K. Figure 2 is a plot of  $\log$  of  $1/(\epsilon' - \epsilon'_\infty)$  vs.  $\log (T - T_C)$  where  $T_C = 0$  for the 9.2-kbar data. The results show the predicted behavior. At 1 bar and 8.3 kbar  $T_C$  is sufficiently far away from the quantum displacive limit ( $T_C = 0$  K) so that  $\gamma \simeq 1.0$ ; however, 9.2 kbar is very close to this limit, and we see the emergence of a distinct  $\gamma = 2.0$  regime in the response, as predicted.

Another consequence of the complete suppression of  $T_C$  is the formation of a quantum paraelectric state characterized by a high dielectric susceptibility (or low soft-mode frequency) which is constant at low  $T$  over an extended  $T$  range. Such a state is evident in Figs. 1 and 2. Because the characteristic energies are small in the quantum regime, *dc* biasing fields can be expected to strongly suppress the  $\epsilon'(T)$  response. The results in Fig. 3 show the large suppression of  $\epsilon'$  by a very modest field (0.85 kV/cm) confirming theoretical predictions.

**Significance**—Pressure has been shown to be an excellent variable for studying the manifestation of quantum fluctuations in FE properties. By the application of pressure to a sample of fixed composition one varies only the balance between long- and short-range forces, thereby avoiding the above-mentioned complications associated with chemical substitution and leading to a better understanding of physics.

**Sponsors for various phases of this work include:** BES

**Contact:** George A. Samara, Nanostructures and Device Sciences, Department 1120

Phone: (505) 844-6653, Fax: (505) 844-4045, E-mail: gasamar@sandia.gov

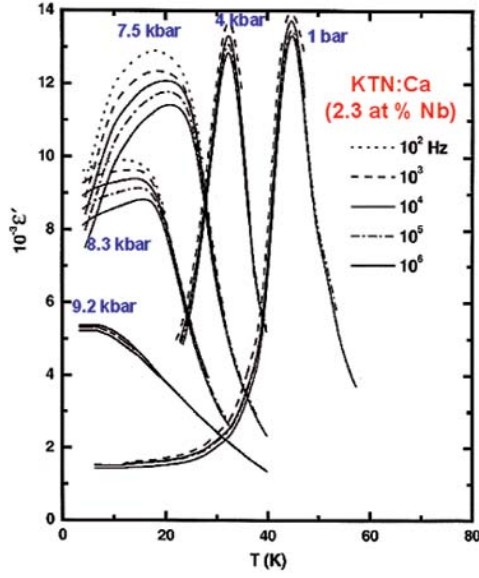


**Figure 2.** Analysis of  $\epsilon'(T)$  data for KTN ( $x = 0.23$ ):Ca at different pressures showing the emergence of the critical exponent  $\gamma = 2.0$  at the quantum displacive limit ( $p_c = 9.2$  kbar,  $T_c = 0$  K).

**Figure 1.** Temperature dependence of the dielectric constant of KTN ( $x = 0.023$ ):Ca showing the pressure induced FE-to-R crossover and the vanishing of the transition of 9.2 kbar.

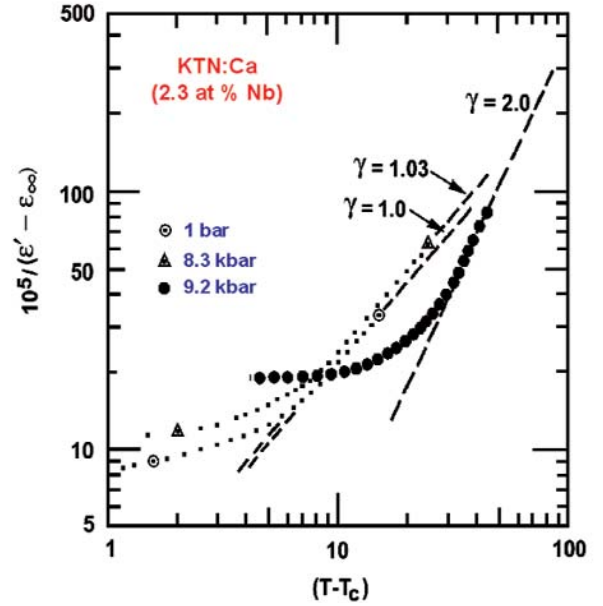
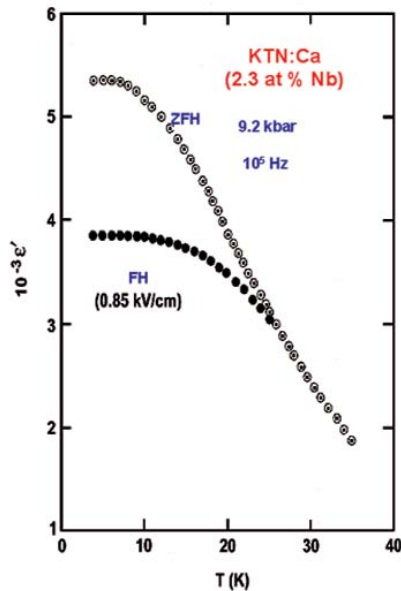


**Figure 3.** Influence of a bias electric field on  $\epsilon'(T)$  of KTN:Ca at 9.2 kbar in the quantum paraelectric regime. (ZFH = zero bias field heating and FH = field heating).



## Dynamics of Polar Nanodomains in Relaxor Ferroelectrics

by *E. L. Venturini and G. A. Samara*

**Motivation**—The mixed oxide perovskite  $\text{Pb}(\text{Zn}_{1/3}\text{Nb}_{2/3})\text{O}_3$  (PZN) exhibits large dielectric constants and electromechanical coupling that offer enhanced performance in applications such as multilayer capacitors and electro-mechanical actuators. This material has a diffuse phase transition from a high-temperature, paraelectric phase to a relaxor ferroelectric phase near 410 K. The attractive dielectric properties in the relaxor phase arise from dynamic, polar nanodomains in a mechanically soft, easily polarized host lattice. The detailed physics of these nanodomains remains controversial, and we have employed ac dielectric measurements under hydrostatic pressure to delineate the domain dynamics.

**Accomplishment**—The host lattice can be further softened by adding a small amount of  $\text{PbTiO}_3$  (PT), thus forming a PZN/PT mixed crystal that lies near a morphotropic (structural) phase boundary; we have studied a PZN/PT 90/10 single crystal. The data in Fig. 1 compare the dielectric constant  $\epsilon'$  versus decreasing temperature at pressures of 1 atm and 10 kbar for frequencies of 1, 10 and 100 kHz. At ambient pressure the temperature  $T_{\text{max}}$  where  $\epsilon'$  reaches a maximum is independent of frequency between 1 and 100 kHz and the data show no discernable dispersion below the maximum. These features are characteristic of a normal ferroelectric where the polar domains reach macroscopic size and become static below the maximum in  $\epsilon'$ . In contrast, the  $\epsilon'$  data at 10 kbar show pronounced dispersion at and below  $T_{\text{max}}$ , characteristic of a relaxor ferroelectric with dynamic polar nanodomains. The application of hydrostatic pressure decreases the

polarizability (softness) of the host lattice and thus limits the growth of the polar domains.

The dynamics of these nanodomains can be established from the dispersion in  $\epsilon'$ : the average nanodomain fluctuation frequency matches the measurement frequency at  $T_{\text{max}}$ . Figure 2 shows the dispersion in  $T_{\text{max}}$  between 100 Hz and 1 MHz at 5, 10 and 15 kbar (relaxor behavior) and the absence of dispersion at ambient pressure (normal ferroelectric). The greater dispersion at higher pressure (Fig. 2) reflects increasing relaxor behavior. The nanodomain dynamics can be modeled by a Vogel-Fulcher equation  $f = f_0 \exp\{-E_a/k_B(T_{\text{max}} - T_0)\}$  where  $f$  is the measurement frequency,  $f_0$  is a fluctuation "attempt" frequency (fixed at 1 THz for this analysis),  $E_a$  is an effective energy barrier for fluctuations,  $k_B$  is the Boltzmann constant and  $T_0$  is the temperature where all relaxation times diverge. Adjusting  $E_a$  and  $T_0$  results in the solid-line fits shown in Fig. 2. There is a nearly linear increase in  $E_a$  and decrease in  $T_0$  with increasing pressure as shown in Fig. 3.

**Significance**—The pronounced change in the dynamics of polar nanodomains under pressure in a PZN/PT relaxor ferroelectric provides new insight into the physics of this important technological material. The energy barrier  $E_a$  for nanodomain fluctuations increases linearly with increasing pressure as the host lattice stiffens. At ambient pressure the long-range electrostatic forces support polar domain growth to macroscopic size and a static ferroelectric phase. Under hydrostatic pressure, these forces are reduced and there is a crossover to a dynamic, polar nanodomain state with relaxor behavior.

**Sponsors for various phases of this work include:** BES, Nuclear Weapons/Science and Technology

**Contact:** Eugene L. Venturini, Nanostructures and Advanced Materials Chemistry, Department 1122

Phone: (505) 844-7055, Fax: (505) 844-4045, E-mail: elventu@sandia.gov

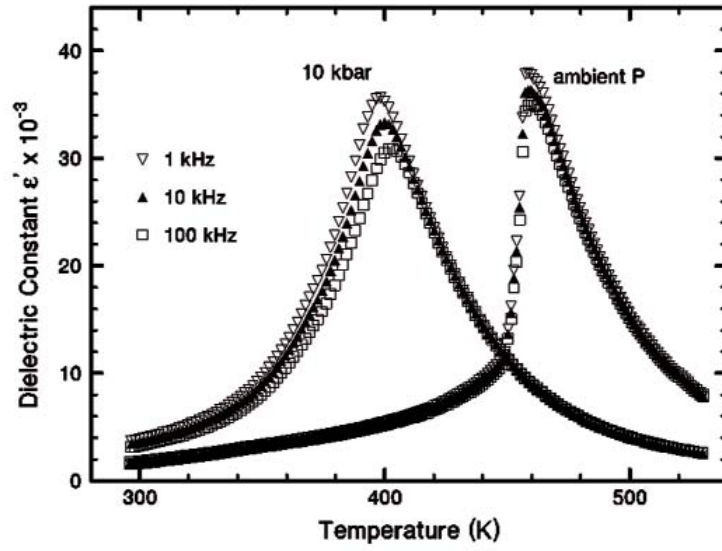


**Figure 1.** Ferroelectric (ambient P) and relaxor (10 kbar) transitions in PZN/PT 90/10 crystal.

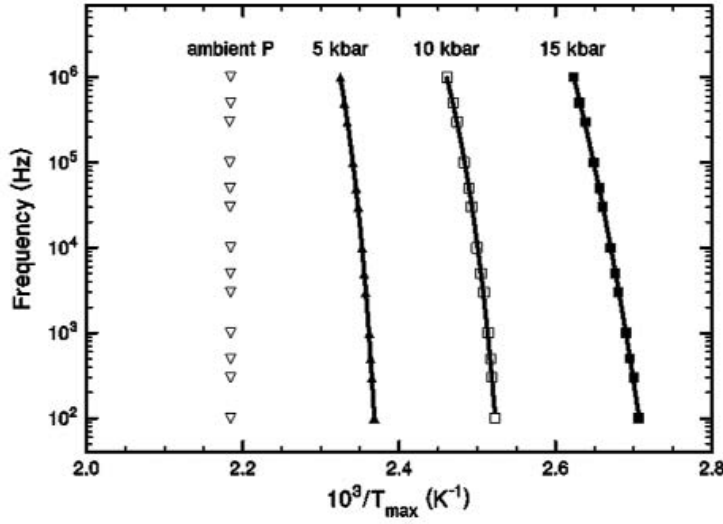


**Figure 2.** Frequency dispersion of  $T_{\max}$  and Vogel-Fulcher fits at 5, 10 and 15 kbar.

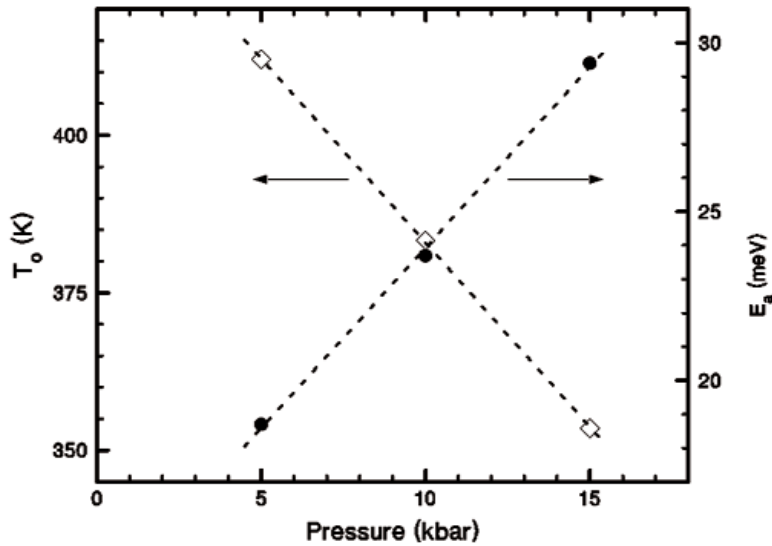


**Figure 3.** Pressure dependence of Vogel-Fulcher temperature  $T_0$  and energy barrier  $E_a$ .

## PZT 95/5 Phase Diagram from First Principles and Effective Hamiltonian

by *K. Leung, E. Cockayne, and A. F. Wright*

**Motivation**—Lead Zirconate-Titanate (PZT) 95/5, with 2% Nb, is ferroelectric at low temperature ( $F_{R(LT)}$ ), and it contains bound charges on crystal surfaces. Due to the system's proximity to the antiferroelectric ( $A_O$ )-ferroelectric phase boundary, applying pressure (e.g., shock waves) induces a transition to the  $A_O$  phase and releases the captive surface charges, yielding a transient current. As a result, this material is used as a compact power supply in high-voltage, pulsed-current applications. Considerable effort is being applied to simulate its shock wave response at the grain scale. The material properties, required as input for such simulations, are largely unavailable from experiments due to the lack of large single crystal samples. Therefore accurate first principles predictions are crucial for modeling the properties of this material as well as for understanding the underlying physics of the phase transitions.

**Accomplishment**—The PZT 95/5 (0% Nb) phase diagram is complex. We have used extensive first principles calculations to study the energy landscapes associated with the following stable/metastable structures: the paraelectric phase ( $P_C$ ), two ferroelectric phases  $F_{R(LT)}$  and  $F_{R(HT)}$ , distinguished by the presence/absence of oxygen octahedral tilts, and the antiferroelectric phase  $A_O$ , which is the ground state in the absence of Nb (Fig. 1). We find that (a) the  $F_{R(HT)}$  structure, seen in experiments, is unstable at zero temperature and is energetically unfavorable; (b) the metastable  $F_{R(LT)}$  structure, not seen in experiments, is very close in energy to the stable  $A_O$  phase. This is reasonable because it is known experimentally that increasing the Ti content slightly at low temperature is sufficient to make  $F_{R(LT)}$  the stable phase. Our

novel prediction is that this same  $A_O$ - $F_{R(LT)}$  competition is also responsible for the temperature driven antiferroelectric-ferroelectric phase transition in PZT 95/5.

To extend these results to finite temperature, we have constructed an effective Hamiltonian which captures the main physics of the PZT 95/5 phase diagram. Our model uses parameters that are primarily fitted to first principles predictions at  $T = 0$  K. Novel features of this Hamiltonian include: (a) a lattice expansion term, which is the driving force of the antiferroelectric-ferroelectric phase transition; (b) non-local anharmonic couplings between oxygen octahedral tilts in neighboring primitive cells; and (c) direct incorporation of metastable structure energies. Finite temperature Monte Carlo simulation of the effective Hamiltonian yields successively the  $A_O$ ,  $F_{R(HT)}$ , and  $P_C$  phases as temperature increases, in qualitative agreement with experiments. This is shown in Fig. 2 which is a plot of the order parameters that indicate stability of the different phases. The structures and crystal symmetries of the phases are also in agreement. The  $F_{R(HT)}$  order parameter is proportional to the spontaneous polarization of the crystal and indicates this phase's ability to store charge.

**Significance**—This is the first work which succeeds in reproducing the main signatures of the complex PZT 95/5 zero temperature structure and the succession of temperature-driven phase transitions. It paves the way to investigating Nb-doped samples as well as the pressure dependence of material properties at finite temperature.

**Sponsors for various phases of this work include:** ASCI, Nuclear Weapons/Science and Technology

**Contact:** Kevin Leung, Nanostructure and Semiconductor Physics, Department 1112

Phone: (505) 844-1588, Fax: (505) 844-1197, E-mail: kleung@sandia.gov



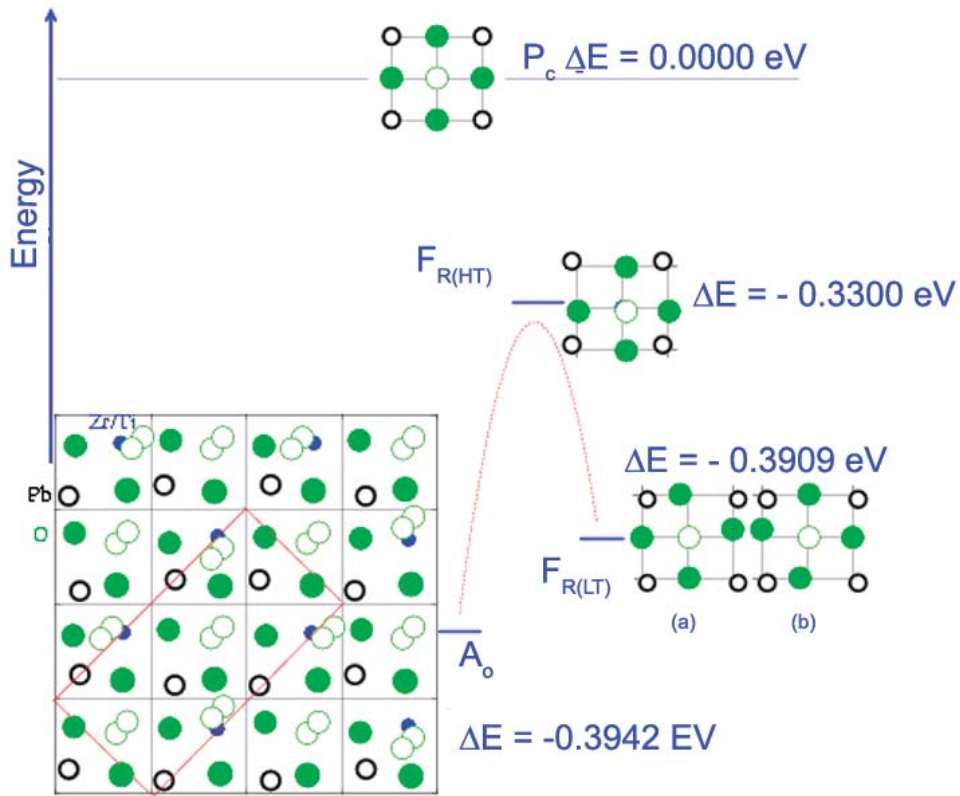


**Figure 1.** Structure and formation energies of antiferroelectric ( $A_O$ , 40-atom unit cell), high-temperature ferroelectric  $F_{R(HT)}$  (5-atom cell), and low-temperature ferroelectric  $F_{R(LT)}$  (10-atom cell) phases relative to the paraelectric cubic phase ( $P_C$ , 5-atom cell).  $F_{R(HT)}$  is unstable relative to the  $A_O$  and  $F_{R(LT)}$  phases which have similar energies. The oxygen octahedral tilt in  $F_{R(LT)}$  is illustrated with the depiction of two successive crystal planes denoted (a) and (b).

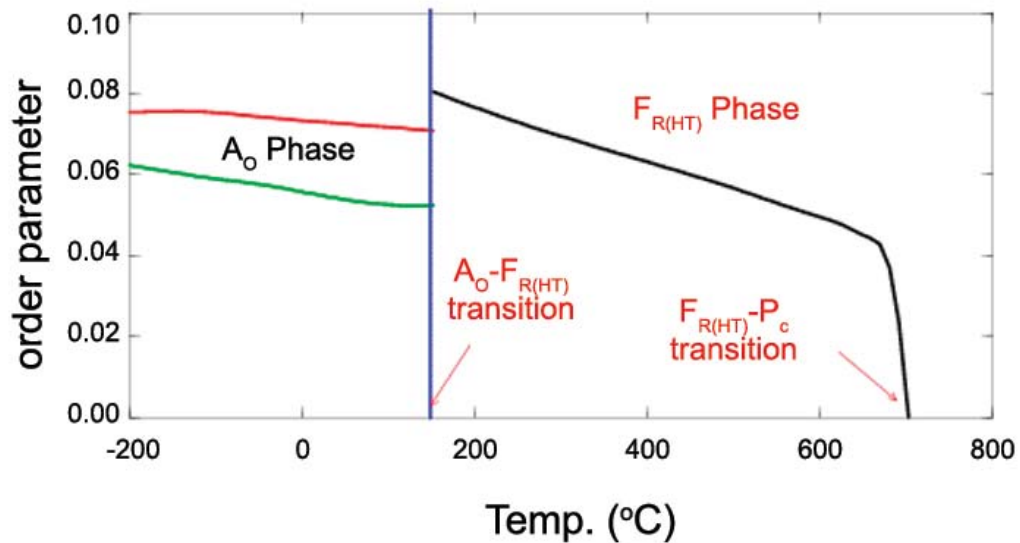


**Figure 2.** The order parameters (arbitrary units) indicate which phases are stable as a function of temperature. The  $A_O$  phase exhibits two modes (shown as red and green); the onset of the ferroelectric mode (black) signals the transition to the  $F_{R(HT)}$  phase.



## Strong Porosity Effects in the Shock Response of PZT 95/5

by R. E. Setchell, B. A. Tuttle, and J. A. Voigt

**Motivation**—High voltages are generated in pulsed power devices through the shock-induced depoling of the ferroelectric ceramic PZT 95/5. Future production of such devices will use PZT 95/5 materials made at Sandia through a new "chem prep" process still under development. A variable in PZT 95/5 production with important consequences for performance and reliability is the material porosity. Previous studies with materials made using a mixed-oxide process showed that a fairly narrow range in bulk density was required to achieve good performance while minimizing the probability for high-voltage breakdown. This density range is obtained by adding organic pore formers to powders prior to pressing, bisque firing, and sintering. A critical current issue is the optimum type and quantity of pore former to be used in chem prep PZT 95/5.

**Accomplishment**—An experimental program is carefully examining the effects of porosity in chem prep PZT 95/5. The goal of this program is to gain fundamental insights into how the porous microstructure affects the mechanical and electrical behavior of normally poled material during shock propagation. A previous study extensively examined mixed-oxide material made with approximately 1.0% by weight spherical Lucite pore formers (50-100  $\mu\text{m}$  diameters), resulting in a fixed density of 7.30  $\text{g}/\text{cm}^3$  (9% porosity). To date the new study has examined chem prep materials made with Avicel pore formers (rods 5-15  $\mu\text{m}$  in diameter and  $\geq 20$   $\mu\text{m}$  long), with additions by weight ranging from 0.45% to 4.0%. The corresponding range in densities is from 7.65  $\text{g}/\text{cm}^3$  (4% porosity) to 6.98  $\text{g}/\text{cm}^3$  (13% porosity). A variety of planar-impact configurations have been used in experiments conducted on the Department 1122

gas gun facility to establish shock response characteristics of these materials. Figure 1 compares Hugoniot states in three chem prep materials with the Hugoniot curve established for the 7.30  $\text{g}/\text{cm}^3$  mixed-oxide material. The high density and low density cases appear to have Hugoniot curves that deviate rapidly from the reference curve at shock pressures above 2.5 GPa. Figure 2 shows VISAR-measured waveforms after fairly strong ( $\geq 4$  GPa) shock waves had propagated through samples 4.0-mm thick. A distinct plateau can be seen in each waveform, with the plateau level decreasing by a factor of two from the high-density case to the low-density case. The plateaus correspond to the onset of dynamic yielding associated with the collapse of the porosity introduced through pore formers. These levels are plotted as a function of density in Fig. 3, together with a value determined in an early study of mixed-oxide material prepared without pore formers. Figure 4 shows the charge release per unit area from normally poled samples during shock transit. The insert shows that the total charge release does not decrease linearly with increasing porosity, as might be expected.

**Significance**—Our experiments are quantifying the sensitivity of the shock response of PZT 95/5 to changes in the porous microstructure. Large differences in mechanical and electrical behavior have been observed over a  $\pm 5\%$  variation in bulk density. These differences are significant both for performance requirements and for high-voltage breakdown concerns. To progress towards identifying an optimum porous microstructure for PZT 95/5, continuing studies will carefully consider differences in pore morphology as well as bulk density.

**Sponsors for various phases of this work include:** LDRD, Nuclear Weapons/Science and Technology

**Contact:** Robert E. Setchell, Nanostructures and Advanced Materials Chemistry, Department 1122

Phone: (505) 844-3847, Fax: (505) 844-4045, E-mail: resetch@sandia.gov

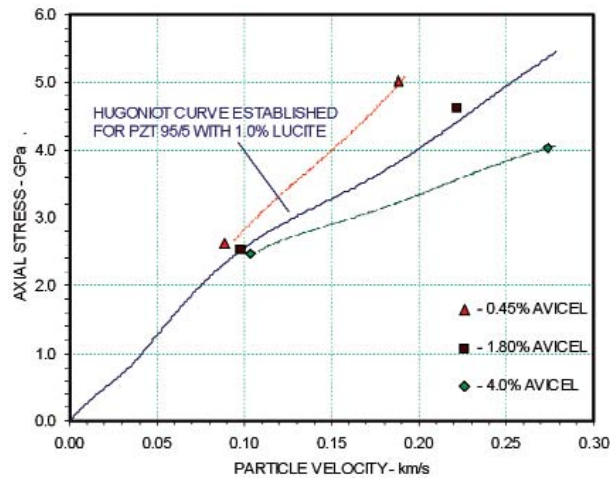


**Figure 1.** Hugoniot states determined from reverse-impact experiments. The central curve was previously established for a mixed-oxide PZT made with 1.0 weight percent Lucite pore former. This material has the same density as the 1.8% Avicel (chem prep) case.

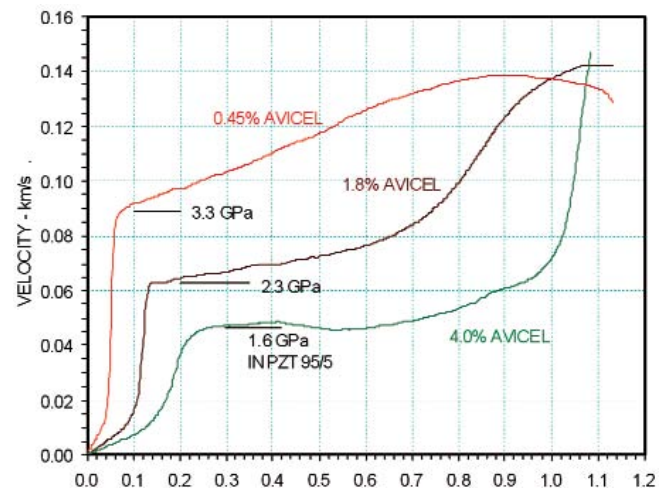


**Figure 2.** Observed waveforms after 4 GPa shock waves had propagated through 4.0 mm, unpoled samples at different densities. Thresholds for the onset of dynamic yielding are indicated.

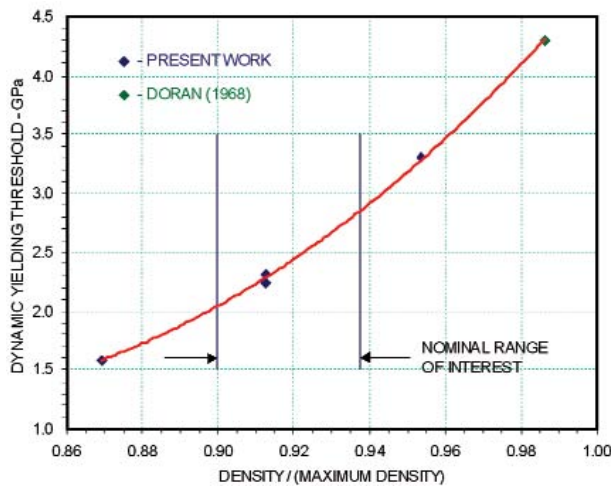


**Figure 3.** Threshold pressures for dynamic yielding associated with the collapse of material porosity resulting from pore former addition.

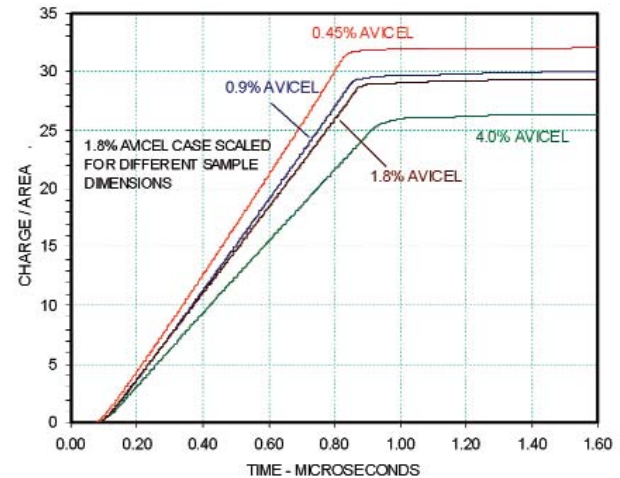


**Figure 4.** Total charge per unit area released during transit of 2.5 GPa shocks. A faster-than-linear decrease with increasing porosity is observed.

# Lasers and Optical Materials



## Improving the Beam Quality of Nanosecond Optical Parametric Oscillators

*by Arlee Smith and Darrell Armstrong*

**Motivation**—The poor beam quality typical of high-pulse-energy optical parametric oscillators (OPOs) limits their range of applications. However, in certain types of OPOs the beam quality is good in one transverse dimension. If similar beam quality can be achieved in the other dimension the beam quality of OPOs will rival that of the best nanosecond lasers.

**Accomplishment**—Most laser applications specify a wavelength. Because there are only a few reliable, well developed lasers such as Nd:YAG, it is often necessary to shift the wavelength of the laser light using nonlinear optical techniques such as Raman shifting, frequency doubling, or optical parametric amplification. Only the latter can provide broad band tuning with high conversion efficiency. It uses a nonlinear optical crystal such as KDP to split a laser photon into two longer wavelength photons with the same total energy. Parametric amplification provides exponential gain much like a laser medium, so oscillation can occur if mirrors are placed on each end of the crystal to provide feedback. If the laser pulse duration is a few nanoseconds, as is typical of Q-switched lasers, the oscillator cavity must be short — typically a few cm — due to constraints imposed by crystal and mirror optical damage. This damage restricts the laser irradiance which in turn limits the parametric gain for a single pass of the cavity. Many passes are required, hence the short cavity. Consequently, if high pulse energy is desired, the beam diameters must be scaled up. This combination of a short cavity and large beam diameter is the recipe for poor beam quality. In spite of this, OPOs with birefringent walk off, or different directions of energy flow for the two generated photons, have good beam quality in the direction of walk off.

Over the past few years we have succeeded in

simulating in detail the performance of these OPOs including the beam quality. We developed a good physical understanding of the factors that determine beam quality, and proposed a new cavity design that could give good beam quality in both dimensions. Our simulations predicted excellent performance with the cavity shown in Fig. 1. This cavity rotates the image of the reflected beam by 90° on each cavity pass. Birefringent walkoff tends to induce phase and irradiance correlations across the beam in the direction of walk off but not in the other direction. By rotating the image on each pass these correlations can be extended to both dimensions. These two-dimensional correlations provide good beam quality in both dimensions across the face of the beam. Figure 2 compares the beam from an OPO with good beam quality in only one dimension with that from the rotated-image OPO.

The cavity in Fig. 1 is rather long, so its conversion efficiency is somewhat lower than a typical nanosecond OPO. We are designing and testing shorter image-rotating cavities to restore the conversion efficiency. Because of the peculiar properties of image-rotating cavities it should be possible to build these in monolithic structures without fine mirror adjustments. This would make these designs doubly attractive in harsh environments with high vibration or dust contamination.

**Significance**—Beam quality is essentially a measure of how well a beam can focus. Good focusing properties are critical in many applications such as compact sensors, remote sensing, or IR counter measures. It is also critical for efficient wavelength conversion in further nonlinear optical stages. We anticipate that our new designs will become a standard for future OPOs.

---

**Sponsors for various phases of this work include:** Nuclear Weapons/Science and Technology

**Contact:** Arlee V. Smith; Lasers, Optics and Remote Sensing, Department 1118

Phone: (505) 844-5810, Fax: (505) 844-5459, E-mail: arlsmit@sandia.gov

---

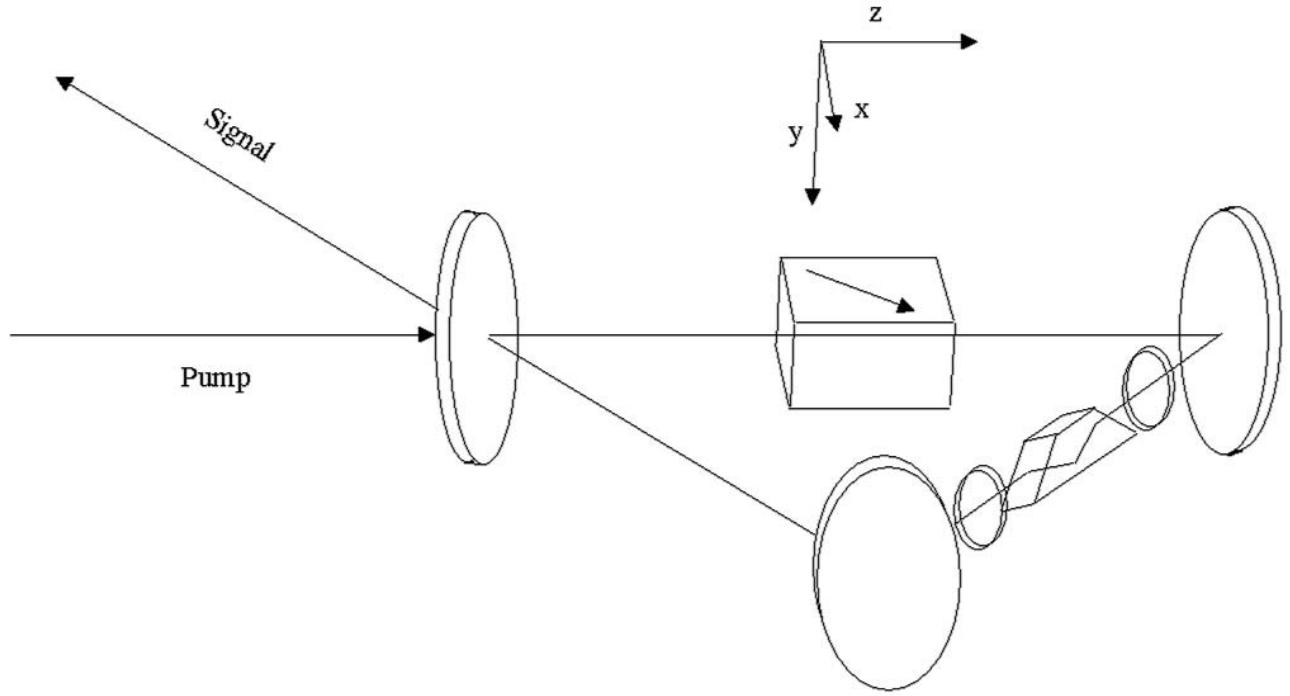


**Figure 1.** An image-rotating optical parametric oscillator design. The combination of a dove prism and three-mirror ring gives a  $90^\circ$  image rotation on each cavity pass.

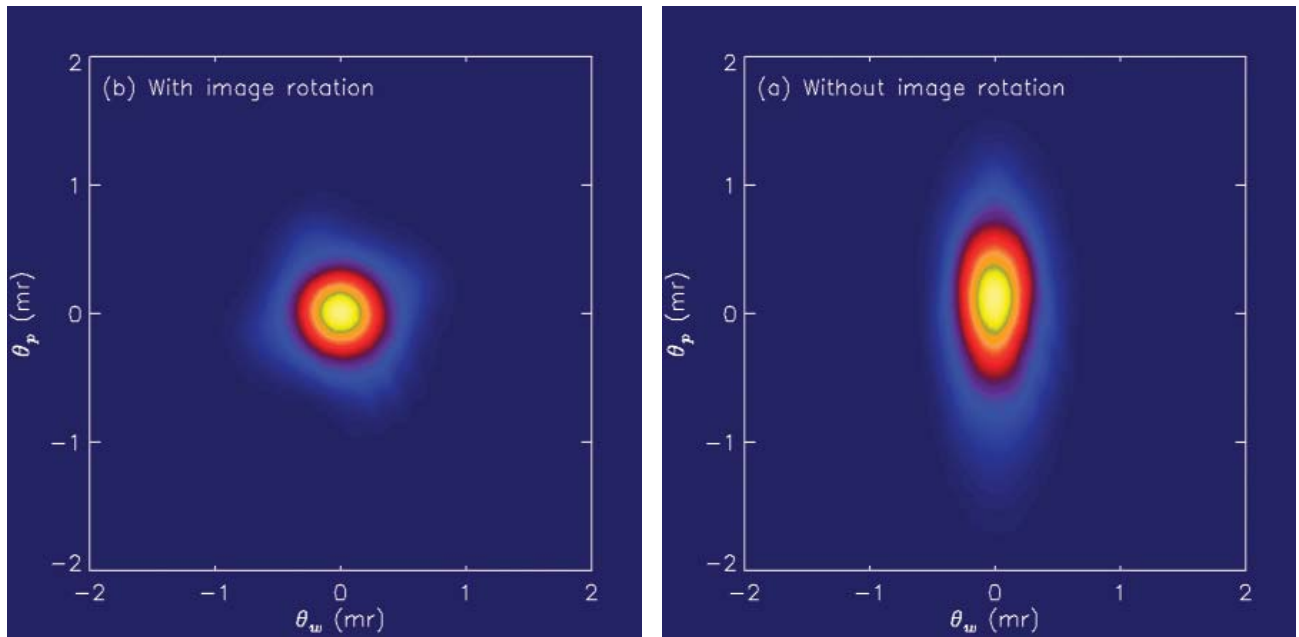


**Figure 2.** A comparison of far-field fluence profiles for the three-mirror ring cavity of Fig. 1 without (a) and with (b) the dove prism in place. Without the dove prism there is no image rotation, only an image inversion.



## Photoluminescent Investigation of the Defect Structure of Doped and Undoped Lithium Niobate

by *W. J. Thomes, Jr., K. Simmons-Potter and B. G. Potter, Jr.*

**Motivation**—Optical materials generally exhibit a large induced loss in infra-red light transmission when exposed to high-flux transient or low-level continuous-wave ionizing radiation doses. We have found, however, that Mg-doped LiNbO<sub>3</sub> exhibits good resistance to radiation-induced optical degradation. A basic understanding of the mechanisms responsible for this improved radiation resistance is needed so that these materials can be reliably incorporated into future device applications.

**Accomplishment**—Photoluminescence (PL) measurements were conducted on cryogenically cooled samples of LiNbO<sub>3</sub> with varying degrees of Mg doping. It was observed that the crystals with higher concentrations of Mg exhibited a larger PL response through an increase in the emission intensity and narrowing of the spectral distribution in the 400 to 600 nm range. Figure 1 shows representative steady-state PL spectra from highly-doped and low-dopant-level LiNbO<sub>3</sub>. (Note that the low-dopant-level spectrum has been multiplied by a factor of eight for the comparison.) Fitting the spectra with a triple Gaussian function revealed that all of the spectra are composed of the same three peaks around 436 nm, 484 nm, and 500 nm. The differences in the shapes of the two spectra arise from changes in the relative ratios between the three peaks. The dominant band change is seen in the intensity of the 436 nm peak, which increases dramatically as more Mg is added to the LiNbO<sub>3</sub> lattice. Accompanying these changes, the lifetime of the 440 nm and 485 nm (maxima of the

steady-state spectra) luminescence also increases with Mg doping. Figure 2 shows representative time-resolved PL measurements from the low-dopant-level and highly-doped samples. The luminescence decays more slowly in the samples with higher Mg doping. This shift in decay rate is a result of a redistribution of the defect energy states in the LiNbO<sub>3</sub> crystal through changes in the Nb local crystal symmetry and the electron-phonon coupling caused by the introduction of Mg into the structure. We are presently working on relating these changes to the improvement in the radiation resistance of these crystals.

**Significance**—Optical systems offer many advantages over more conventional electrical systems for many DOE/DP applications. In a variety of device environments, however, such as space-based ultrafast communications and weapons applications, these systems need to be able to withstand large doses of ionizing radiation without suffering a loss in performance or function. Correlations developed from our PL and radiation-exposure studies will allow prediction of the optical response of doped and undoped LiNbO<sub>3</sub> in ionizing radiation fields. The possibility therefore exists to use optical spectroscopy as a materials evaluation method to avoid direct radiation testing of materials and systems. Changes in the local crystal symmetry and the electron-phonon coupling elucidated through the PL investigations provide insight into the necessary requirements needed to produce radiation "hard" optical systems.

---

**Sponsors for various phases of this work include:** Nuclear Weapons/Science and Technology

**Contact:** Joe Thomes; Lasers, Optics, Remote Sensing and Plasma Sciences, Department 1118

Phone: (505) 284-5342, Fax: (505) 844-5459, E-mail: [wjthome@sandia.gov](mailto:wjthome@sandia.gov)

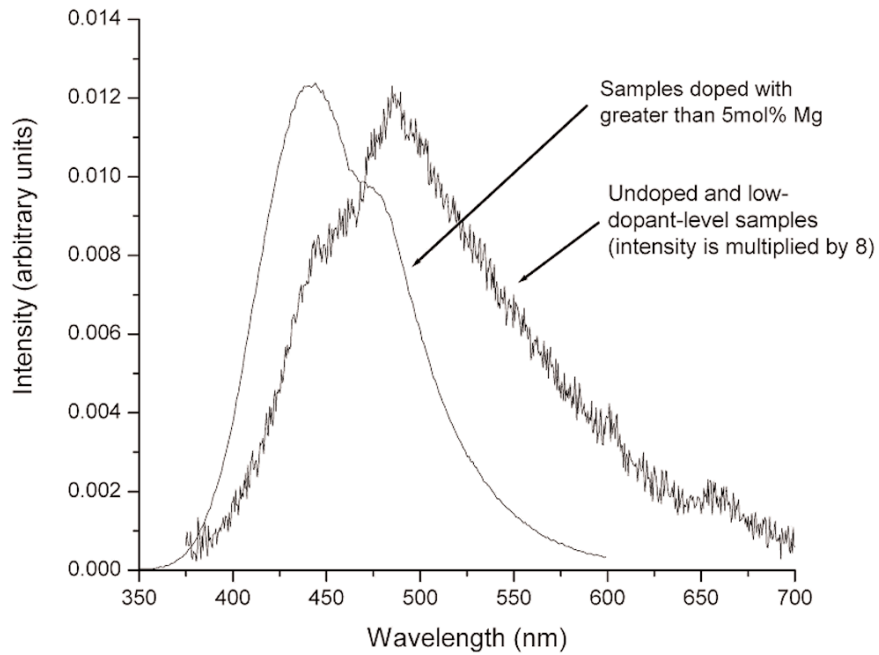


**Figure 1.** Representative steady-state photoluminescent spectra from highly-doped and low-dopant-level  $\text{LiNbO}_3$ . Samples were cooled to 16 K during measurement.

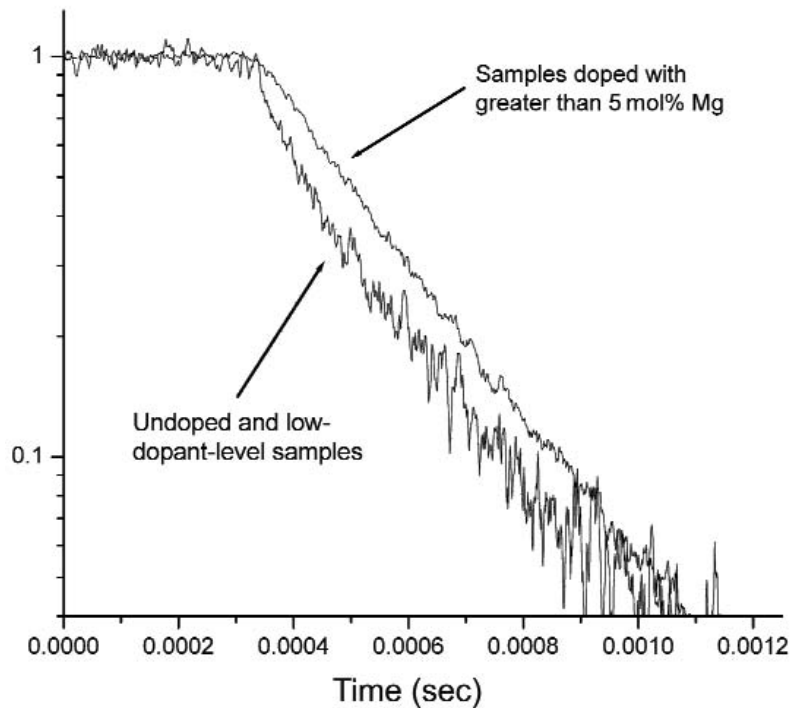


**Figure 2.** Representative time-resolved photoluminescent spectra from highly-doped and low-dopant-level  $\text{LiNbO}_3$  taken at 440 nm. Spectra taken at 485 nm were similar. All samples were cooled to 16 K during measurement. Crystals with a higher Mg dopant concentration are seen to decay more slowly compared to those with less Mg incorporated.

# Semiconductor Materials and Physics



## Theory of Exciton Transfer between Semiconductor Quantum Wells

by *S. K. Lyo*

**Motivation**—Exciton transfer between deep quantum wells (QWs) and quantum dots separated by wide barriers is not only an academically interesting phenomenon but plays a fundamental role in optoelectronic devices based on artificially structured semiconductors such as QW lasers and light-emitting diodes. Recent data from photoluminescence excitation and photoluminescence studies indicate that excitons migrate with surprisingly fast rates between distant QWs separated by tens of nm. The observed transfer rates are too fast to be explained by carrier tunneling through the barriers or by thermal activation. There has been no satisfactory understanding of this important phenomenon.

**Accomplishment**—The QWs studied have well depths much larger than the thermal energy and have different QW widths resulting in an energy mismatch much larger than the exciton binding energy ( $\sim$  tens of meV). We found that different mechanisms are responsible for the Stokes exciton transfer (i.e., from the higher-energy to the lower-energy QW) and the anti-Stokes back transfer. For Stokes transfer, an exciton in the initial QW decays into a free electron-hole (e-h) pair in the final QW, relaxing the extra energy into e-h kinetic energies, while the in-plane momentum of the center of mass is conserved. The e-h pair is then recombined instantly (i.e., in a time scale much shorter than the transfer time) into an exciton in the final QW. The coupling between the initial and final states is dominated by electric dipole-dipole interaction at a short distance and by photon-exchange interaction at a long distance beyond

$\sim 10$  nm in GaAs/ $\text{Al}_x\text{Ga}_{1-x}\text{As}$  QWs. The dipolar rate decays with the distance  $d$  as  $1/d^4$  while the photon-exchange rate decays slowly (e.g., logarithmically). For the latter, a resonant or virtual photon is emitted through the e-h recombination in the initial exciton and reabsorbed in the final QW by promoting a valence electron into the conduction band.

We found that the anti-Stokes transfer occurs through two-exciton Auger processes, where an exciton is annihilated nonradiatively by monopole-dipole interaction, imparting the energy to ionize another exciton into an e-h pair over the barrier. These e-h pairs fall into the higher-energy QW and form excitons instantly.

We have also found that localization of the excitons affects the transfer rate as well as its temperature dependence significantly. The phonon-assisted processes are from higher-order processes and yield negligible transfer rates for both Stokes and anti-Stokes transfer.

**Significance**—Our theory yields good agreement with observed data. This is significant in view of the fact that no other microscopic mechanisms proposed so far yield even the correct order of magnitude agreement with the data for the exciton transfer over a long distance. The predicted Stokes (anti-Stokes) rate is more sensitive to the interface roughness of the QWs (exciton density) than to the distance between the QWs, explaining recent *intriguing* data which show faster rates for QWs separated by a greater distance in some samples as evident in the following figures.

---

**Sponsors for various phases of this work include:** BES, LDRD

**Contact:** S. Ken Lyo, Semiconductor Materials and Device Sciences, Department 1123

Phone: (505) 844-3718, Fax: (505) 844-1197, E-mail: sklyo@sandia.gov

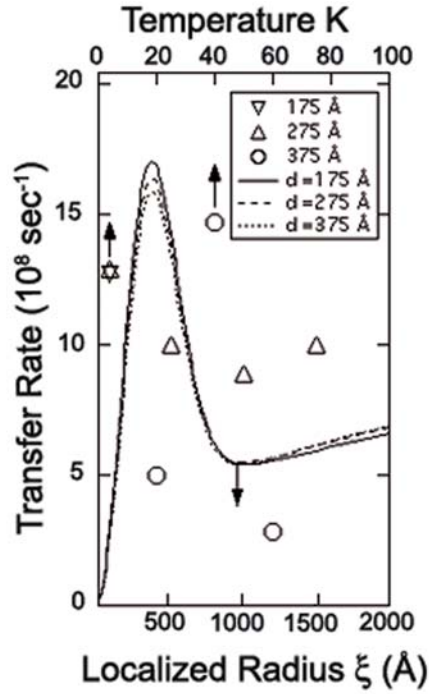


**Figure 1.** Calculated Stokes exciton transfer rate from a narrow (5 nm) to a wide (10 nm) QW in GaAs/Al<sub>0.3</sub>Ga<sub>0.7</sub>As double QWs as a function of the exciton localization radius. The rate is independent of the temperature.  $d$  is the center-to-center distance between the QWs. The symbols are the temperature-dependent data (upper axis) from A. Tomita, J. Shah, and R. S. Knox, Phys. Rev. B, 53, 10793 (1996).

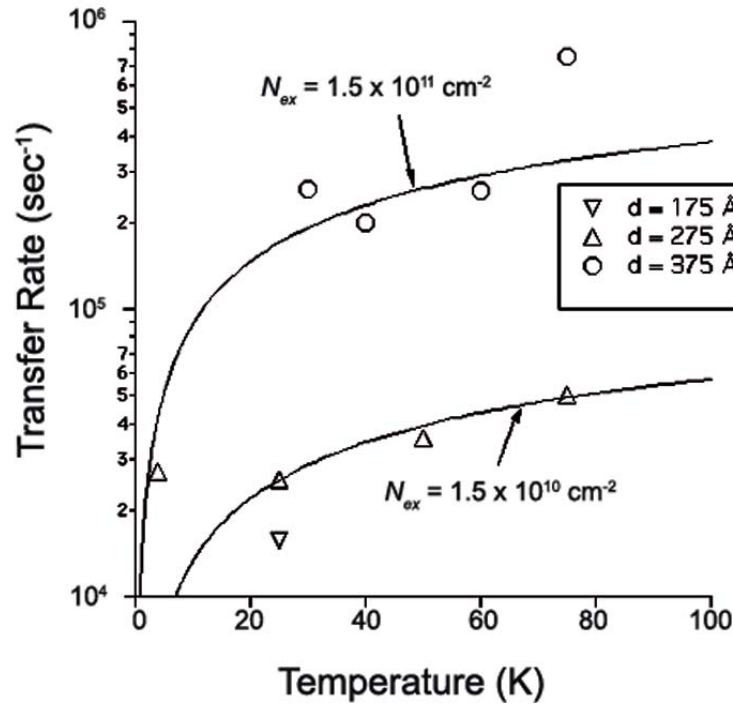


**Figure 2.** Calculated anti-Stokes exciton transfer rate from a wide (10 nm) to a narrow (5 nm) QW in GaAs/Al<sub>0.3</sub>Ga<sub>0.7</sub>As double QWs as a function of the temperature. The symbols are from A. Tomita, J. Shah, and R. S. Knox, Phys. Rev. B, 53, 10793 (1996). The adjustable parameter  $N_{ex}$  is the exciton density and  $d$  is the center-to-center distance between the QWs.



## Anomalous Temperature Dependent Exciton Energies in AlGaAs Alloys

by *E. D. Jones, S. K. Lyo, and J. L. Reno*

**Motivation**—Semiconductor alloys play an integral and important role in the design and operation of modern optoelectronic materials. A fundamental understanding of the random nature of alloys would provide the optoelectronic industry with the necessary tools for producing high mobility (high quality) devices. However, the tools necessary for characterizing the random nature of semiconductor alloys are still in their infancy. The photoluminescence measurement of the line shape at low temperatures provides the best data that can be interpreted in terms of a random alloy model.

**Accomplishment**—We have discovered that the temperature dependencies of the exciton energies in many semiconductor alloys do not exhibit the expected behavior based on simple temperature dependent thermal expansion of the lattice constant. We attribute this anomalous behavior to the presence of random alloy fluctuations. In the past, these anomalies were blamed on various phenomena involving dislocations, interstitial impurities, etc. To date, we have observed this kind of anomalous temperature dependence for several semiconductor alloys such as AlGaAs, InGaP, InGaAs, and InGaAsP. For purposes of this report, only the AlGaAs data will be discussed. The photoluminescence spectrum at 1.4K for an  $\text{Al}_{0.20}\text{Ga}_{0.80}\text{As}$  alloy is shown in Fig. 1. The line shape is almost

Gaussian and the full-width-half-maximum (FWHM) linewidth of about 2.9 meV is nearly theoretical thereby indicating no strong evidence for clustering, etc. Traditionally, the line-shape, linewidth measurement marks the end of the analyses for non-random alloy fluctuations.

Because the non-random contributions to the alloy fluctuation spectrum for our samples are minimal, other experimental methods for detection have to be employed. Figure 2 shows the result of measuring the band gap energy versus temperature between 1.4 and 120 K. The open circles are the data points and the solid line is the behavior expected from a simple temperature dependent lattice constant model. The difference in energy at low temperatures is a result of random alloy fluctuations of the band gap energy. Efforts are underway to extract the alloy fluctuation energy spectrum by modeling the difference between the thermal expansion model (solid line) and the experimental data (open circles).

**Significance**—Information about the non-random character of the alloy fluctuation energy spectrum can be made from temperature dependent photoluminescence measurements. This kind of information is valuable in order to produce high mobility and hence high quality optoelectronic devices.

---

**Sponsors for various phases of this work include:** BES, LDRD

**Contact:** Eric D. Jones, Semiconductor Material and Device Sciences, Department 1123

Phone: (505) 844-8752, Fax: (505) 844-3211, E-mail: [edjones@sandia.gov](mailto:edjones@sandia.gov)

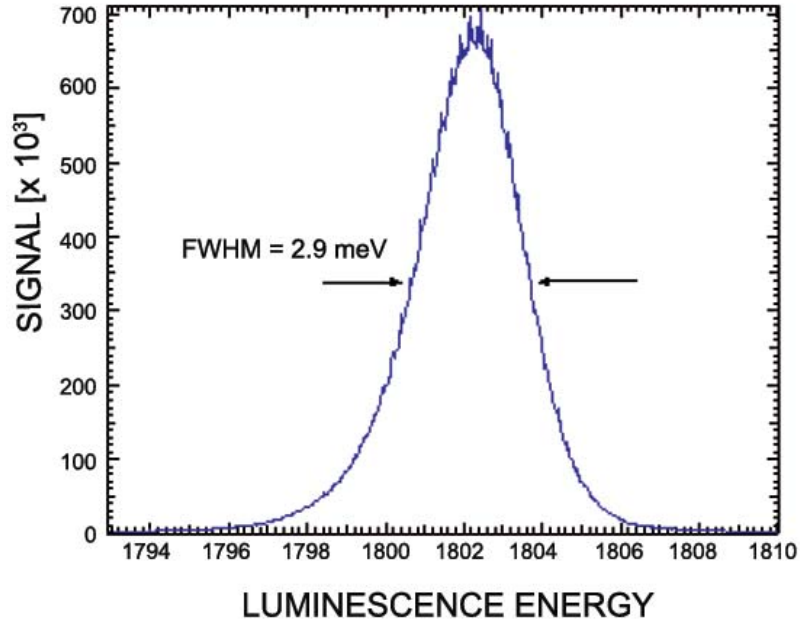


**Figure 1.** Photoluminescence spectrum for an  $\text{Al}_{0.20}\text{Ga}_{0.80}\text{As}$  alloy at  $T=1.4\text{K}$ . The FWHM linewidth of about 2.9 meV is nearly theoretical.

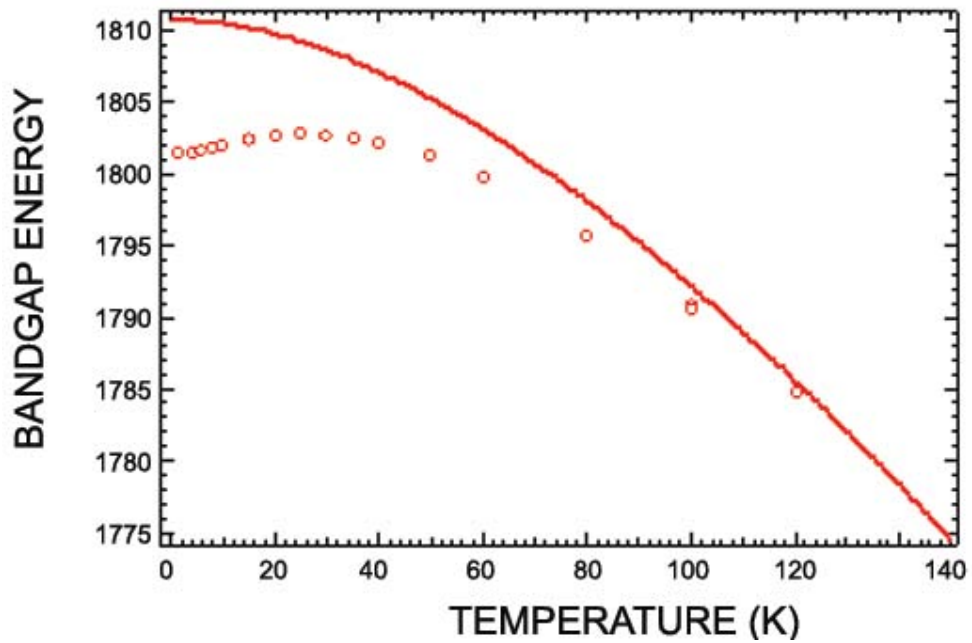


**Figure 2.** The temperature dependence for an  $\text{Al}_{0.20}\text{Ga}_{0.80}\text{As}$  alloy band gap energy. The open circles are the data points and the solid line is the behavior expected from a simple temperature dependent lattice constant model. The difference in energy at low temperatures is a result of random alloy fluctuations of the band gap energy.

## Energy Spectroscopy of the Eigenstates of a Ballistic One-dimensional Double Quantum Wire

by *J. A. Simmons, S. K. Lyo, J. R. Wendt, J. L. Reno, and M. P. Lilly*

**Motivation**—Ballistic one-dimensional (1-D) quantum wires have long been a subject of intense interest in nanoelectronics, for a number of reasons. Not only are they one of the few systems which exhibit a conductance quantized in fundamental units, but their low lying energy excitations are postulated to be those of a Luttinger liquid, rather than the usual Fermi liquid behavior seen in higher dimensions. One dimensional wires thus provide an ideal platform for testing our fundamental understanding of electron transport in condensed matter systems. In addition, due to the greatly restricted electronic density of states and unique degree of control over subband occupancy in 1D, novel electronic devices might be realized in tunnel-coupled structures composed of 1D wires. Indeed, one recent proposal for a solid-state platform for quantum computing involved a coupled pair of quantum wires with variable inter-wire coupling.

**Accomplishment**—We have fabricated a pair of coupled, ballistic, 1D quantum wires. The width of each wire is independently tunable. The tunnel coupling between the wires is also tunable. Using this sample, we have demonstrated the energy spectroscopy of the eigenstates of the coupled 1D quantum wire system, and have demonstrated eigenstate-mixing by the application of a magnetic field along the axis of the wire.

We used the epoxy-bond-and-stop-etch (EBASE) flip-chip technique to define a pair of vertically aligned split gates by electron beam lithography *on each side* of an AlGaAs/GaAs double quantum well heterostructure, as shown in Fig. 1. The epitaxial layer thickness is only

3000 Å. The two high mobility 200 Å quantum wells were separated by 11 Å.

A negative gate voltage defines the (very short) 1D wires by depleting electrons everywhere beneath them, leaving a small 1D wire in the gap between the gates. Further varying the top or bottom gate voltage varies the number of occupied 1D sublevels in the top or bottom wire, respectively, enabling independent control of the two wires. Since each sublevel contributes  $e^2/h$  to the conductance, plateaux in the conductance occur when an integer number of sublevels are occupied. Hence, the position of plateaux versus gate voltage yields an energy spectroscopy of the coupled system. Figure 2 shows contour plots of the derivative of the double quantum wire conductance versus gate voltages, where white represents a plateau. While at zero magnetic field the 1D sublevels exhibit numerous crossings, a magnetic field of 2T causes the eigenstates in each wire to mix, and thus the upper wire and lower wire states to repel each other whenever their energies coincide. This manifests itself as a number of anticrossings, yielding characteristic "fish-eye" shapes in the contour.

**Significance**—This is the first time a double quantum wire with this degree of tunability and control has been demonstrated. This work, which was enabled by our invention and development of the novel fabrication technique, thus presages a number of different experiments including 1D-1D tunneling, lateral Aharonov-Bohm effects, and transport in coupled double quantum dots. The ballistic transport of these samples allows them to be investigated at the wavefunction level.

**Sponsors for various phases of this work include:** BES, LDRD

**Contact:** Jerry A. Simmons, Semiconductor Materials and Device Sciences, Department 1123

Phone: (505) 844-8402, Fax: (505) 844-3211, E-mail: jsimmon@sandia.gov

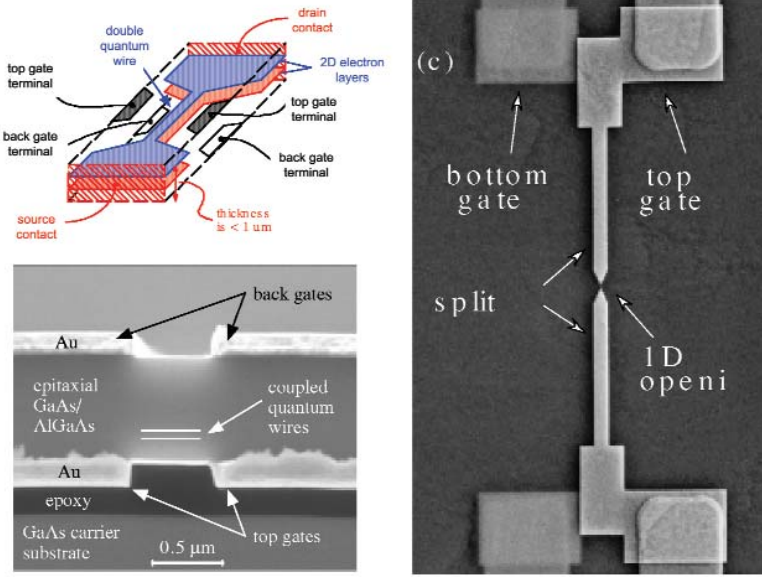


**Figure 1.** Double quantum wire sample. Upper left shows a schematic. Lower left shows a cross section of a test structure, showing the gates on both sides of the epitaxial layers. Right shows a birds eye view. Gate leads on the bottom side of the sample are visible through the epitaxial layers.

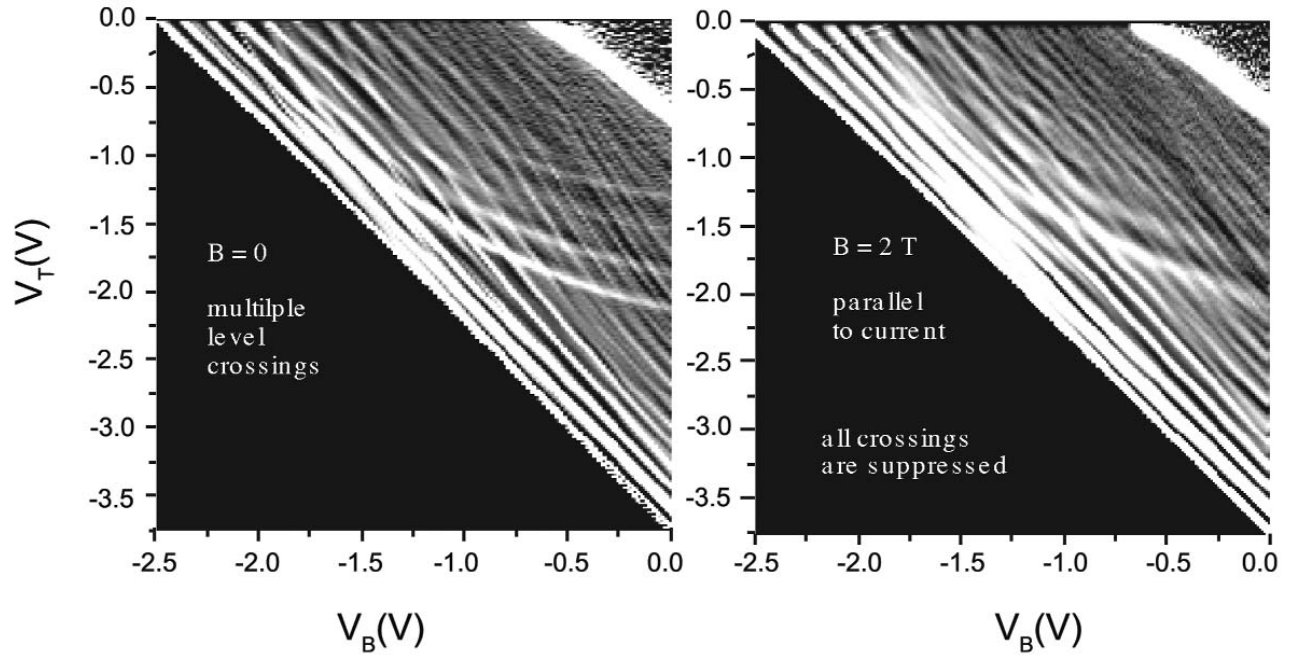


**Figure 2.** Contour plots of the derivative of the conductance of a coupled double quantum wire at 0.3 K. Left is for zero magnetic field, right is at 2 T along the current. White shows a low derivative value, corresponding to a plateau in the conductance. Thus every white line occurs when the Fermi level lies between 1D subband energies, yielding a spectroscopy of energy levels as a function of top ( $V_T$ ) and bottom ( $V_B$ ) split gate bias. Field-induced state-mixing produces anticrossings, at right.

## Theory of Quantum Dot Lasers

*by H. C. Schneider and W. W. Chow*

**Motivation**—Considerable effort is currently devoted to developing quantum dot (QD) lasers. Because of their unique zero-dimensional electronic structure, QDs have many interesting and advantageous properties for opto-electronic device applications. Ultra low and temperature insensitive lasing threshold currents have been experimentally demonstrated. Future developments are likely to include operation under high excitation and high modulation rate conditions. For these situations, not only are the QD states occupied, but the two-dimensional carrier states in the quantum well region surrounding the dots will also be appreciably populated. As a result, many-body Coulomb effects become important, and they cause deviations from idealized zero-dimensional behavior.

**Accomplishment**—We have developed a theory for QD lasers that is also valid for high excitation or high modulation rate operation. Our approach takes into account the interactions between the carriers in the localized quantum-dot states, and the two-dimensional electron-hole plasma occupying the extended quantum-well states. These many-body Coulomb interactions are described at the level of a Hartree-Fock approximation. The influence of the QD potentials on the extended quantum-well states are also be taken into account in the many-body calculations.

Figure 1 depicts typical absorption/gain spectra computed with our theory. The calculations are performed for shallow QDs in the

GaInAs/AlGaAs material system and room temperature. The spectra show the changes in optical response with increasing excitation, where the transition of the quantum dot resonance from absorption to gain is accompanied by a shift to lower energies, due to many-body effects. The carrier density dependence of this screened-exchange shift for the QD is different from that for the quantum well. This difference is shown explicitly in Fig. 2, which plots the quantum dot resonance energy and the quantum well band-edge energy as functions of carrier density. This difference in the two screened-exchange shifts has important consequence on device properties, for example in the carrier transport phenomenon known as the "phonon-bottleneck effect". We plan to further investigate this and other many-body effects. In particular, future development of the theory will include the quantum kinetic treatment of Coulomb correlation effects.

**Significance**—Many applications of quantum dot lasers involve operation under high excitation or high modulation rate conditions. We have developed a many-body theory that is capable of describing laser behavior for those situations. Our theory provides a theoretical understanding of quantum dot optical properties, and shows that for high excitation or high modulation rate operation a consistent treatment of the many-body Coulomb interactions between the quantum dots and the surrounding quantum well is necessary.

---

**Sponsors for various phases of this work include:** LDRD

**Contact:** Weng W. Chow, Semiconductor Material and Device Sciences, Department 1123

Phone: (505) 844-9088, Fax: (505) 844-3211, E-mail: wwchow@sandia.gov



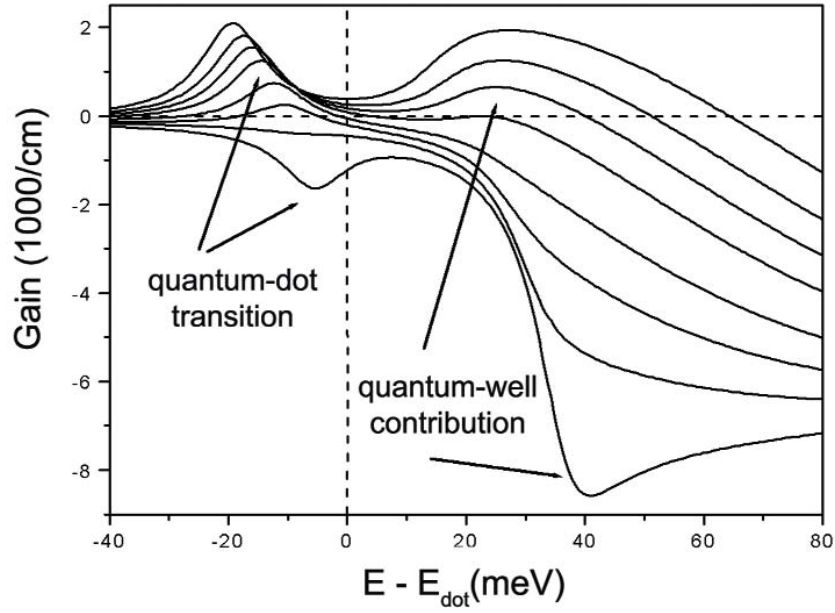


**Figure 1.** Computed gain spectra for quantum-dot laser at 300 K. The two-dimensional density of quantum dots in the well is  $10^{11} \text{ cm}^{-2}$ . The total carrier density is varied from  $3 \times 10^{11} \text{ cm}^{-2}$  (bottom curve) to  $1.5 \times 10^{12} \text{ cm}^{-2}$  (top curve). The zero of the energy scale corresponds to the dot transition-energy at zero carrier density.

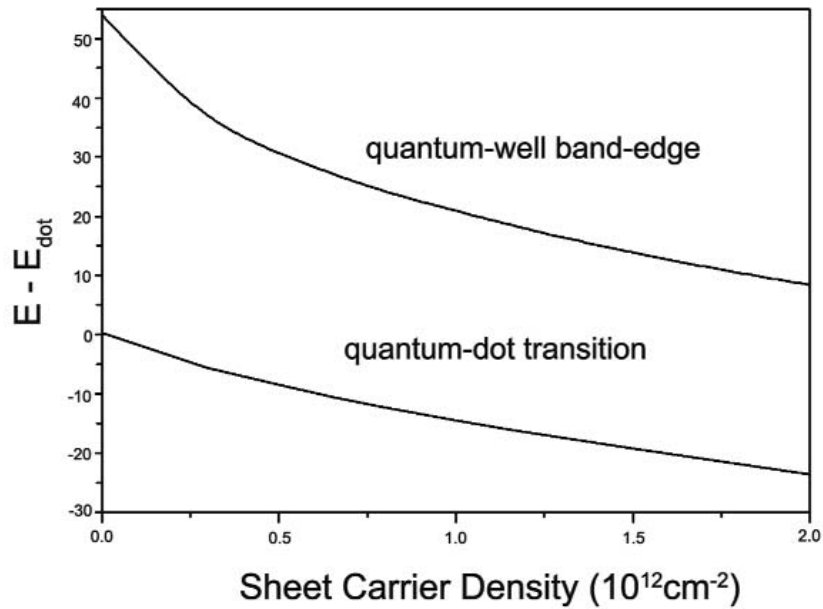


**Figure 2.** Quantum-dot transition energy and quantum-well band-edge at 300 K versus carrier density.

## Coupled-Resonator Vertical-Cavity Laser Diodes

by A. J. Fischer, W. W. Chow, K. D. Choquette, K. M. Geib, A. A. Allerman

**Motivation**—Laser resonators based on two or more optically coupled sections have been used in edge emitters to enable single mode operation, bistable laser output, and extremely high speed pulsed operation. Analogous improvements in device performance can be achieved using coupled-resonator vertical-cavity lasers (CRVCLs). In this scheme, two vertical-cavity surface-emitting lasers are optically coupled via a common middle mirror. CRVCLs combine the benefits of optically coupled resonators with the attractive attributes of VCSELS such as high efficiency, low threshold, and well-defined circular far field patterns.

**Accomplishment**—Lasing was demonstrated in electrically-injected CRVCLs which were grown by metalorganic chemical vapor deposition. As shown in Fig. 1(a), the devices consisted of a bottom p-type GaAs/Al<sub>0.94</sub>Ga<sub>0.16</sub>As distributed Bragg reflector (DBR) with 36 periods, a middle n-type DBR with 11.5 periods, and a top p-type DBR with 22 periods. The top and bottom one-wavelength optical cavities were either active or passive where the active cavities contained five 8 nm GaAs quantum wells. Figure 1(b) shows reflection from a CRVCL wafer. Due to the optical coupling, two cavity resonances ( $\lambda_L$  and  $\lambda_S$ ) are observed where the splitting is determined by the reflectivity of the middle n-type DBR. The inset of Fig. 1(b) shows the calculated splitting as a function of middle mirror pairs where the splitting increases as the reflectivity of the middle mirror is reduced. The observed splitting of 14.2 nm agrees well with the expected splitting 13.3 nm.

Three terminal optoelectronic devices were fabricated to allow independent current injection into either cavity. Figure 2(a) shows Q-switched

pulses generated using an active/passive CRVCL. The bottom cavity had GaAs quantum wells to provide gain and was biased above threshold at 14 mA direct current. The top cavity, which had only a thick absorbing layer of GaAs, was supplied with a -4 V bias and +20 dBm of RF power at 0.88 GHz. Absorption in the passive cavity was modulated by the applied RF power to create Q-switched pulses as short as 150 ps. Devices with gain in both optical cavities were also fabricated. As shown in Fig. 2(b), an active/active CRVCL can exhibit bistable operation of the light output with variations in bottom cavity input current. By varying the bias to the top cavity, the CRVCL could be switched from high power lasing (~6 mW) to very low power spontaneous emission (~40  $\mu$ W). This high contrast switching will find applications in a wide variety of data encoding applications. Active/active CRVCLs also demonstrated other interesting properties such as high single-mode power (> 6.0 mW) and simultaneous lasing at both longitudinal cavity resonances.

**Significance**—CRVCLs expand the useful operating regime of vertical-cavity surface-emitting lasers. One important advantage of a CRVCL over an edge emitter is the ease of tailoring the coupling between cavity sections by varying the number of mirror pairs in the middle DBR during the growth. For an edge emitter, the coupling is normally fixed by the index step at the semiconductor air interface. This difference enabled us to study devices with a wider range of cavity coupling and hence to demonstrate interesting device operating behavior such as Q-switched pulse generation, bistable operation, and high single-mode power.

**Sponsors for various phases of this work include:** LDRD

**Contact:** Arthur J. Fischer, Semiconductor Material and Device Sciences, Department 1123

Phone: (505) 844-6543, Fax: (505) 844-3211, E-mail: ajfisch@sandia.gov

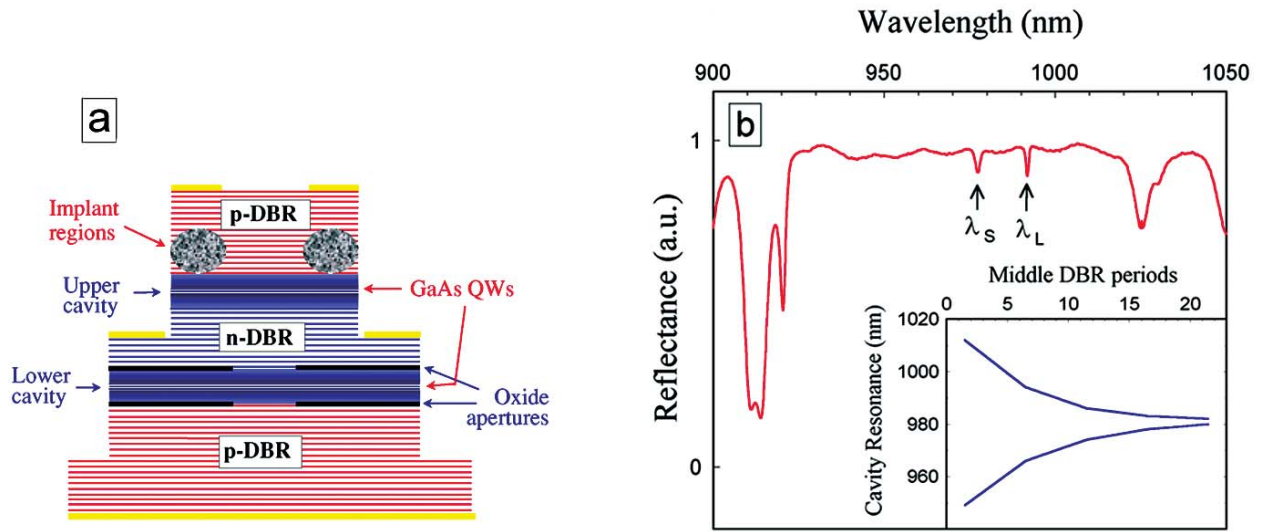


**Figure 1.** (a) Schematic of a coupled-resonator vertical-cavity laser diode. (b) Reflection data showing two longitudinal cavity resonances ( $\lambda_S$  and  $\lambda_L$ ). The inset shows the calculated splitting as a function of middle DBR mirror pairs.

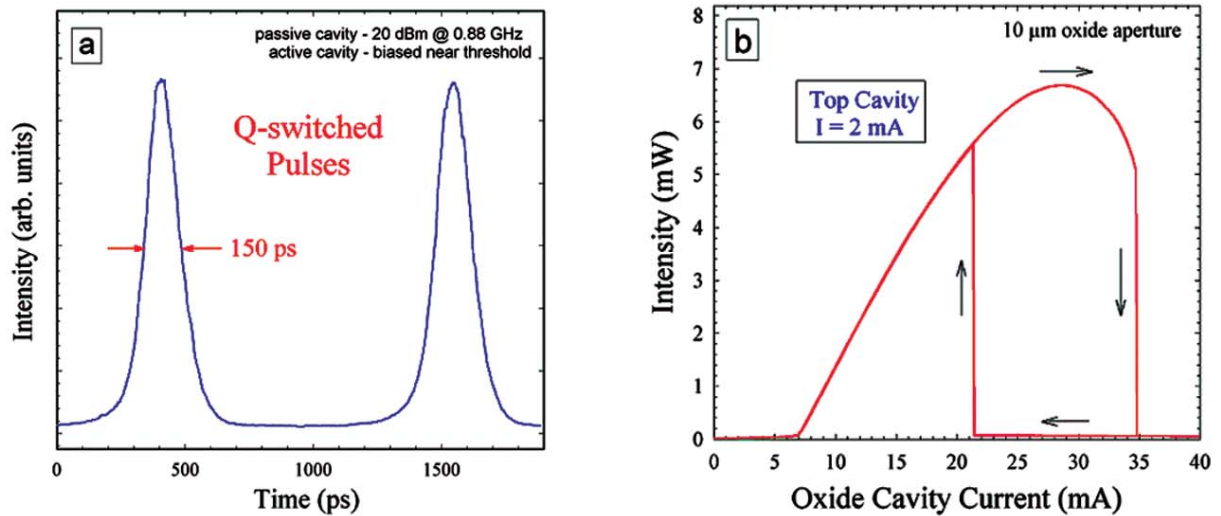


**Figure 2.** (a) Q-switched pulses from an active/passive coupled-resonator vertical-cavity laser. (b) Bistable operation of an active/active coupled-resonator vertical-cavity laser. By varying the bias to the top cavity, the device output could be switched from lasing at ( $\sim 6$  mW) to subthreshold luminescence ( $\sim 40$   $\mu\text{W}$ ).

## 10 Million $\text{cm}^2/\text{Vs}$ Mobility GaAs/AlGaAs Heterostructures and the Metallic Behavior of Dilute 2D Electron Systems

by *M. P. Lilly\** and *J. R. Reno*

**Motivation**—Low dimensional electronic structures can exhibit new physics phenomena that may provide the operating principles for novel nanoelectronic devices. Eventually, these may provide superior alternatives to today's conventional electronics. However, studies of electronic interactions in low-dimensional and nanoscale systems requires disorder to be minimized and interactions emphasized. Here we describe two advances supporting these studies: (1) achievement of high mobility 2D electron gases (2DEGs) and (2) fabrication techniques to produce ultra-low density electron systems.

**Accomplishment**—When delicate interactions between charge carriers or nanostructures is important, it is critical to use a material system where disorder can be minimized. For 2D electron systems, this material system is GaAs/GaAlAs grown by molecular beam epitaxy. With a combination of improvements to the growth chamber and fine-tuning of growth conditions (temperature, alloy concentration, etc.), we have demonstrated a 2DEG in a 30 nm quantum well with a mobility in excess of  $10^7 \text{ cm}^2/\text{Vs}$ . In Fig. 1, the perpendicular magnetoresistance of one such 2DEG is shown. The several delicate higher order fractional quantum Hall states present testify to the very high quality material growth.

One technique to emphasize interactions in 2DEGs is to lower the density. As the density decreases, the ratio ( $r_s$ ) of potential to kinetic energy of the electrons increases. When  $r_s \approx 32$ , interactions become so strong that an electron solid (Wigner crystal) is expected to form. Low density 2DEGs in conventional doped

heterostructures are very difficult to achieve. In order to attain low density, we use an *undoped* GaAs/AlGaAs heterostructure fabricated in a field-effect transistor (FET) geometry (Fig. 2, diagram). Ohmic contacts are placed in close proximity to an overall gate. A voltage on the gate draws carriers from the contact region into the 2D channel. With this technique, we have succeeded in making a 2DEG with a density that is tunable over two orders of magnitude. Due to the very low disorder, the density can be as low as  $3 \times 10^9 \text{ cm}^{-2}$ , not previously observed.

At zero magnetic field, the resistivity of a 2DEG typically decreases with temperature as a result of dynamic scattering processes such as phonons. At low temperature, the phonons freeze out and the remaining resistance is attributed to static disorder. In our gateable system, the above behavior is observed for high density ( $n > 10^{10} \text{ cm}^{-2}$ , red curve in Fig. 2). At lower densities, however, we observe a low temperature peak in the resistivity that cannot be attributed to dynamic scattering. At these densities, the Fermi temperature is reduced to a point that the 2D electron system is no longer degenerate. The peak arises from a combination of screening effects and a crossover from a degenerate Fermi system to a classical system. At higher densities, these subtle features are completely overwhelmed by phonons.

**Significance**—The advances described here will benefit fundamental studies of interacting nanoscale systems. By starting with high mobility material and utilizing the range of processing techniques at Sandia, novel structures such as electron-hole bilayers are possible.

\*Collaborators: J. P. Eisenstein, Caltech; L. N. Pfeiffer and K. W. West, Lucent Technologies.

**Sponsors for various phases of this work include:** BES, LDRD

**Contact:** Michael P. Lilly, Semiconductor Materials and Device Sciences, Department 1123

Phone: (505) 844-4395, Fax: (505) 844-1197, E-mail: mplilly@sandia.gov

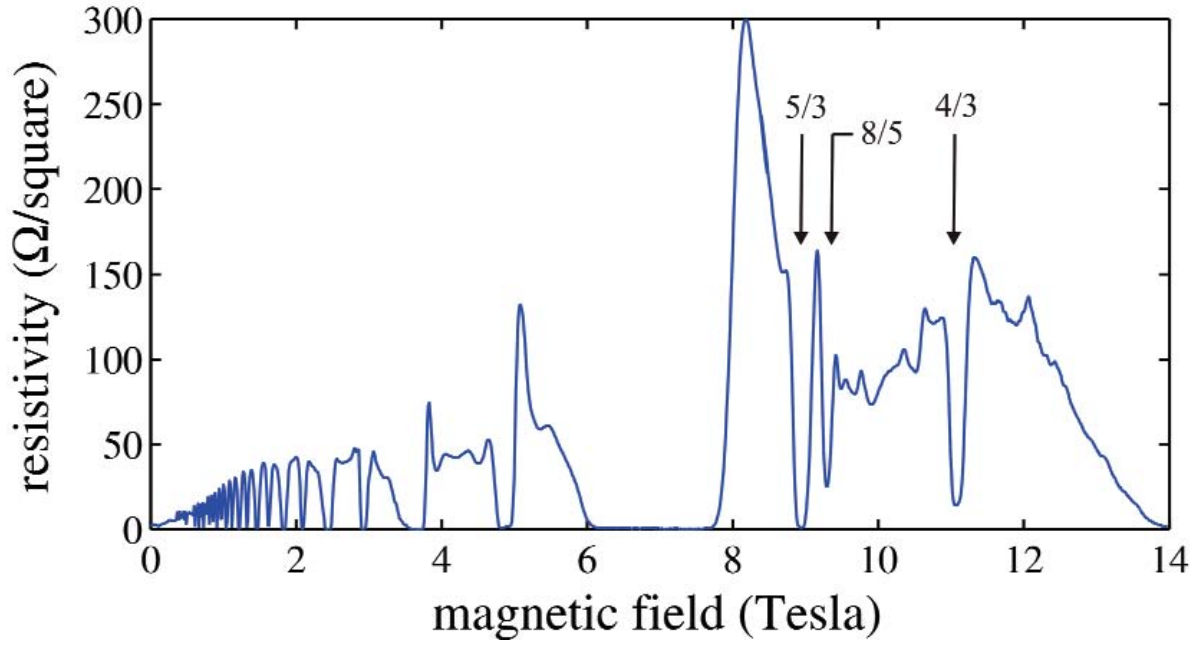


**Figure 1.** Magnetoresistance of a high mobility 2D electron gas at  $T=0.3$  K. The high quality of this sample is indicated by the presence of a number of fractional quantum Hall states (arrows).

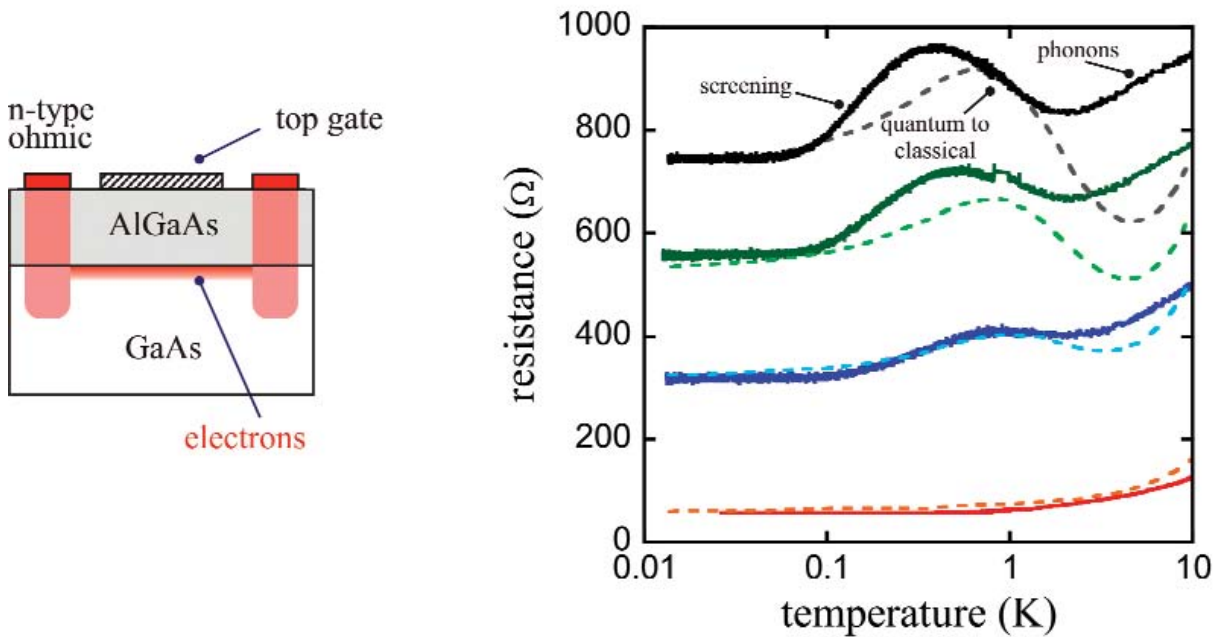


**Figure 2.** The diagram illustrates the FET geometry of the undoped heterostructure. In the graph, the solid lines are the experimental resistance measurements of a 2D electron gas for densities  $0.35$  (black),  $0.40$  (green),  $0.64$  (blue) and  $1.82$  (red)  $\times 10^{10} \text{ cm}^{-2}$ . Dashed lines are the results of a calculation of ionized static impurity scattering (Huang and Das Sarma, private communication). The curves exhibit a hump-like feature due to a crossover from a degenerate Fermi system to a classical system, observable only at low density.



## Emissivity-correcting Pyrometry of Semiconductor Growth

by W. G. Breiland, L. A. Bruskas, A. A. Allerman, and T. W. Hargett

**Motivation**—Temperature is a critical factor in the growth of thin films by either chemical vapor deposition (CVD) or molecular beam epitaxy (MBE). It is particularly important in compound semiconductor growth because one is often challenged to grow materials with specific chemical compositions in order to maintain stringent lattice-matching conditions or to achieve specified bandgap values. Optical pyrometry can be used to measure surface temperatures, but the thin film growth causes significant changes in the emissivity of the surface, leading to severe errors in the pyrometer measurement. To avoid these errors, emissivity changes must be measured and appropriate corrections made to extract an accurate surface temperature.

**Accomplishment**—We have developed an emissivity-correcting pyrometer tool that is specifically tailored to accurately measure surface temperatures during compound semiconductor growth. The data collection and analysis software has been named Thermogrow. It is currently being licensed to an original equipment manufacturer (OEM) for sale to semiconductor thin film equipment vendors.

The Thermogrow emissivity-correcting pyrometer system can measure reflectance and thermal emission at two independent wavelengths. The reflectance data is used in two ways. First, it is used to correct for emissivity changes during growth, allowing one to extract surface temperatures with 1 °C precision throughout a thin-film deposition run. Second, the reflectance is used with a previously-developed Sandia tool — Analysis of Deposition using Virtual Interfaces and Spectroscopic Optical

Reflectance (ADVISOR) to perform *in situ* thin film growth rate measurements. This provides a user with real-time information on temperature, growth rate and composition.

In applying the emissivity-correcting method to compound semiconductor growth, we found it necessary to measure and correct for other errors that are unique to each deposition system. At low emissivity values, the effects of detector offsets, reflectance drift, signal scaling errors, and stray thermal emission can lead to large temperature errors. As an example, during the growth of 850 nm mirrors, the pyrometer would produce 40 °C temperature artifact errors even when emissivity correction was used. We developed a way to account for all the above errors by devising an *in situ* calibration method. Analysis of the calibration run allows one to extract a single empirical parameter that accounts for all the unique errors of a particular deposition system. This parameter is employed in a slightly modified pyrometer algorithm to make artifact-free *in situ* surface temperature measurements during growth. Temperature precision is 1 to 3 °C, even in regions with low (< 20%) emissivity.

**Significance**—The Thermogrow pyrometer method has allowed semiconductor crystal growers to maintain accurate control of temperature for a variety of applications, increasing the yield of device production and enabling more complex device structures to be grown. It has proved to be particularly useful in low-nitrogen InGaAsN alloys where the bandgap is very sensitive to deposition temperature. A joint patent with EMCORE Corporation has been filed and the technology is being transferred to the commercial sector.

---

**Sponsors for various phases of this work include:** CRADA, BES

**Contact:** William G. Breiland, Chemical Processing Sciences, Department 1126

Phone: (505) 844-7029, Fax: (505) 844-3211, E-mail: wgbreil@sandia.gov

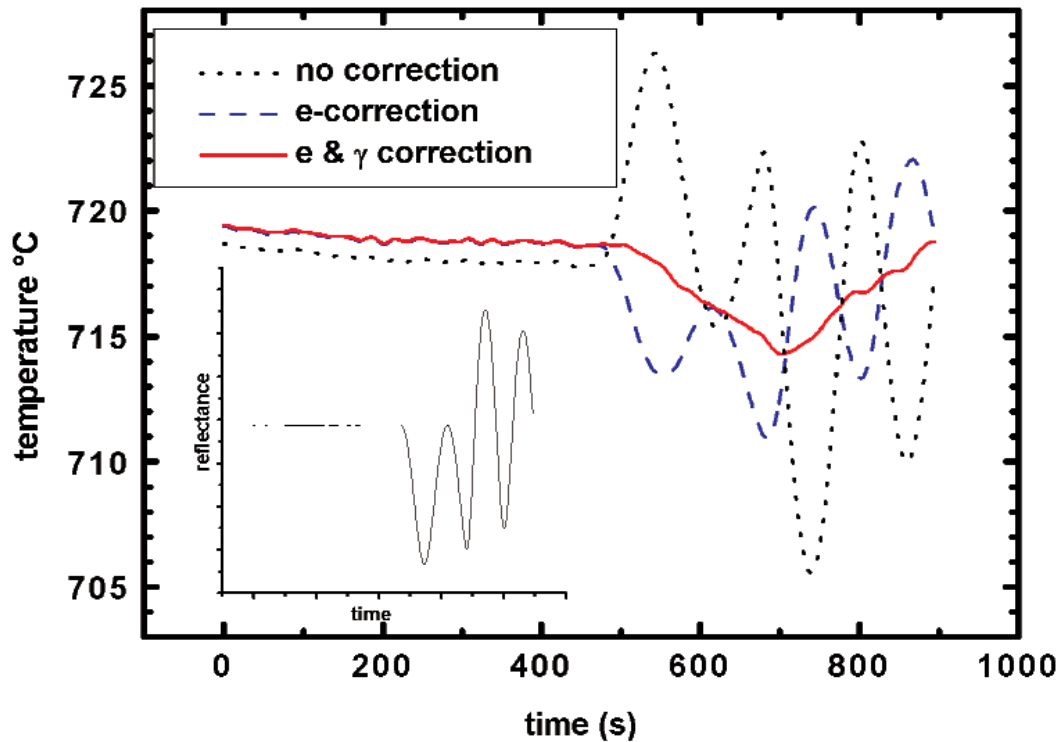


**Figure 1.** Example of the improvements in temperature measurement achieved by the Thermogrow method. The dotted curve shows the pyrometer temperature that is measured during the growth of an AlAs film followed by a GaAs film on a GaAs substrate. The large changes in reflectance from thin-film interference effects (shown in inset) cause large changes in the wafer emissivity. Compensating for the emissivity gives the dashed curve. Although the artifacts caused by emissivity changes are reduced, deposition-chamber specific factors lead to overcompensation errors. Thermogrow uses an in situ calibration method which measures a single empirical parameter that can correct for five deposition chamber errors. The result of this additional correction is shown with the solid curve. Subtle temperature changes caused by different materials on the wafer surface can now be resolved.

# Wide Bandgap Compound Semiconductors



## Dynamic Model of Hydrogen in GaN

by *S. M. Myers and A. F. Wright*

**Motivation**—Hydrogen is incorporated into p-type GaN during MOCVD growth, producing highly stable passivation of the Mg acceptors. Complete acceptor activation by thermal H release requires temperatures that threaten material integrity, prompting compromises in device processing. At lower temperatures, forward bias of p-n junctions or electron-beam irradiation produces a metastable, reversible activation without H release. To understand and control such effects, we are developing a mathematical model of H behavior wherein state energies from density-functional theory are employed in diffusion-reaction equations. Previously, we used the greatly simplifying assumptions of local equilibrium among states and local charge neutrality to treat uniform materials at high temperatures. Now, an extended diffusion-reaction formalism includes nonequilibrium, and a simultaneous solution of Poisson's equation takes account of space charge, allowing H to be modeled in junction devices, under bias, and at room temperature.

**Accomplishment**—Calculations using density-functional theory identified the important lattice states of H as  $H^+$ ,  $H^0$ ,  $H^-$ , interstitial  $H_2$ , the neutral Mg-H complex, and, in n-type material containing Si donors, the neutral Si-H center. Formation energies were calculated for these states, together with local-mode vibrational frequencies affecting the H chemical potential and diffusion activation energies for the mobile species  $H^+$ ,  $H^0$ , and  $H^-$ . Also, captured-electron energies were theoretically evaluated for  $H^+$ ,  $H^0$ , and the Mg-H complex to elucidate the reaction path of the aforementioned metastable activation of acceptors in p-n junctions under minority-carrier injection. To describe the time evolution of the system,

differential equations were developed for the time and depth dependent concentrations of the above H states as well as  $Mg^-$ ,  $Si^+$ , conduction electrons, holes, and net charge. The resulting formalism is solved numerically. Among the properties of the solution is that it reproduces our earlier treatment of thermodynamic equilibrium, which was validated by measurements of H solubility, and also our prior modeling of thermal release, similarly found to be consistent with experiment.

Applications of our newly extended model are exemplified by results for the metastable activation of Mg acceptors in a p-n junction under forward bias. We find that interstitial  $H_2$  is the only viable candidate for the state of the H produced in this treatment. Additionally, we have predicted the rate at which the metastable activation is reversed during heating, as shown in Fig. 1. These results indicate that half-hour isochronal anneals will begin to restore the passivation at about 350°C, which agrees with published observations. As another example, the model shows H being strongly excluded from the space-charge region of a p-n junction, as seen in Fig. 2, leading to bias-driven H redistributions with device implications at temperatures extending below 100°C.

**Significance**—Through modeling a range of observable behaviors in terms of states predicted by *ab-initio* theory, we are validating and refining the understanding of H in GaN. These calculations are more quantitative and comprehensive than past treatments of H in semiconductors. Results are clarifying trade-offs in device processing and have already influenced processing protocols.

**Sponsors for various phases of this work include:** BES, Nuclear Weapons/Science and Technology

**Contact:** Sam M. Myers, Nanostructure and Semiconductor Physics, Department 1112

Phone: (505) 844-6076, Fax: (505) 844-7775, E-mail: [smmymyers@sandia.gov](mailto:smmymyers@sandia.gov)

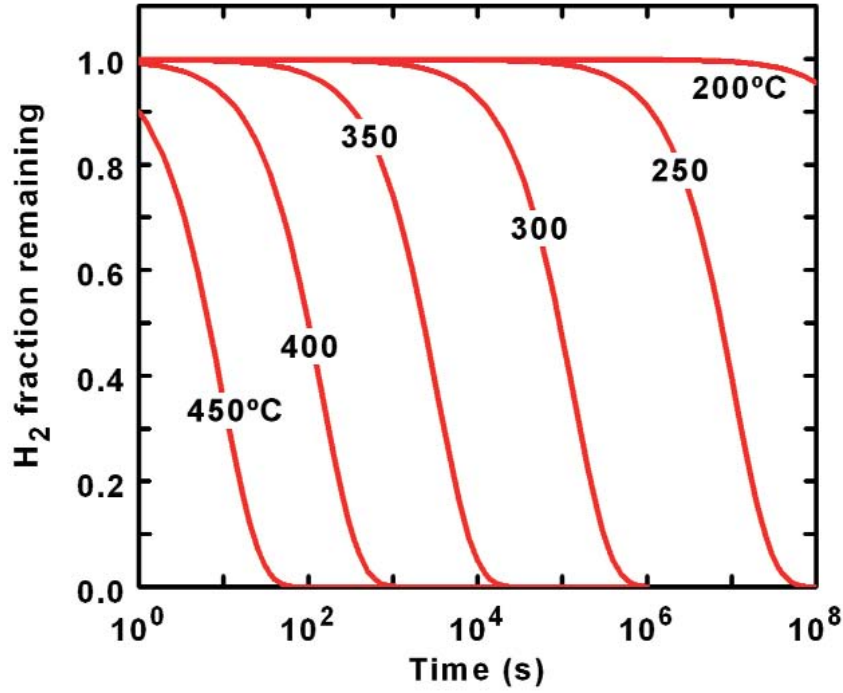


**Figure 1.** Theoretically predicted repassivation of Mg acceptors in GaN during annealing with no bias. Plotted versus time is the decreasing fraction of interstitial  $H_2$  as the H returns to the acceptors and reforms the neutral Mg-H center.

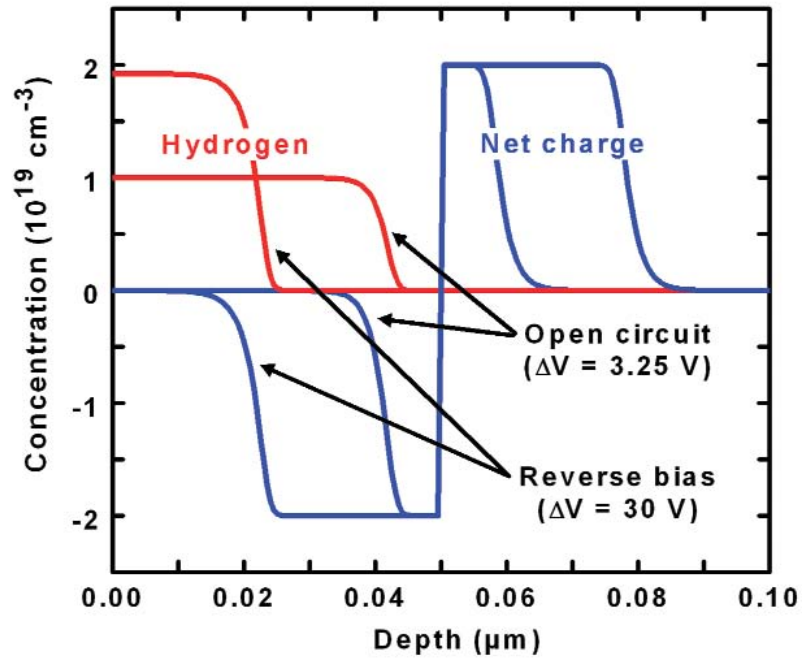


**Figure 2.** Theoretically predicted H redistribution in a p-n junction under bias with space charge also shown. In the model, H was first diffused into the p-type region from the surface under open circuit conditions and then caused to redistribute by the application of a reverse bias. The temperature is 400°C, and the plotted depth profiles are for the asymptotically approached conditions.



## High Power Electronics Based on the 2D Electron-Gas in GaN Heterostructures

by *S. R. Kurtz, A. A. Allerman, and D. Koleski*

**Motivation**—GaN-based electronics offer miniaturization potential of radical proportions for microwave power amplifiers. GaN's large bandgap, high breakdown field, high electron velocity, and excellent thermal properties have led to high electron mobility transistors (HEMT) with up to 10x the power density of GaAs and other traditional semiconductors at frequencies up to 20 GHz.

Further contributing to the outstanding performance of GaN-based amplifiers is the highly conducting, 2-dimensional electron gas (2DEG) used for the HEMT channel. Intrinsic polarization and piezoelectric properties of GaN materials can produce a 2DEG at an AlGaIn/GaN interface with a sheet carrier concentration of  $10^{13}/\text{cm}^2$ , well in excess of that achievable in any other III-V material system. The physics and material science of the AlGaIn/GaN 2DEG are critical to the performance and future development of GaN-based electronics.

**Accomplishment**—High quality AlGaIn/GaN heterostructures have been grown on sapphire substrates using an AlN nucleation layer. Capacitance-voltage and transport measurements confirm that 2DEG sheet densities  $>10^{13}/\text{cm}^2$  have been achieved at 300 K, Hall mobilities  $>1000 \text{ cm}^2/\text{Vs}$  at the highest densities. A depth profile of the 2DEG is shown in Fig. 1. Experimental results are compared with Schrodinger-Poisson calculations of AlGaIn/GaN conduction band-bending and 2DEG concentrations shown in Fig. 2. These bandstructure results are incorporated into a finite element, charge-control HEMT model which includes both saturation velocity and

injected space charge effects, in addition to the solid state properties of the AlGaIn/GaN interface and 2DEG.

No high quality GaN substrate has been developed to grow GaN HEMT structures. As a consequence GaN is most often grown on substrates with a considerably different lattice constant, most commonly sapphire or SiC. Not surprisingly, GaN material is grown with extremely high levels of threading dislocations and point defects. We have begun to evaluate alternative substrates to sapphire. Initial work has focused on the properties of the 2DEG formed within low-dislocation density regions produced through cantilever-epitaxy or epitaxial-lateral-overgrowth. Overall material quality and properties of the 2DEG are monitored with optical and electrical measurements. Novel optical characterization techniques being explored include electroreflectance spectroscopy of 2DEG energy levels and infrared spectroscopy of defect states near the AlGaIn/GaN interface which trap charge, degrading HEMT performance. Unconventional GaN HEMT designs, enabled by novel substrates, are being modeled and evaluated.

**Significance**—Fundamental studies of GaN growth and the unique 2DEG have led to the demonstration of state-of-the-art solid state microwave amplifiers. We have constructed an AlGaIn/GaN HEMT on sapphire, with a power density  $3\text{W}/\text{mm}$  at 3 GHz. Further improvement in GaN materials and growth promise higher mobilities and novel quantum effects of the 2DEG, leading to the next generation of microwave power devices.

---

**Sponsors for various phases of this work include:** Nuclear Weapons/Science and Technology, BES, LDRD

**Contact:** Steven R. Kurtz, Semiconductor Physics, Department 1123

Phone: (505) 844-9637, Fax: (505) 844-3211, E-mail: [srkurtz@sandia.gov](mailto:srkurtz@sandia.gov)

---

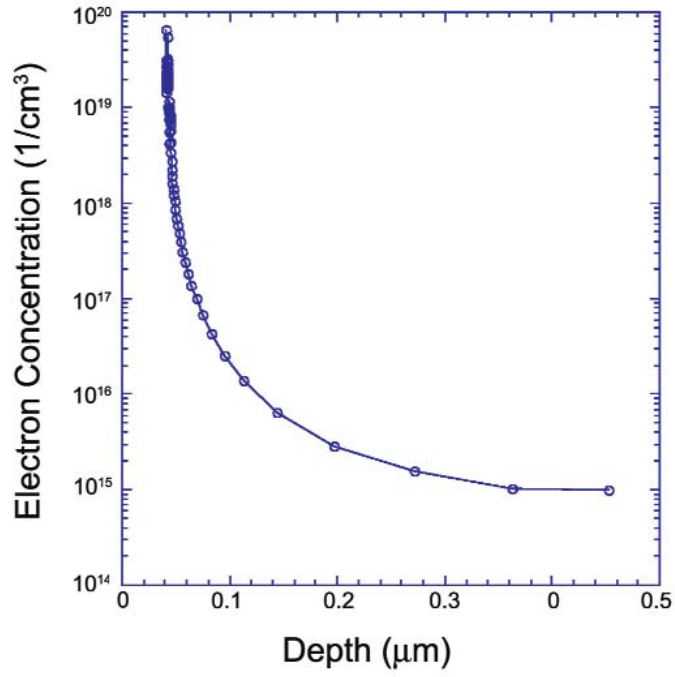


**Figure 1.** 2DEG concentration at an AlGaIn/GaN interface determined by capacitance-voltage measurements.

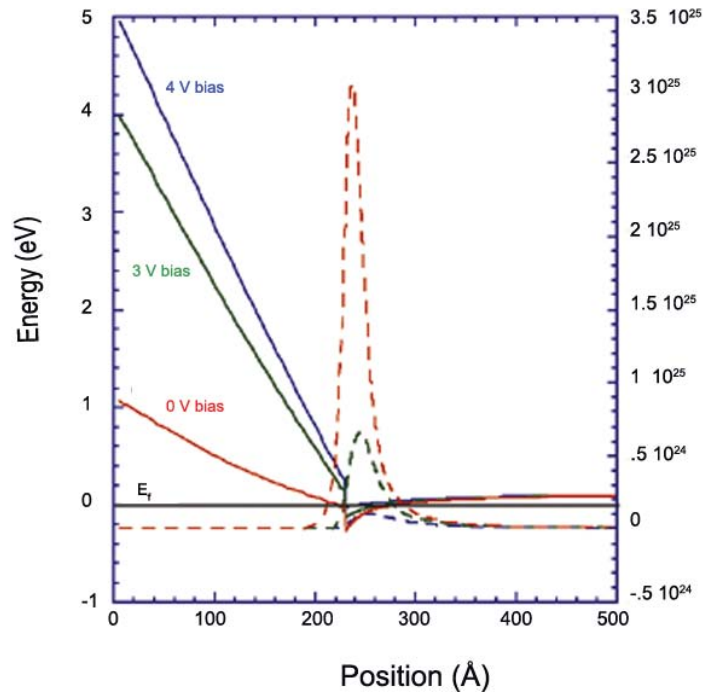


**Figure 2.** Calculation of conduction band energies (solid) and 2DEG concentration (dotted) at an AlGaIn/GaN interface for 0, 3, and 4V bias.

## Optically-pumped UV Lasing from a GaN-based VCSEL

by J. Han, K. E. Waldrip, J. J. Figiel, S. R. Lee, and A. J. Fischer\*

**Motivation**—Compact ultraviolet sources are required for advanced chemical and biological sensors, high density optical storage, and as pump sources for phosphors used in solid-state white lighting. Although GaN-based edge-emitting lasers operating near 400 nm are available commercially, shorter wavelengths as well as other lasing geometries have remained a challenge. In particular, electrically-injected vertical-cavity surface-emitting lasers (VCSELs) have not been demonstrated in the III-Nitrides. VCSELs have unique advantages due to their low cost, compact size, and well-defined circular output beam. Optoelectronic sources based on UV VCSELS will be the enabling component for many advanced sensor, display, and general illumination technologies.

**Accomplishment**—We have demonstrated a technique for producing epitaxial distributed Bragg reflectors (DBRs) with reflectivities greater than  $R = 99\%$ . This resulted in the demonstration of a room temperature, quasi-continuous wave optically-pumped VCSEL operating at 383 nm. The optical resonator consisted of a lower epitaxial GaN/Al<sub>0.20</sub>Ga<sub>0.80</sub>N DBR and an upper dielectric DBR. Using a standard nucleation layer, 1  $\mu\text{m}$  of GaN was grown by metalorganic chemical vapor deposition on a sapphire substrate followed by a 135 Å thick AlN strain compensating layer. Due to the low index contrast between GaN and Al<sub>0.20</sub>Ga<sub>0.80</sub>N, a very thick DBR ( $\sim 5 \mu\text{m}$ ) of 60 alternating quarter-wave layers is required to achieve a reflectivity of  $R > 99\%$ . AlN strain compensating layers were inserted every 20 layer pairs in order to avoid the stress-induced cracking which is normally observed when thick AlGaIn is grown on GaN. The effective use of

strain compensating layers was the key to achieving the crack-free, high reflectivity epitaxial DBRs.

An active region containing 20 In<sub>0.03</sub>Ga<sub>0.97</sub>N/GaN multiple quantum wells was grown to provide gain near 380 nm. A top dielectric DBR composed of SiO<sub>2</sub>/HfO<sub>2</sub> was deposited to complete the optical cavity. The VCSEL structure was optically pumped using the third harmonic of high repetition rate (76 MHz) 100 ps YAG laser. Figure 1 shows the output power of the laser as a function of input pump power with a clear threshold observed near 30 mW of pump power. The inset shows the far field emission pattern of the UV light projected on a fluorescent screen. Figure 2 shows the emission spectrum of the laser above and below threshold. Note the narrow linewidth ( $< 0.1 \text{ nm}$ ) above threshold. The threshold behavior and linewidth narrowing are clear evidence of optically-pumped lasing.

**Significance**—The GaN/Al<sub>0.20</sub>Ga<sub>0.80</sub>N DBR technology demonstrated here can be used in a variety of optoelectronic devices. For example, epitaxial DBRs used in resonant-cavity light emitting diodes (RC-LEDs) are known to improve the light extraction and hence device efficiency. For VCSELs, epitaxially grown DBRs provide a controllable, low cost means of producing high finesse optical cavities. Optically pumped lasing is one important step towards the realization of an electrically-injected UV VCSEL. Electrically-injected UV VCSELs will find applications in a wide array of chemical and biological sensors as well as in display and general illumination technologies.

\*Collaborator: A.V. Nurmikko, Brown University

**Sponsors for various phases of this work include:** LDRD, Nuclear Weapons/Science and Technology

**Contact:** Arthur J. Fischer, Semiconductor Material and Device Sciences, Department 1123

Phone: (505) 844-6543, Fax: (505) 844-3211, E-mail: ajfisch@sandia.gov

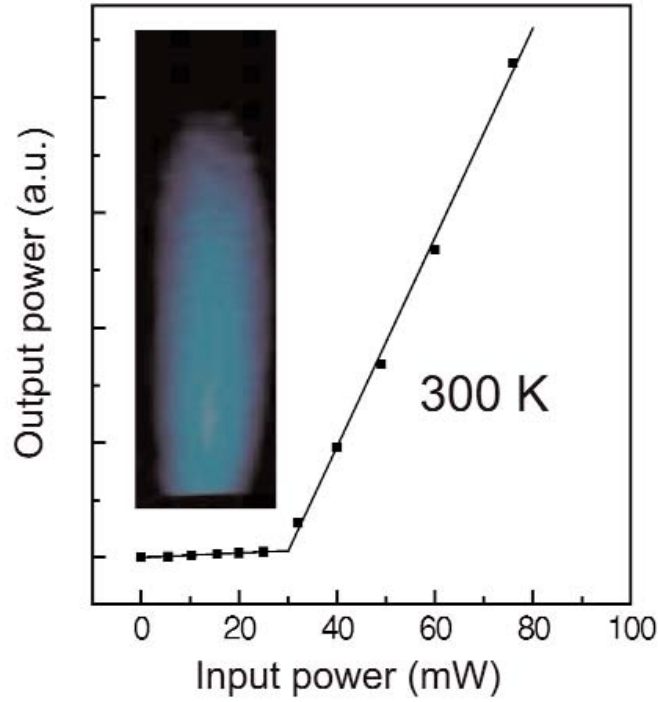


**Figure 1.** Average input power versus output power of a VCSEL device at room temperature. The inset shows the far field pattern of the VCSEL projected onto a fluorescent screen.

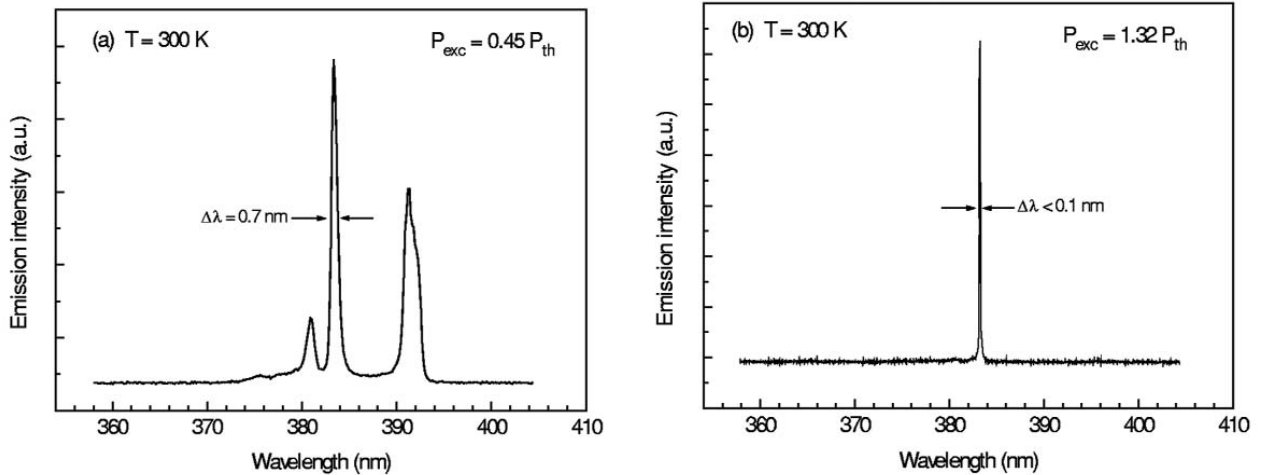


**Figure 2.** (a) Room temperature VCSEL emission spectrum below threshold. (b) VCSEL lasing spectrum above threshold. Note the linewidth narrowing observed above threshold.

## Transport and Kinetic Processes in GaN Epitaxial Lateral Overgrowth

by *M. E. Coltrin and C. C. Mitchell*

**Motivation**—GaN is a wide band gap semiconductor with a broad range of potential applications, e.g., high-temperature electronics, optoelectronics, chemical or biological sensors. GaN thin films usually have a high defect density, leading to poor performance. Epitaxial Lateral Overgrowth (ELO) has been shown to greatly reduce defect densities, often by factors of 100 or more. We are conducting fundamental studies of GaN growth kinetics during ELO.

**Accomplishment**—In ELO, a mask pattern of dielectric material is deposited on top of a GaN buffer layer. Further growth of GaN occurs selectively on exposed areas of the underlying buffer layer, and not on the dielectric material. Many coupled phenomena potentially contribute to observed ELO behavior, including mass transport and anisotropic growth kinetics. Scanning electron microscopy (SEM) is used to measure grown feature sizes. Growth rates depend strongly on the ELO pattern, i.e., size of the window opening,  $w$ , and mask width,  $m$  (or pattern "Pitch"  $\pi=w+m$  and fill-factor  $\theta=w/p$ ).

We examined the ELO growth efficiency, i.e., how much of the Ga reactant is incorporated into the growing ELO feature compared with the incorporation for unmasked, blanket growth. If the rate constant is high enough, the system is transport limited, and ELO growth efficiency is very high. As the reaction rate slows, for example through a decrease in temperature, the deposition rate now depends both on transport processes and on chemical kinetics. As a result, the ELO growth efficiency can be observed to drop. Finite-element analysis of ELO growth efficiency shows these effects quantitatively. In addition to these numerical studies, we have recently derived an analytical model that predicts the ELO efficiency, which depends importantly on the parameter  $Da=k\delta/D$ , a sur-

face Damkohler number, where  $k$  is the rate constant for the deposition reaction,  $\delta$  is the reactor boundary layer thickness, and  $D$  is the diffusion constant.

$$\varepsilon = \frac{\theta(1 + Da)}{1 + \theta Da}$$

When  $Da \gg 1$ , chemistry rates are fast relative to mass transport, and the system is mass-transport limited. At the other extreme, when  $Da$  is unity or below, the system is limited by the chemistry rate. Figure 1 shows remarkable agreement between the above analytical model for ELO efficiency and the exact 2-D diffusion calculations.

Plotted in Fig. 2 are measured cross-sectional areas of the GaN ELO features versus the pattern Pitch. The observation that the 8:4 cross-sectional area matches the 100% efficiency line indicates that the inherent growth chemistry of the (0001) basal plane is very fast. Thus, this feature is in the transport-limited regime. Thus the 1:16 feature is bounded by (1 $\bar{1}$ 01). The observation that this point lies significantly below the unit-efficiency line is a reflection of the slow growth chemistry on that face.

**Significance**—These results have important implications for GaN ELO. Understanding the interplay between transport and kinetics allows us to extract the fundamental growth rates for individual crystal facets. For example, we have determined that the (0001) basal plane intrinsic growth kinetics are a factor of ten greater than for the (1 $\bar{1}$ 01) face, illustrated in Fig. 2. Knowledge of the fundamental growth kinetics enables us to adjust experimental growth conditions to optimize and manipulate growth morphology in ELO as well as in Cantilever Epitaxy.

**Sponsors for various phases of this work include:** BES

**Contact:** Michael E. Coltrin, Chemical Processing Sciences, Department 1126

Phone: (505) 844-7843, Fax: (505) 844-3211 E-mail: mecoltr@sandia.gov



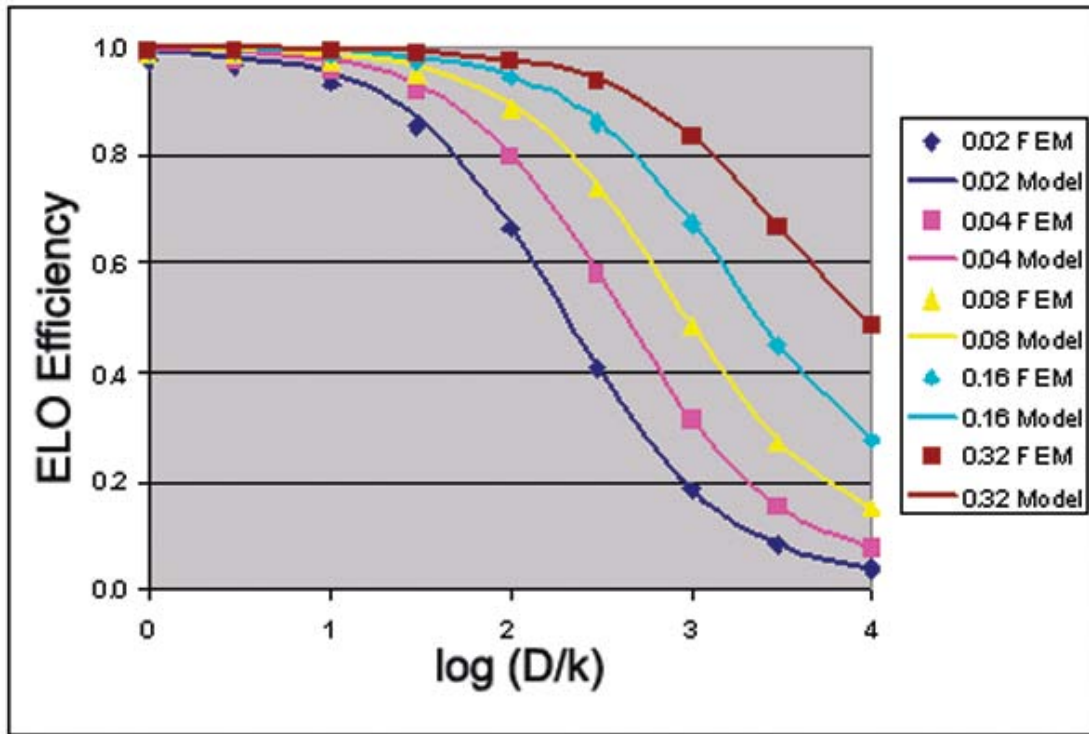


**Figure 1.** Theoretical ELO efficiency as a function of  $D/k$ , a measure of the relative rates of transport vs kinetics, for fill factors ranging from 0.02 to 0.32. Results of the exact finite-element calculation (FEM) are compared to the analytical model.

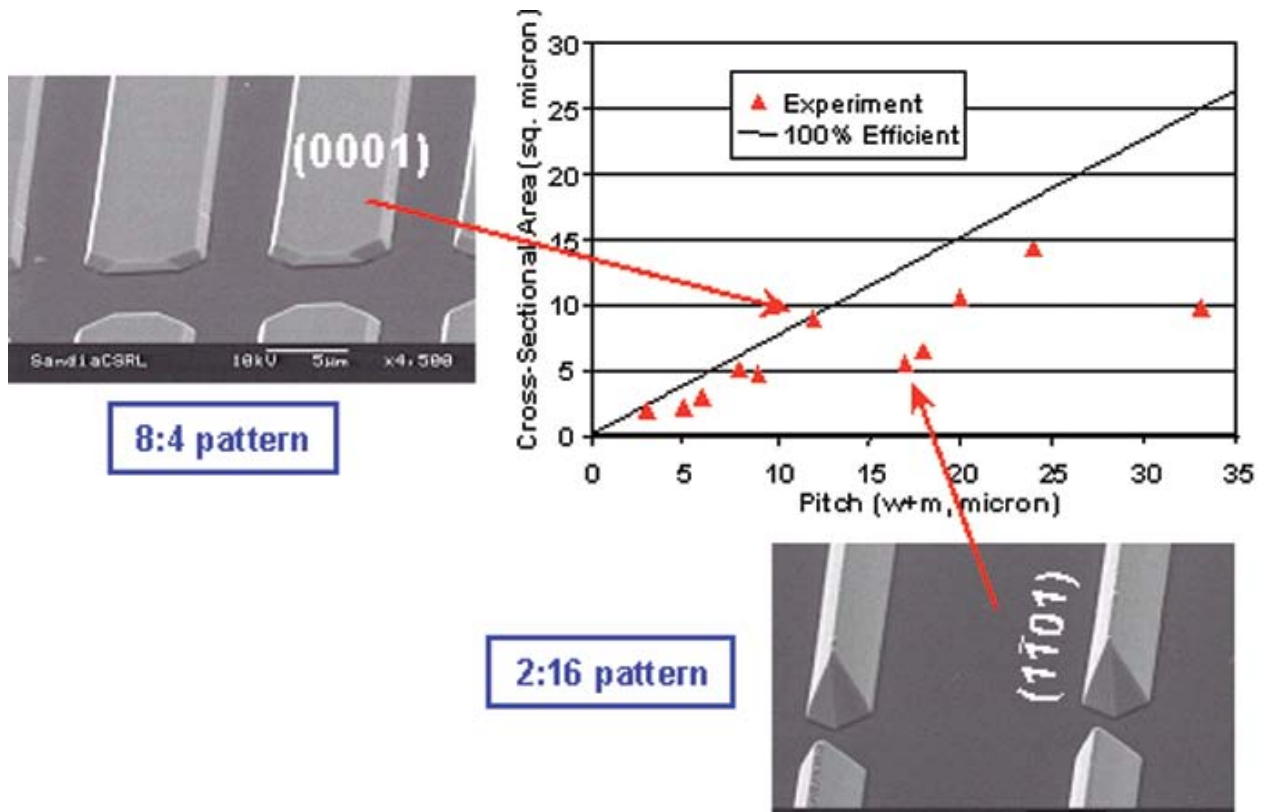


**Figure 2.** Measured cross-sectional areas of GaN ELO features grown on a variety of line patterns, varying  $w$  and  $m$ . Solid line denotes the expected result when ELO transport has unit efficiency.

## Development of Cantilever Epitaxy to Produce High Quality GaN with Reduced Threading Dislocation Densities

by C. C. Mitchell, A. A. Allerman, C. I. H. Ashby, R. D. Briggs, D. M. Follstadt, S. L. Lee, and D. D. Koleske

**Motivation**—GaN grown on any currently available substrates has an inherent problem of having to overcome a large lattice mismatch with the substrate. As a result typical planar GaN includes anywhere from  $10^8$  -  $10^{10}$  threading dislocations per square centimeter. Cantilever epitaxy (CE) is a technique developed to produce areas of GaN with a reduced number of vertical threading dislocations (VTDs) over large areas. Low defect materials are required to reduce leakage and breakdown of both electronic and opto-electronic devices.

**Accomplishment**—This method requires pre-growth processing to create parallel sapphire posts off of which GaN is laterally overgrown. Figure 1 shows a coalesced CE film. CE does not require a dielectric mask, which can cause doping in regrown material. This is particularly important when creating electrical devices such as HEMTs. The lack of a dielectric mask will also allow us to significantly reduce the number of VTDs in AlGaN, which cannot be accomplished with standard overgrowth techniques due to a lack of selectivity on the dielectric mask.

To produce areas of GaN larger than the area grown from a single cantilever post, dislocations have to not only be removed in the overgrown regions, but also have to be removed over the post, and cannot be created when adjacent cantilever wings coalesce. Figure 2 shows a transmission electron micrograph (TEM) of a CE film that has coalesced over a  $4\text{ }\mu\text{m}$  trench from a post that was  $8\text{ }\mu\text{m}$  wide. The number of VTDs in the laterally grown material is reduced by two orders of magnitude when compared to the amount found in the material directly over the post. In addition, TEM results show that

vertical threading dislocations found near the outer  $0.5\text{ }\mu\text{m}$  of the sapphire post turn over and run horizontally i.e. parallel to the sapphire substrate. Further study reveals the turning of vertical dislocations, so that they run horizontally, occurs in other lateral overgrowth techniques such as epitaxial lateral overgrowth (ELO) when steps are taken to insure that the crystal grows to a pyramidal structure before lateral overgrowth commences. This phenomenon provides the opportunity to turn all of the VTDs normally found in the growth over a CE sapphire post by growing to a full pyramid before starting the lateral growth. This pyramidal growth followed by lateral growth to coalescence must occur before growth from the bottom of the trench interferes. The material quality will be compromised by not having free hanging cantilevers.

Atomic force microscopy results concur with TEM results in that the number of VTDs in the laterally overgrown cantilever regions is less than  $1 \times 10^7$ . This is over a two order of magnitude reduction in the number of VTDs when compared to a control section of planar growth. In addition, the VTDs over the post are reduced by an order of magnitude. These results indicate that the proper growth conditions will indeed lead to a situation where vertical threading dislocations over the post are being turned to run horizontally.

**Significance**—Overcoming the difficulties of growing GaN on a substrate with a 14% lattice mismatch is vital to producing reliable, robust electronic and opto-electronic devices. The cantilever epitaxy technique provides an opportunity to do this for a wide range of binary, ternary, and quaternary materials without compromising the electrical characteristics.

---

**Sponsors for various phases of this work include:** BES, LDRD

**Contact:** Christine C. Mitchell, Chemical Processing Sciences, Department 1126

Phone: (505) 845-3550, Fax: (505) 844-3211, E-mail: ccmitch@sandia.gov

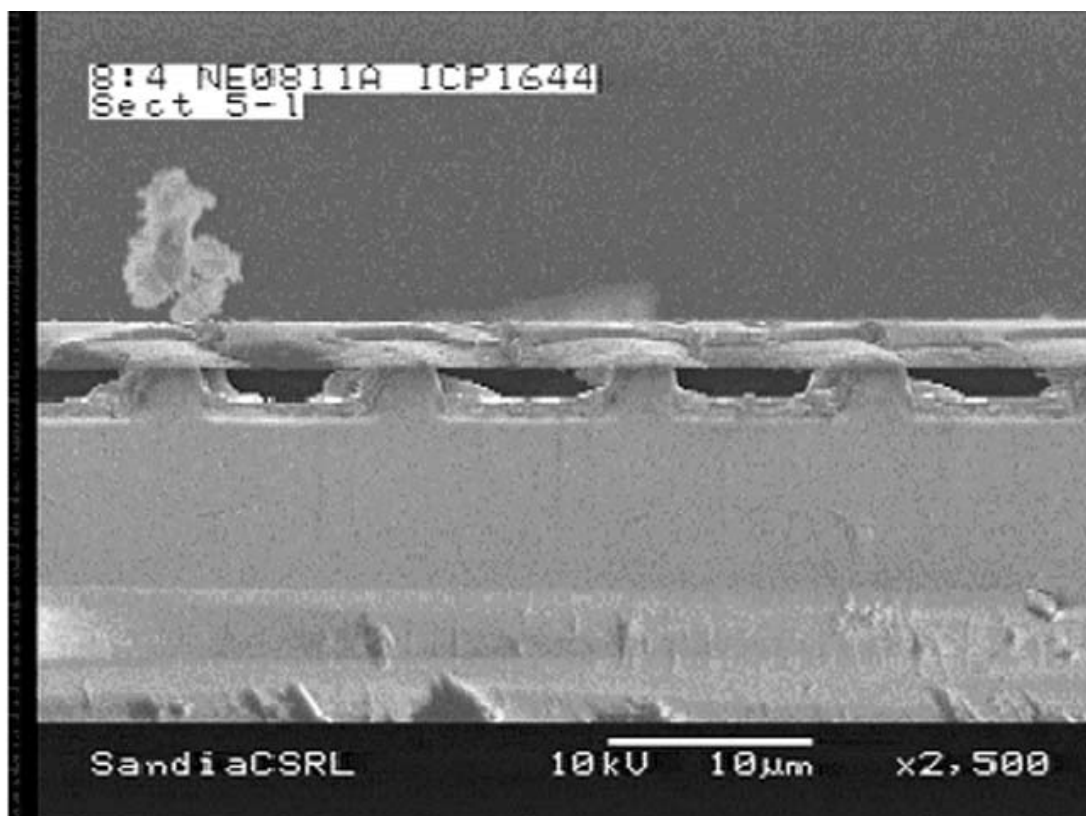


**Figure 1.** Coalesced cantilever epitaxy film grown off of 4  $\mu\text{m}$  posts over 8  $\mu\text{m}$  trenches.

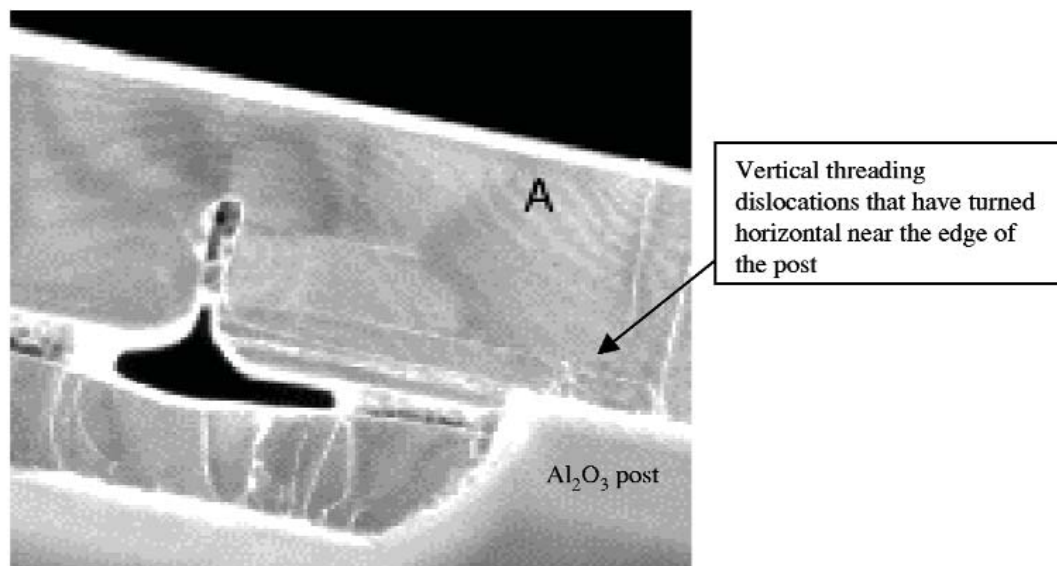


**Figure 2.** TEM of a CE sample shows no visible threading dislocations to the left of section A and vertical threading dislocations turning horizontally near the edge of the sapphire post.

## Identification of the Parasitic Chemical Reactions during AlGaN OMVPE

by J. R. Creighton, M. E. Coltrin, and W. G. Breiland

**Motivation**—GaN and AlGaN alloys are extremely important materials with widespread applications for optoelectronics (e.g., solid state lighting) and high power electronics. Organometallic vapor phase epitaxy (OMVPE) is the primary deposition methodology, but it suffers from several growth chemistry anomalies. Growth rate and alloy composition are often a sensitive function of temperature and other reactor variables. These factors make the AlGaN OMVPE process difficult to control and increase the cost of the material. Conventional wisdom has been that the non-ideal OMVPE behavior is due to parasitic "pre-reactions" between the reactants, but these processes have not been studied in a reliable and thorough manner. An important question is whether the parasitic processes occur at low temperatures (e.g., near the inlet,  $<100^{\circ}\text{C}$ ) or require high temperatures (e.g., near the wafer,  $\sim 1000^{\circ}\text{C}$ ).

**Accomplishment**—We have explored many possible mechanisms for the parasitic pathways using both experimental techniques and complex reactive flow simulations. As expected, trimethylgallium (TMGa) and trimethylaluminum (TMAI) react with ammonia to form adducts, which we have unambiguously identified with mass spectroscopy and FTIR. We have measured the vapor pressure of the adducts near room temperature and found that physical condensation can be an important process, especially at higher reactor pressures and higher reactant concentrations. However, over the  $0$ – $100^{\circ}\text{C}$  range we have found no evidence of significant irreversible decomposition reactions, such as methane elimination (see Fig. 1), which have often been postulated to be the source of the loss of group-III flux. The TMAI: $\text{NH}_3$  adduct does irreversibly react to form  $\text{CH}_4$ , but

this process only becomes detectable above  $125^{\circ}\text{C}$ .

We have modified one of our research rotating disk reactors (RDR) so that TMGa, TMAI, and  $\text{NH}_3$  are premixed before entering the chamber. Growth rates in this RDR are comparable to the growth rates from our RDR where the group-III precursors are kept separate from  $\text{NH}_3$  at the inlet. We have measured growth rates over a wide range of operating conditions and concluded that the parasitic reactions must be occurring in the thermal boundary layer just above the wafer. One example of this type of experiment is the growth rate dependence on spin rate ( $\Omega$ ) shown in Fig. 2. Lowering  $\Omega$  increases the residence time in the boundary layer, which allows the parasitic processes to advance to a greater extent, thus dropping the growth rate. If there were no parasitic loss terms the growth rates would be independent of  $\Omega$  and at the transport limit. A low temperature mechanism would not exhibit the strong  $\Omega$  dependence observed. Many details of the high temperature parasitic mechanisms still need to be resolved, but our current working hypothesis is based on homolysis of TMGa and TMAI, followed by gas-phase association reactions (e.g., particle nucleation).

**Significance**—By showing that the parasitic mechanism requires high temperatures, we were able to use a reactor design with premixed gases. Premixing eliminates a major source of nonuniformity in the system. By understanding the details of the high-temperature parasitic mechanism we will be able to optimize the AlGaN OMVPE process. We have already found that for GaN we can reach the transport limit by increasing the spin rate (Fig 2).

---

**Sponsors for various phases of this work include:** BES, LDRD

**Contact:** J. Randall Creighton, Chemical Processing Sciences, Department 1126

Phone: (505) 844-3955, Fax: (505) 844-3211, E-mail: jrcreig@sandia.gov



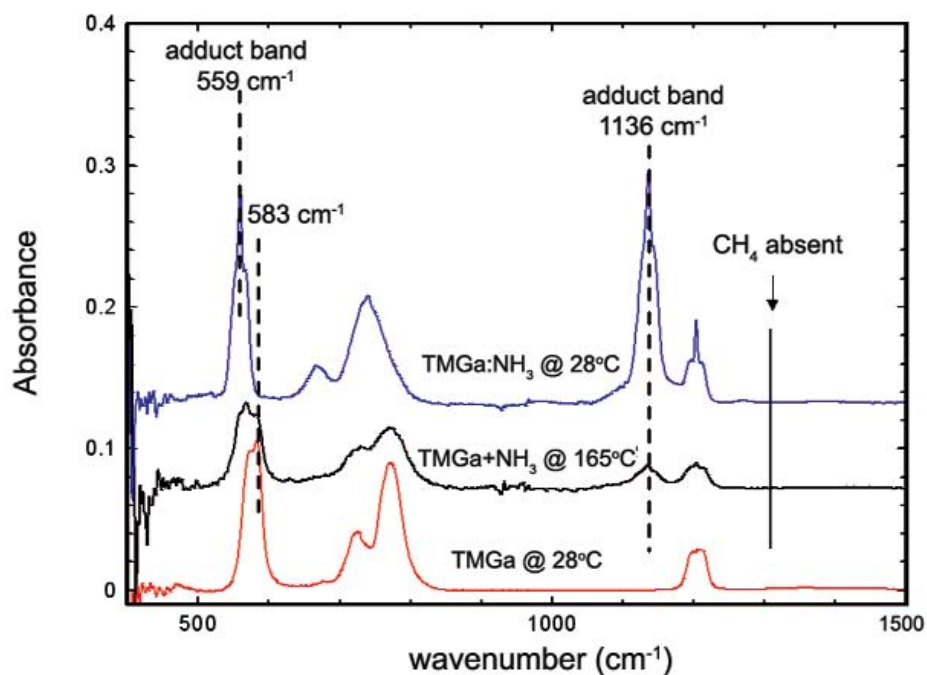


**Figure 1.** Gas-phase FTIR demonstrates that for typical OMVPE inlet conditions the TMGa:NH<sub>3</sub> adduct formation is reversible, i.e., no CH<sub>4</sub> is produced. As the temperature is raised this adduct simply dissociates back into the original reactants.

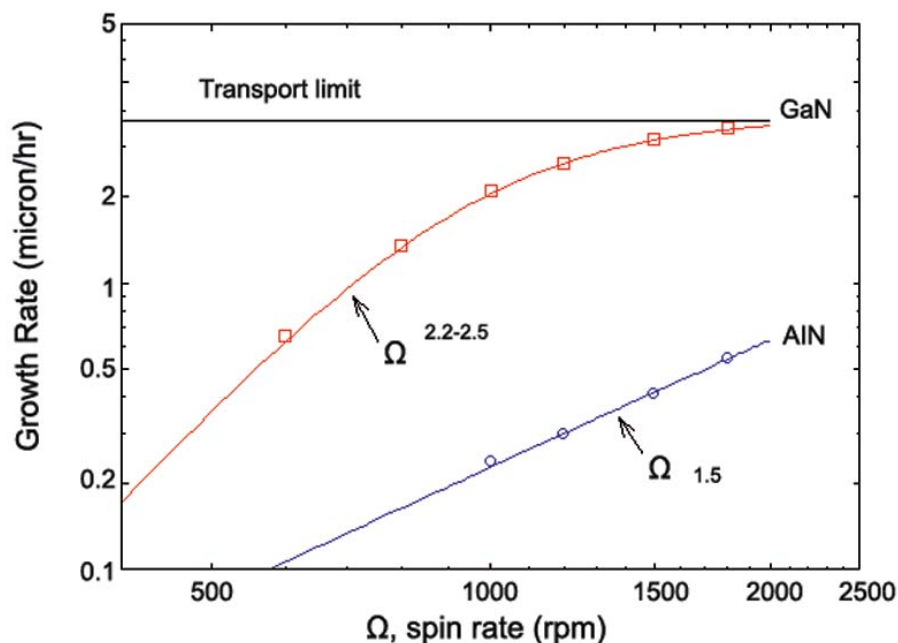


**Figure 2.** Growth rate of GaN and AlN at 1050°C as a function of RDR spin rate ( $\Omega$ ) at matched flow conditions. Without a parasitic process the growth rate would be independent of  $\Omega$  and at the transport limit. A high-temperature parasitic chemical mechanism is responsible for the strong  $\Omega$  dependence.



# Complex and Collective Phenomena



## Physics of Hierarchical Self-Organization

by G. C. Osbourn

**Motivation**—Nature's approach to building complex structures and functions is *hierarchical*. Nature's hierarchically organized materials are typically highly functional systems, with remarkable properties that include self-assembly, self-repair and adaptability to environmental conditions. These properties are themselves hierarchical, i.e., they recur at many length scales — from the nanoscale of the underlying molecular components to the macroscale of organisms. The nanoscale revolution is being driven by the hope that new classes of technology, from smart materials to self-assembling/healing sensors and electronics, may some day be developed with these and other remarkable properties. A key guide to nanotechnology success will be a theoretical understanding of the hierarchical design and assembly processes by which living organisms create materials and functional complexes. At present, no such understanding exists — man-made hierarchical self-organization of functional systems has not yet been created in the lab or the computer. This understanding is needed before we can know what properties must be present in a collection of active nanoscale components for them to carry out man-made hierarchical self-organization and what new classes of man-made machines and systems could be made in this fashion given the appropriate nanoscale components.

**Accomplishment**—We have initiated a research effort to develop a statistical mechanics approach to understanding driven, far-from-equilibrium populations of active machines that develop complex collective behaviors. This physics-based approach will attempt to mimic the collective behaviors in living organisms that drive hierarchical self-organization from the nanoscale to the macroscale. Through the exploration and

manipulation of simulated collective behavior at one length scale, we hope to develop an understanding of how further self-organizing collective behavior can be caused to emerge at larger length scales (hierarchy levels). Our initial work is based on our concept of an "entropy pump" (Fig. 1) as a key component of non-equilibrium self-organizing systems. Entropy pumps are generalizations of Carnot-cycle heat engines that deal with the non-thermal degrees of freedom of a physical system. Using populations of entropy pumps of a particular design, we have achieved, in initial computer simulations, a collective behavior that acts as a selective "organizational amplifier". The amplifier acts to increase its own internal machine population size, if seeded with a machine population that has extremely low entropy (is highly ordered). The same system eliminates a seeded population that has a high entropy (disordered) distribution. The conditions under which this self-organizing collective behavior is achieved are already providing interesting, useful insights into the requirements for building and maintaining self-organizing systems. In particular, our results (Fig. 2) suggest that continual "self-destruction" of *fully functional* machines is essential for maintaining extreme non-equilibrium collective states. This also suggests an unexpected role for apoptosis of healthy cells in multi-celled organisms beyond the maintenance of cell population sizes.

**Significance**—We have initiated a new research program intended to support emerging nanotechnology and biotechnology programs at SNL and DOE. Our results suggest that a physics-based approach may prove useful in understanding and ultimately synthesizing hierarchical self-organizing systems.

---

**Sponsors for various phases of this work include:** Nuclear Weapons/Science and Technology

**Contact:** Gordon C. Osbourn; Lasers, Optics and Remote Sensing, Department 1118

Phone: (505) 844-8850, Fax: (505) 844-5459, E-mail: gcosbou@sandia.gov

---

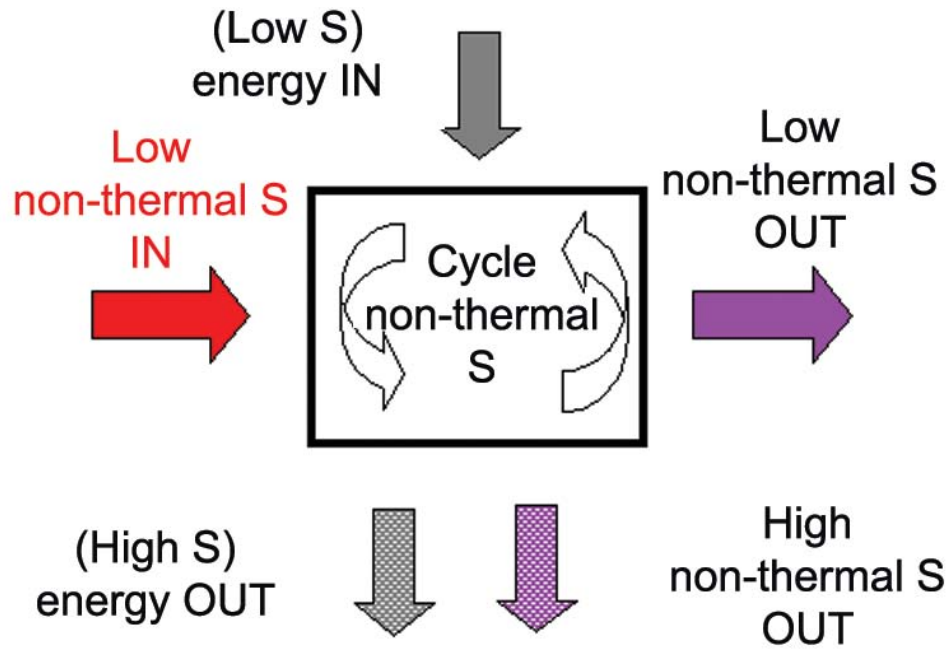


**Figure 1.** Schematic of the energy and entropy (S) flows through and within an entropy pump.

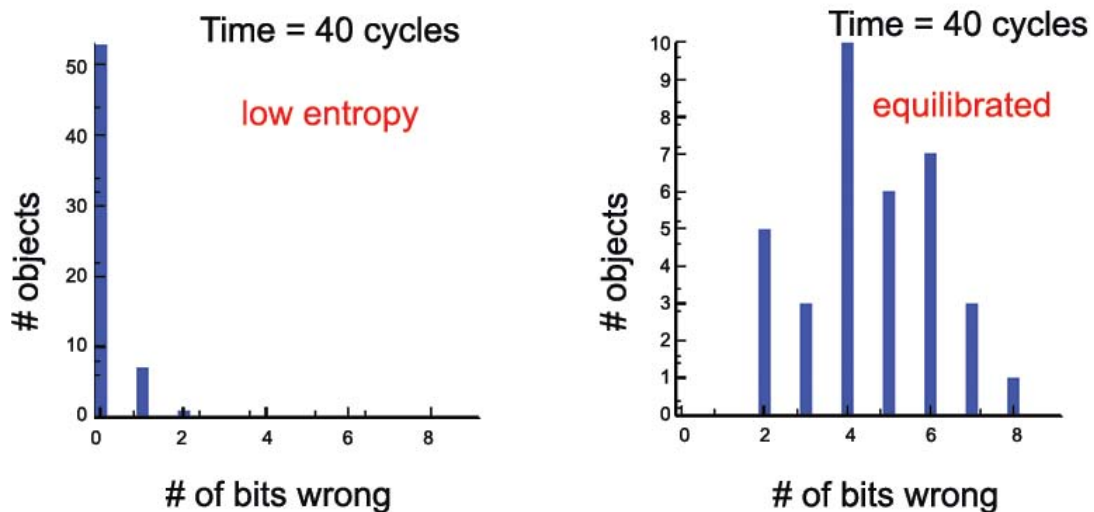


**Figure 2.** Simulation results comparing histograms of two populations of self-organizing entropy pumps, seeded with identical organized states initially, but with self-enforced machine lifetimes that are either much shorter (left) or longer (right) than typical times to failure for the pumps. The horizontal scale gives an increasing measure of lost organization towards the right. The organization of the population persists if many "healthy", working machines are continually eliminated as at left. The population at right is already near equilibrium after 40 simulation time steps, and has lost the information and organization of its initial non-equilibrium state.

## Measurement of Dust Charge and Interaction in 2D Plasma Dust Crystals

by *M. E. Riley, G. A. Hebner, D. S. Johnson, P. Ho, and R. J. Buss*

**Motivation**—Material bodies in contact with a typical low-temperature plasma result in the plasma becoming positively charged relative to the material, be it a dielectric or conductor. This is because of the higher thermal speed of electrons compared to ions (due to mass and temperature) and the comparable sticking probabilities on the surface. Dusty plasmas occur everywhere from interstellar space to semiconductor processing reactors. In 1986 it was pointed out that plasma dusts could crystallize, and this was first observed in 1994. Several hundred relevant journal articles have appeared since then. Typical plasma dust particles are several micrometers in diameter, are easily visible by scattered light, and bear a net resident negative charge of tens of thousands of electrons. Scientific interest is high not only because of astronomy and the semiconductor industry, but also because the crystals are a macroscopic platform on which to test and develop theories of many physical phenomena. These include wave propagation in ionic solids, phase transitions in Coulomb and shielded-Coulomb crystals, lattice stability, dynamics of crystallization, charging mechanisms within plasmas, and physics of the surrounding plasma.

Our prime motivation is to understand the forces on and interactions of the particles. The more complex aspect of the interaction is that it is non-central and non-reciprocal. There also are ion flow scattering forces, thermophoresis, gravity, gas friction, and plasma sheath fields.

**Accomplishment**—We have developed a novel experimental and theoretical procedure for measuring the particle interactions within the plane of a two-dimensional (2D) dust crystal. Dust particles trap into a 2D horizontal layer

because of the balance of gravity and plasma electric field adjacent to a horizontal flat electrode. Similar to marbles "crystallizing" in the bottom of a shallow bowl, we used a mildly curved spherical depression ( $R_c=0.5$  m) in the bottom electrode of an rf plasma reactor to apply an external force to a nearly planar, conformal monolayer of uniform sized dust. This design removes components of the poorly understood ion wind force and thermal force from the problem. Using a novel equation of state for the 2D close-packed triangular lattice, we balance gravity against the internal forces and extract the dust charge and screening length of the pair interaction. Figure 1 shows various amounts of compression within crystals of differing sizes. Due to the compression there are packing defects contained in the lattice. In Fig. 2 we show the agreement of the measured nearest-neighbor separation with that predicted by the equation of state as a function of radius. The scatter in the data is due to the defects. The constitutive interaction parameters in the equation of state, charge and screening length, have been determined by regression analysis.

**Significance**—We now have a methodology that allows direct measurement of the charge and screening length on a dust particle trapped within a plasma. We do not depend on estimates of local plasma properties (electron temperature, ion temperature, density) to determine the charge and screening. This is useful for all methods that use these particles to study collective phenomena.

We now are in a forefront position that allows the plasma dust to be used as a probe for exploring the fields within the plasma presheath — a region for scientific investigation.

---

**Sponsors for various phases of this work include:** BES

**Contact:** Greg A. Hebner, Plasma Sciences, Department 1118

Phone: (505) 844-6831, Fax: (505) 844-5459, E-mail: gahebne@sandia.gov

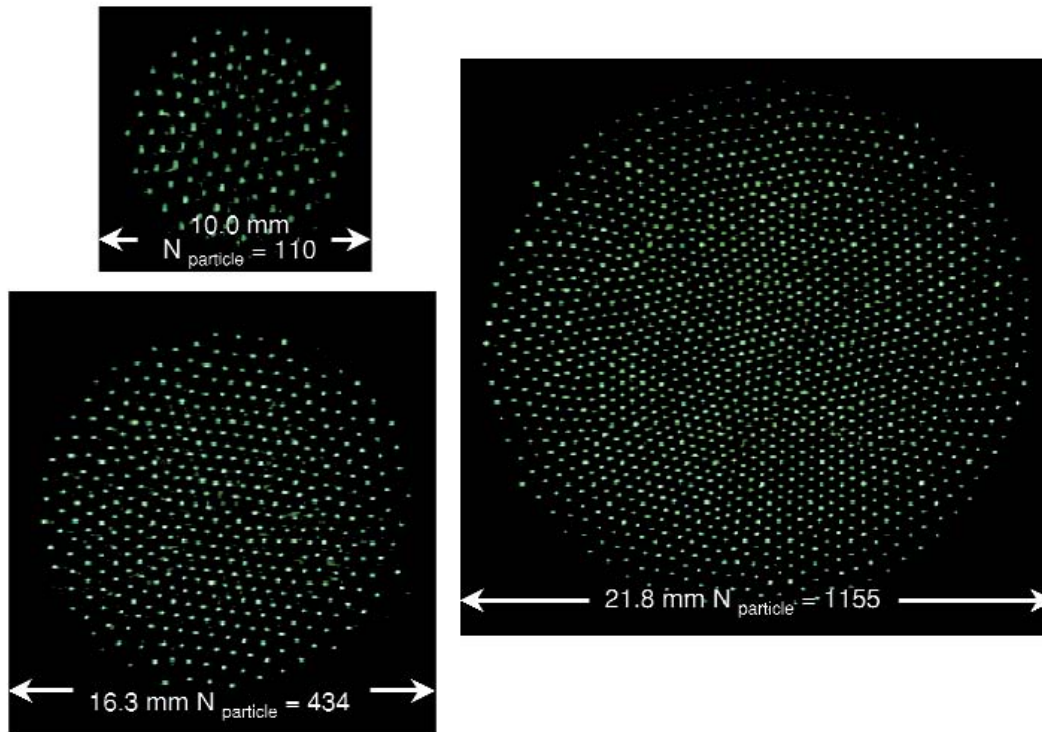


**Figure 1.** Top view of light scattering from plasma crystals comprised of different numbers of  $8.3\ \mu\text{m}$  diameter, melamine formaldehyde particles suspended in a 1.8 W, 110 mTorr argon plasma. The length scale is shown in each image. Horizontal confinement is provided by curvature of the lower electrode. The radial variation in nearest neighbor spacing is visible for the larger crystals.

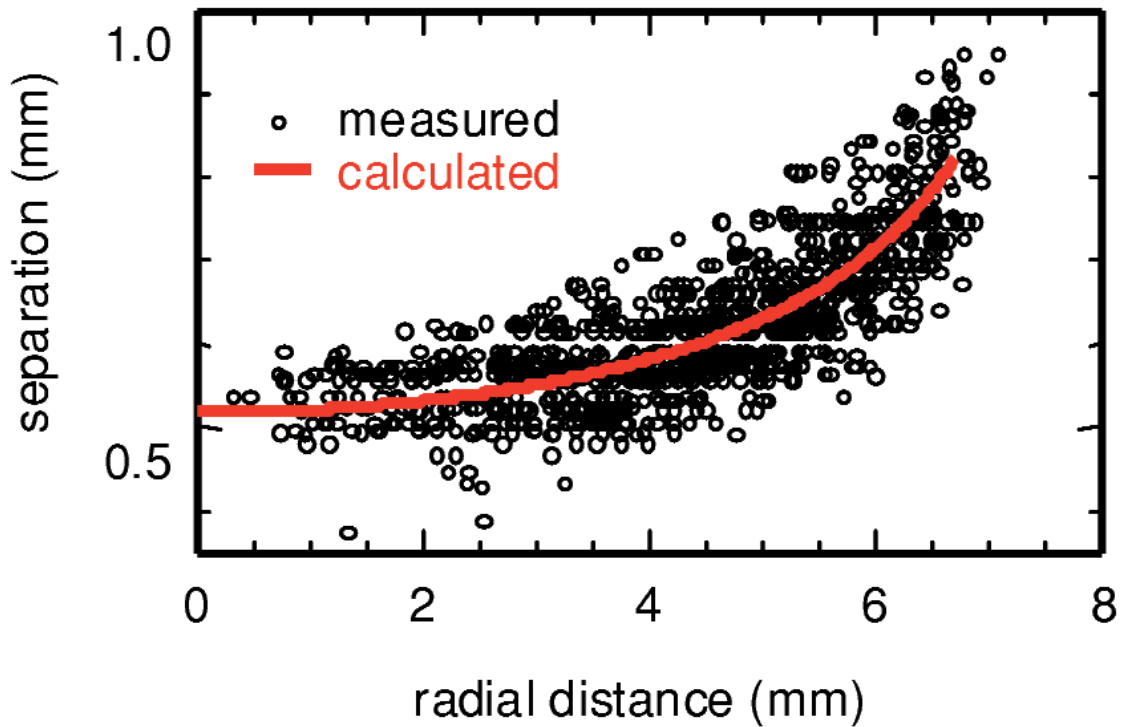


**Figure 2.** Nearest neighbor separation as a function of radial position for a plasma crystal with 434 particles, plasma power of 1.8 W, pressure of 110 mTorr, and  $R_c = 0.5\ \text{m}$ . The solid line was calculated from the equation of state using  $\lambda D = 260\ \mu\text{m}$  and  $Z = 23500$  electron charge units.



# Recent Awards and Prizes

## Recent Awards and Prizes

### **National and International Awards**

- 2000 — R&D 100 Award for the Ion Electron Emission Microscope (IEEM). [Barney Doyle, George Vizkelethy, Robert Weller (Vanderbilt University), and Berthold Senftinger (Staib Instruments, Inc., in Germany)]
- 1999 — American Chemical Society Earle B. Barnes Award for outstanding leadership in chemical research management: "For visionary leadership in managing laboratory and inter-laboratory research in the National interest at the frontiers of materials science." (George A. Samara)

### **DOE Basic Energy Sciences, Material Science Awards**

- 2000 — DOE Energy@23 Award (top 23 DOE innovations from 1977-2000 contributing to American consumers) for the Strained-Layer Semiconductor. (Gordon Osbourn)
- Energy 100 Awards (top one hundred discoveries and innovations from the Department of Energy that have resulted in improvements for American consumers from 1977-2000) for the Biological Microcavity Laser. (Paul Gourley)
- 1999 — 1<sup>st</sup> place for BES "Chunky Bullet Shootout," entitled "Detecting Cancer Quickly and Accurately." (Paul Gourley, et al.)

### **Other Awards**

- 2001 — The Lockheed Martin NOVA Award: The annual NOVA Awards honor 50 Lockheed/Martin individuals/teams "who have made outstanding contributions to Mission Success." A Sandia/industry team has developed the first 1.3-micron electrically pumped vertical cavity surface emitting laser (VCSEL) grown on a GaAs substrate using InGaAsN as the active material for ultra-high bandwidth datacomm and integration with silicon microsystems. [1.3-Micron Vertical Cavity Surface Emitting Laser (VCSEL) Team: John Klem, Andy Allerman, Kent Choquette, et al.]
- 1999 — Elected to the rank of AAAS Fellow by the American Association for the Advancement of Science for his "national leadership in materials science and for pioneering contributions to ion beam analysis and modification of materials". Researchers are "elevated to this rank because of their efforts toward advancing science or fostering applications that are deemed scientifically or socially distinguished". (Tom Picraux)

---

## **Patents Awarded**

### **2001**

#### **— Patent 6,258,615**

Title: Multiple Wavelength Vertical Cavity Resonance Devices Fabricated by Selective Area Epitaxy in MOVPE

Originators: Michael E. Coltrin, Org. 1126; Hong Q. Hou and Kent D. Choquette, Org. 1742

#### **— Patent 6,187,592**

Title: Method for Determining Hemoglobin Concentration in Individual Red Blood Cells

Originator: Paul L. Gourley, Org. 1140

#### **— Patent 6,245,200**

Title: Visible Light Photooxidation of Toxic Organic Chemicals Using Nanoscale MoS<sub>2</sub>

Originator: Jess P. Wilcoxon, Org. 1122

#### **— Patent 6,252,287**

Title: Heterojunction InGaAsN Solar Cells

Originators: Steven R. Kurtz, Org. 1123; Eric Daniel Jones, Org. 1741; Andrew A. Allerman, Org. 1126; John F. Klem, Org. 1742

#### **— Patent 6,194,769**

Title: Sensor Devices Based on Field-structured Composites

Originators: Robert C. Hughes, Org. 1744; James E. Martin, Org. 1122; Robert A. Anderson, Org. 1846

#### **— Patent 6,248,992**

Title: Tailored Doping Profile for Photoconductive Semiconductor Switch

Originators: Guillermo M. Loubriel, Darwin James Brown, Fred J. Zutavern, Wesley D. Helgeson, Martin W. O'Malley, and Gary J. Denison, Org. 15333; Charles T. Sullivan, Hong Q. Hou, and Albert G. Baca, Org. 1742; Thomas E. Zipperian, Org. 1740; Andrew A. Allerman, Org. 1126; Harold P. Hjalmarson, Org. 9235

#### **— Patent 6,290,868**

Title: Field-structured Chemical Sensor

Originators: Robert C. Hughes, Org. 1744; James E. Martin, Org. 1122; Robert A. Anderson, Org. 1846

### **2000**

#### **— Patent 6,147,793**

Title: Short-Cavity, Pulsed Optical Parametric Oscillators

Originators: Arlee V. Smith and William J. Alford, Org. 1118

#### **— Patent 6,110,390**

Title: A Double Electron Layer Tunneling Transistor (DELTT)

Originators: Timothy J. Drummond, Org. 5911; Marc E. Sherwin, Org. 1322; Jerry A. Simmons, Org. 1123

— **Patent 6,035,246**

Title: Chemical Recognition Software

Originators: John S. Wagner, Org. 15311; Gary Carmen Tisone, Org. 15334; Philip J. Hargis, Jr., Org. 1118

— **Patent 6,048,546**

Title: Lipid Bilayer Entrapment in Sol-gel Materials

Originators: Douglas A. Loy, Org. 6245; Darryl Y. Sasaki, Org. 1140; Stacey A. Yamanaka, Org. 1812

— **Patent 6,103,305**

Title: Zero Stress Amorphous Diamond

Originators: Thomas A. Friedmann and John P. Sullivan, Org. 1112

— **Patent 6,057,377**

Title: Molecular Receptors in Functionalized Sol-gel Materials Generated through Molecular Imprinting

Originators: Carol S. Ashley and C. Jeffrey Brinker, Org. 1841; Darryl Y. Sasaki, Org. 1140

— **Patent 6,022,748**

Title: Immobilization of Colorimetric Liposomes into Sol-gel Matrices for Direct Colorimetric Detection

Originators: Darryl Y. Sasaki, Org. 1140; Stacey A. Yamanaka, Org. 1812

— **Patent 6,085,581**

Title: 3 Dimensional 2 Location Positioner with Reverse Referencing

Originators: Gary D. Jones, Org. 1812; Jack E. Houston, Org. 1114; Kenneth T. Gillen, Org. 1811

— **Patent 6,071,109**

Title: The Preparation of AlInSb by Metal-Organic Chemical Vapor Deposition

Originators: Kevin C. Baucom and Robert M. Biefeld, Org. 1126; Andrew A. Allerman, Org. 1126

— **Patent 6,117,369**

Title: Improved Molecular Optical Switch Based on Nickel Porphyrins

Originator: John A. Shelnutt

— **Patent 6,083,360**

Title: Use of Supplemental Heating for Deposition Tooling Shields

Originators: John A. Hunter, Org. 1114; Diane E. Peebles, James A. Ohlhausen, and Kenneth Hall Eckelmeyer, Org. 1822

**1999**

— **Patent 5,965,271 (Continuation patent based on Patent 5,736,245)**

Title: Chemical Treatment for Silica Containing Glass Surfaces

Originators: William L. Smith and Alexis Grabbe, Org. 1114; Terry A. Michalske, Org. 1140

— **Patent 5,995,529**

Title: Mid-infrared, InGaAsSb-based LEDs and Lasers with Semi-metal Electron Injection

Originators: Steven R. Kurtz, Org. 1742; Robert M. Biefeld and Andrew A. Allerman, Org. 1126

---

— **Patent 5,858,559**

Title: Method for Altering the Luminescence of a Semiconductor

Originators: Duane Dimos, Org. 1831; J. Charles Barbour, Org. 1111

— **Patent 5,864,381**

Title: Automated Pupil Remapping with Binary Optics

Originator: Dan Neal, Org. 1128

— **Patent 5,901,247**

Title: A New Cluster Analysis Method

Originators: Gordon Osbourn and R. Martinez, Jr., Org. 1155

— **Patent 5,902,636 (Divisional of Patent 5,736,245)**

Title: Method for Chemical Surface Modification of Fumed Silica Particles

Originators: A. Grabbe and W. L. Smith, Org. 1114; T. Michalske, Org. 1115

— **Patent 5,926,773**

Title: Chemical Recognition Software

Originator: J. Wagner, Org. 15334

— **Patent 5,912,738**

Title: Wafer Curvature Measurement Using Parallel Laser Beams

Originators: E. Chason and J. Floro, Org. 1112; C. Seager, Org. 1111; M. Sinclair, Org. 1812

— **Patent 5,939,716**

Title: A Three-dimensional Light Trap for Reflective Particles

Originator: Daniel R. Neal, Org. 1128

— **Patent 5,936,739**

Title: Frequency-converting Short-pulse Image Intensifier Based on Optical Parametric Amplification for the Detection of Phase

Originators: Mark W. Kimmel and Daniel R. Neal, Org. 1128; David E. Bliss, Org. 15333; Stewart M. Cameron, Org. 15336

— **Patent 5,936,720**

Title: Amplitude & Phase Beam Characterization Using a Two-dimensional Wavefront Sensor

Originators: William J. Alford, Org. 1118; Daniel R. Neal, Org. 1128; James K. Gruetzner, Org. 15333





# Government Advisory Boards and Professional Societies



---

## Government Advisory Boards

### **National Research Council**

- Board on Astronomy and Physics; Julia Phillips, member; 2000-2003
  - Solid State Sciences Committee; Julia Phillips, Vice Chairman; 1998-2001
- National Materials Advisory Board; Julia Phillips, member; 1999-2001
  - Committee on Materials Research for the Defense-After-Next; Julia Phillips, member; 1999-2002
- U. S. Liaison Committee for the International Union of Pure and Applied Physics; Julia Phillips, member; 2000-2002

### **Argonne National Laboratory**

- Materials Science Division External Review Committee; Julia Phillips, member; 1995-2000

## Professional Societies

### **American Physical Society**

- APS Division of Materials Physics (DMP) Executive Committee Member at Large, Julia Phillips, 1997-2000

### **American Vacuum Society**

- AVS Surface Science Division Chair, Neal Shinn, 2000-2001
- AVS Surface Science Division Program Chair, Neal Shinn, 1999-2000

### **Materials Research Society**

- MRS Meetings Chair, Jerry Floro, 2001
- MRS Symposium Organizer, Tom Friedmann, 2001
- MRS Symposium Organizer, Eric Jones, 2000

### **Optical Society of America**

- OSA-Committees for 2000 Awards: Max Born Award Member, Arlee Smith, 2000



# Resources and Capabilities

## Resources and Capabilities Physical and Chemical Sciences Center

### — Diagnostics and Characterization —

#### Atomic-Level Imaging and Spectroscopy

We have developed technical capabilities in:

- Scanning Tunneling Microscopy (STM) with the ability to track the diffusion of single atoms on surfaces,
- Low Energy Electron Microscopy (LEEM) with nanometer spatial resolution and spectroscopic imaging capability;
- Field Ion Microscopy (FIM) with single atom resolution and accurate temperature control to 1 Kelvin,
- Atom Probe Microscopy (APM) with pulsed laser desorption capability,
- Interfacial Force Microscopy (IFM) with feedback for accurate force profile measurements, and
- Atomic force microscopy (AFM) for imaging, force profiling, and manipulation of individual biomolecules in fluid environments with simultaneous fluorescence detection.

#### Simultaneous Measurement of H, D, and T in Materials

We have designed and implemented a new ion beam analysis (IBA) system to simultaneously measure the absolute quantities of H, D, and T in materials using an elastic recoil detection (ERD) technique. The technique uses an E-dE detector arrangement, or particle telescope, to provide for accurate separation of the H, D, and T signals. The system can also simultaneously acquire information about medium and high Z elements in the sample using Rutherford backscattering spectrometry (RBS). Measurement of other light elements is possible using the nuclear reaction analysis (NRA) technique, which is isotope specific. The system will have an accuracy of  $< 2\%$  for measuring the composition of solids.

#### Ion Accelerator Nuclear Microprobe

We have facilities for nuclear microscopy and radiation effects microscopy based on a 6 MV

tandem Van de Graaff ion accelerator. We generate ion species from hydrogen to gold for both radiation effects research and quantitative high-energy ion beam analysis of materials containing light elements (hydrogen to fluorine) using heavy ion elastic recoil detection (ERD) and heavy elements using high-energy backscattering spectrometry, and Heavy Ion Backscattering (HIBS). (Includes Patent #5,059,785 issued October, 1991.) An external Micro Ion Beam Analysis (X-MIBA) capability enables multi-elemental analysis and ion irradiation of samples, which are vacuum incompatible or extraordinarily large. The Sandia Nuclear Microprobe with micrometer size high-energy ion beams is used to study materials and devices. Special emphasis is given to the evaluation of the radiation hardness of microelectronic devices using three new advanced diagnostic techniques invented at Sandia: Single-Event-Upset Imaging, Ion-Beam-Induced-Charge-Collection Imaging (IBICC), and time-resolved IBICC. A recent development is the Ion Electron Emission Microscope (U. S. Patent No. 6,291,823 and 2001 R & D-100 Award winner) which can perform radiation microscopy using very highly ionizing particles *without* focusing the ion beam.

#### Materials Microcharacterization

Our capabilities in this area include optical microscopy, scanning, electron microscopy, analytical transmission electron microscopy, double crystal x-ray diffraction, ion beam analysis of materials (RBS, channeling, ERD, PIXE, NRA), Hall measurements, microcalorimetry, photoluminescence, light scattering, electronic transport, deep level spectroscopy, magnetization, and dielectric and magnetic susceptibilities.

#### Surface and Interface Spectroscopies

We maintain strong capabilities in Auger electron spectroscopy (AES), x-ray photoelectron



---

spectroscopy (XPS), low energy electron diffraction (LEED), ultraviolet photoelectron spectroscopy (UPS), thermal desorption spectroscopy (TDS), infrared reflectance-absorption spectroscopy (IRAS), and quantum state resolved laser surface probes.

### **Vision-Science Laboratory**

The vision science laboratory consists of state-of-the-art hardware and software capabilities for carrying out video inspection, multi-spectral image analysis, and sensor-based pattern recognition. (Includes Imaging Processing System, Patent #5,495,536.) These capabilities are used in applications ranging from microsensor-based chemical detection and recognition to automated video/SEM inspection of semiconductor materials and circuits (Patent #5,901,247). This is a new approach to pattern recognition, coupling perception-oriented research with machine algorithms.

### **Chemical Vapor Deposition (CVD)**

Our experimental tools for investigating CVD include optical probes (such as reflectance-difference spectroscopy and emissivity correcting pyrometry) for gas-phase and surface processes, a range of surface analytic techniques, molecular beam methods for gas/surface kinetics, and flow visualization techniques. These tools are integrated in a unique manner with research CVD reactors and with advanced chemistry and fluid models.

### **Growth Science Laboratory**

Capabilities for in situ characterization of materials during thin film deposition, molecular beam epitaxial growth, and low energy ion beam simulated growth, include intensity profile sensitive reflection high energy electron diffraction (RHEED) for surface structure, energy dispersive x-ray reflectometry for in situ surface and interface structure, multibeam wafer curvature for strain (Patent #5,912,738), and Auger electron spectroscopy for surface composition.

### **KMAP X-ray Diffractometer**

Based on double crystal x-ray diffractometry in combination with position sensitive x-ray detection, our KMAP x-ray diffraction analysis is used to determine the lattice constant, strain relaxation, composition, layer orientation, and mosaic spread for a large variety of advanced epitaxial semiconductor material systems.

### **Nanoelectronics Laboratory**

We have the capabilities for fabrication of nanoscale quantum device structures, together with capabilities for ultra-low-noise measurement of transport from 0.3 Kelvin to ambient at high magnetic fields.

### **Lasers and Optics**

We provide characterization and advanced understanding in the area of solid-state lasers and non-linear optics, especially as coherent sources of broadly tunable light in rugged, compact geometries. We also have established expertise in long-term and transient radiation effects characterization of optical materials. (Includes patented Wavefront Sensor Patent #5,493,391, and Monolithic Optical Amplification Devices Patent #5,463,649.) Capabilities include the widely used (approximately 2000 users worldwide) SNLO (Sandia Non-Linear Optics) code, which is a lab-tested code for predicting the performance of non-linear optical components. In the area of integrated optical materials, our laboratories produce new types of photosensitive materials (processing patent applied for) for directly-writeable waveguides and reconfigurable optical interconnects.

### **Laser and Optical Spectroscopies**

Our capabilities in characterizing semiconductor materials by photoluminescence and magnetoluminescence extend down to low temperatures by optical laser imaging and laser microscopy, by laser excitation spectroscopy, and by the time-resolved measurements of optical emission. We

also have developed a high lateral resolution, near-field scanning optical microscopy (NSOM) capability with time and frequency resolution.

### **Low-Temperature Plasma Analysis**

We have state-of-the-art capabilities for the analysis of low-temperature plasmas as found in commercial processing reactors. These include

emission spectroscopy, electrical characterization, laser and microwave-based measurements of species concentrations, in situ electric field measurements, and others. Sandia is the only lab that combines new diagnostics, relevant process chemistries (complex mixtures), and massively parallel (MP) computer models for simulation of continuous and transient plasmas.

## **— Synthesis and Processing —**

### **Biomaterials Laboratory**

The Biomaterials Laboratory possesses equipment to perform numerous molecular biology and biochemistry research including genomic DNA, RNA, and plasmid isolation from a variety of sources (e.g., bacteria, viruses, and eukaryotic tissues and cells). DNA sequences can be cloned into a variety of organisms, permitting the manipulation and modification of DNA and protein sequences, structure, and function. Cloned DNA sequences can be genetically engineered using reverse transcription, the polymerase chain reaction and site-directed mutagenesis. Native and recombinant proteins also can be expressed, purified, characterized, and functionalized in this laboratory.

### **Monolayer Deposition of Organic Films**

We have a Langmuir-Blodgett facility for controlled deposition of mono- and multi-layer organic films. The facility includes two computer-controlled troughs, *in situ* fluorescence microscopy, vibration isolation, and a dust-free down flow work area.

### **Nanocluster Laboratory**

We have developed and patented a process based on the use of inverse micelles for the synthesis of large quantities of monodisperse clusters of metals, semiconductors, and oxides.

### **Electron Cyclotron Resonance (ECR)**

This plasma facility has been built for studying fundamental processes governing the growth of oxide and nitride dielectric films used in

optoelectronics and used as hard coatings. This is the only system in the U.S. which combines ECR plus e-beam evaporation.

### **Molecular Beam Epitaxy (MBE)**

We have research semiconductor growth laboratories for ultra-pure and ultra-flexible MBE growth of III-V materials. In addition, we have research systems for Group IV semiconductor growth.

### **Metal-Organic Chemical Vapor Deposition (MOCVD)**

We maintain research facilities with capabilities in MOCVD of III-V compound semiconductor materials including GaN-based materials and self-assembled quantum dots. These capabilities include research reactors designed specifically for studies of CVD chemistry, fluid dynamics, the development of advanced in situ diagnostics, and the development of advanced semiconductor heterostructures and devices.

### **Crystal and Thin Film Growth**

Capabilities in this area include pulsed laser deposition chambers, a high vacuum metal deposition chamber, a thin film oxide deposition chamber, a diamond-like carbon deposition chamber, a hot filament chemical vapor deposition chamber, and various apparatus for single crystal growth. Our capabilities for stress relief of diamond-like carbon films and structures produced by pulsed laser deposition are not available elsewhere.

---

### **400 kV and 180 keV Ion Implanters**

These systems are equipped with a variety of sources (gas, sputter, and metal vapor). This facility provides ion species from hydrogen to bismuth that can be used for studying fundamental irradiation mechanisms and selective chemical doping in semiconductors, metals, ferroelectrics, and superconductors.

### **High Pressure and Shock Wave Physics and Chemistry Laboratories**

Our capabilities in this area include large volume static high pressure apparatus which can

be operated at temperatures ranging from 2 to 700 K and in magnetic fields, as well as gas gun and explosive loading facilities with state-of-the-art, time-resolved diagnostics. Recovery fixtures have been developed for use with the gas gun and explosive shock loading facilities that allow unique material synthesis over broad ranges of shock pressures and temperatures.

## **— Theory and Simulation —**

### **Electronic Structure and Linear Scaling**

We have developed state-of-the-art massively parallel electronic structure algorithms, based on *ab initio* pseudopotentials and plane-wave/Gaussian basis functions. These codes are used to develop a fundamental understanding of physical phenomena and materials, including compound semiconductor band structure, diffusion of point defects, dopants and impurities, optoelectronic properties of extended defects, adsorbate interactions on surfaces, bonding at metal-oxide interfaces, and enhanced reactivity of nanoparticles. To allow the investigation of more complex systems and phenomena, we have developed new computationally efficient algorithms, e.g., self-consistent linear scaling density functional theory, and variable and real-space gridding.

### **Chemical Processes**

We have extensive capabilities, including massively-parallel computation, to model complex chemically reacting flows such as occur in chemical vapor deposition manufac-

turing processes. Our numerical simulations can include the coupled gas-phase and gas-surface chemistry, fluid dynamics, heat, and mass transfer to provide predictive models of a chemical process.

### **Low-Temperature Plasmas**

We have extensive capabilities in massively parallel codes to simulate the time and space evolution of low-temperature plasmas, focusing on new theoretical techniques for achieving rapid convergence and on direct comparisons with experimental results.

### **Optical and Wave Propagation**

We have developed advanced simulation codes for understanding wave propagation in optical parametric oscillators and amplifiers for the purpose of designing highly efficient, tunable laser sources. We also have capabilities in novel optical designs, including resonators for compact laser geometries. These capabilities are coupled to in-house micro-optics construction facilities and state-of-the-art optics testing.

# Physical and Chemical Sciences Center FY01 Budget - By Customer

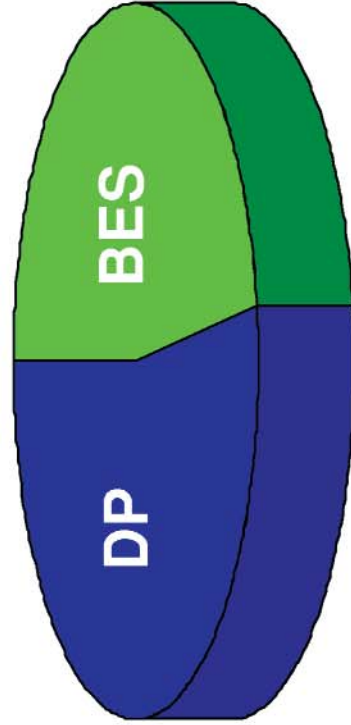


# Physical and Chemical Sciences Center

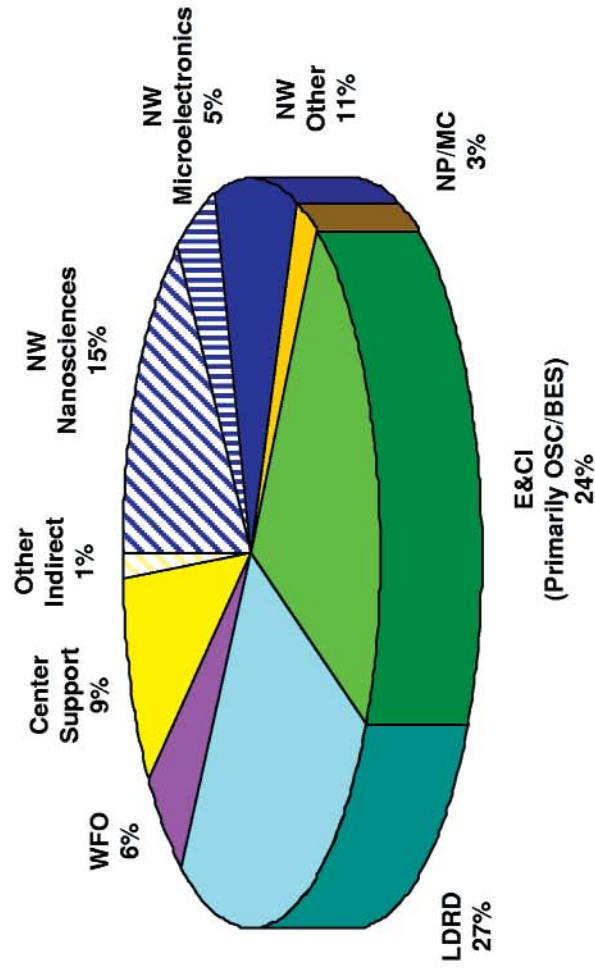
## FY01 Budget - By Customer

---

**Capital (\$1.4M)**



**Operating (\$32M)**







**SAND2001-3710P:** Prepared by Sandia National Laboratories, Albuquerque, New Mexico 87185 and Livermore, California 94550. Sandia is a multiprogram laboratory operated by Sandia Corporation, a Lockheed Martin Company, for the United States Department of Energy under Contract DE-AC04-94AL85000

Printed 2001

---